DEMOCRATIC AND POPULAR REPUBLIC OF ALGERIA

MINISTRY OF HIGHER EDUCATION AND SCIENTIFIC RESEARCH

UNIVERSITY OF KASDI MERBAH – OUARGLA

FACULTY OF MATHEMATICS AND MATERIAL SCIENCES

DEPARTMENT OF PHYSICS

Order N° : ……..
Serial N° : ……..…..

THÈSE DE DOCTORAT LMD

SPECIALITY: **PHYSIQUE**

OPTION: **Rayonnement et Matière**

BY: **MENACER FATMA**

THEME

Etude des propriétés physiques des clusters d'Or dopés pour les applications optoélectroniques

Défendu le 31/05/2026 devant le jury composé de :

Pr.	**Boukraa Aomar**	**Ouargla University**	**President**
Pr.	**Mehammdi lazhar**	**Ouargla University**	**Examiner**
Pr.	**Daoudi Bahmed**	**Ghardaia University**	**Examiner**
Pr.	**Bouhadda Youcef**	**URAER Ghardaia**	**Examiner**
Pr.	**Bentouila Omar**	**Ouargla University**	**Supervisor**
Pr.	**Aïadi Kamel Eddine**	**Ouargla University**	**Co-Supervisor**

DEMOCRATIC AND POPULAR REPUBLIC OF ALGERIA

MINISTRY OF HIGHER EDUCATION AND SCIENTIFIC RESEARCH

UNIVERSITY OF KASDI MERBAH – OUARGLA

FACULTY OF MATHEMATICS AND MATERIAL SCIENCES

DEPARTMENT OF PHYSICS

Order N° : ……..
Serial N° : ……..…..

THESIS OF LMD DOCTORATE

SPECIALITY: **PHYSICS**

OPTION: **Radiation and Matter**

BY: **MENACER FATMA**

THEME

Study of the physical properties of doped Gold clusters for optoelectronic applications

Pr.	**Boukraa Aomar**	**Ouargla University**	**President**
Pr.	**Mehammdi lazhar**	**Ouargla University**	**Examiner**
Pr.	**Daoudi Bahmed**	**Ghardaia University**	**Examiner**
Pr.	**Bouhadda Youcef**	**URAER Ghardaia**	**Examiner**
Pr.	**Bentouila Omar**	**Ouargla University**	**Supervisor**
Pr.	**Aïadi Kamel Eddine**	**Ouargla University**	**Co-Supervisor**

s work is dedicated, with profound reverence

and enduring gratitude

To my Father, whose foresight cleared the impediments from my path, illuminating and paving the way for the pursuit of knowledge. and Mother, whose tireless vigilance, sacrifice, and sleepless efforts provided the unwavering foundation and light for this academic journey.

To my Sister, my constant source of steadfast support and encouragement, and to my entire Family, the deepest wellspring of my strength and success.

And finally, to the loyal Comrades and Friends, who offered invaluable assistance and companionship, sharing both the burdens and the triumphs of this scientific endeavor.

Abstract

This thesis investigates the physical characteristics and structural stability of pure gold clusters and nanoclusters (Au_n), with a particular focus on the effects of metal doping using titanium (Ti) and platinum (Pt). The research explores doping with Ti ($TiAu_n$, n=1-17) and Pt ($PtTiAu_n$, n=1-16), emphasizing their applications in detectors and biosensors. The study employs density functional theory (DFT) with generalized gradient approximation (GGA) as implemented in the SIESTA simulation package. Time-dependent density functional theory (TDDFT) utilizes long-range corrected hybrid functionals, including B3LYP and CAM-B3LYP, where "CAM-B3LYP" denotes a variable with a corrected approach modified by adjusting the range separation parameter, computational resources from the HPC facility**. (HPC Ab initio simulations were performed using computational resources from the HPC facility (DGRSDT) at the University of Batna 2 (Algeria) /ROZA Deutsche Forschungsgemeinschaft (DFG, GERMANY RESEARCH FOUNDATION) in OLDENBURG)** were utilized for HPC Ab-initio simulations using the GAUSSIAN software package, implementing linear response theory. This approach determines excited-state properties by analyzing the electron density's response to time-dependent perturbations. Calculations employed first-principles wave function-based electronic correlation methods using a standard Hamiltonian within the Born-Oppenheimer approximation. The study examined the equilibrium geometry, electronic structure, and magnetic properties of $TiAu_n$, $PtTiAu_n$, Au_{n+1}(n = 1–17), and Au_{n+2} (n = 1–16) groups. The stability of the systems was evaluated through binding energies, bond lengths, second-order energy differences, and HOMO-LUMO electronic energy gaps. The findings reveal differences in the formation of planar, two-dimensional, and three-dimensional structures. As energies increase with larger group sizes, the groups gain energy as they expand. Theoretical gaps between HOMO and LUMO are prevalent with stable MAu. N groups (M = Ti, Pt) decrease with increasing group size. Vertical electron affinity (VEA), vertical ionization potential (VIP), and chemical hardness (η) indicate that certain MAu_n groups exhibit unique properties. Substituting Ti and Pt atoms modifies the magnetic moments of pure gold clusters. Excited-state calculations were performed for ground-state-optimized geometries of Aun, TiAun, and PtTiAun n=1-6 clusters using the configuration interaction (CI) methodology at different levels. While clusters exhibit a strong redshift compared to pure gold, dominant peaks in $PtTiAu_{4-6}$ show a slight blue shift relative to more active $TiAu_{4-6}$ systems. The Pt component, with its denser d-shell, stabilizes reactions by enhancing low-energy transitions. The absorption spectrum of $PtTiAu_{4-6}$ extends into the near-infrared region up to 700 nm, indicating low-energy charge transfer (CT) states induced by Ti, though their oscillator strength is weaker compared to Au or Pt transformations. Vibrational analysis shows that molecular symmetry influences Au_n spectra, with symmetric Au3 exhibiting limited activity (due to mutual exclusion), unlike the complex spectra of lower-symmetry Au_{4-6} clusters. Ti addition alters the bonding environment, causing a blue shift in the main IR absorption from (165 cm^{-1} in Au_4 to 340-380 cm^{-1} in $TiAu_3$) due to high-frequency MAu_n stretching modes. The Ti and Pt; Ti alloy clusters show denser Raman features and intense low-frequency modes (50-150 cm^{-1}), confirming enhanced polarizability and plasmonic coupling, which are crucial for superior SERS applications.

Keywords: DFT Simulation, $TiAu_n$ -$PtTiAu_n$ clusters, Physical properties, Siesta package, TDDFT Simulation, Gaussian package, UV-Vis/IR/Raman spectra.

الملخص

تبحث هذه الأطروحة في الخصائص الفيزيائية والاستقرار الهيكلي لمجموعات الذهب النقي والمجموعات النانوية (Au_n)، مع التركيز بشكل خاص على آثار ادخال المعادن والمعادن الانتقالية للتطعيم الأول والثاني باستخدام التيتانيوم (Ti) والبلاتين(Pt) على التوالي .يستكشف بحثنا هذا المنشطات للمجموعات العنقودية Ti ($TiAu_n$, n=1-17), Pt ($PtTiAu_n$, n=1-16)مع التركيز على تطبيقاتها في أجهزة الكشف وأجهزة الاستشعار الحيوية. باستخدام الدراسة النظرية للكثافة الوظيفية (DFT) مع تقريب التدرج المعمم (GGA) كما تم تنفيذها في حزمة محاكاة SIESTA. كما تم استخدام نظرية الكثافة الوظيفية المعتمدة على الوقت (TDDFT) مع وظائف هجينة المنفصلة والمصححة طويلة المدى B3LYP وCAM-B3LYP، حيث يشير "CAM-B3LYP" إلى متغير بنهج مصحح تم تعديله عن طريق ضبط معلمة فصل النطاق، تم تطبيقها في الموارد الحسابية من مرفق الحوسبة عالية الأداءHPC ,حسب المبادئ الأولى للمحاكاة Ab-initio باستخدام حزمة GAUSSIAN، وتنفيذ نظرية الاستجابة الخطية. يحدد هذا النهج خصائص الحالة المثارة من خلال تحليل استجابة كثافة الإلكترون للاضطرابات المعتمدة على الوقت. استخدمت الحسابات طرق الارتباط الإلكتروني القائمة على دالة الموجة ذات المبادئ الأولى باستخدام هاملتوني قياسي ضمن تقريب بورن-أوبنهايمر. تناولت الدراسة هندسة التوازن والبنية الإلكترونية والخصائص المغناطيسية لمجموعات $TiAu_n$ و$PtTiAu_n$ و($n = 1–17$) Au_{n+1} و($n = 1–16$) Au_{n+2}. تم تقييم استقرار الأنظمة من خلال طاقات الربط، وأطوال الروابط، وفروق الطاقة من الدرجة الثانية، وفجوات الطاقة الإلكترونية HOMO-LUMO. تكشف النتائج عن اختلافات في تكوين الهياكل المستوية وثنائية الأبعاد وثلاثية الأبعاد. مع زيادة الطاقات مع زيادة أحجام المجموعات، تكتسب المجموعات الطاقة مع توسعها. الفجوات النظرية بين HOMO وLUMO سائدة مع MAU المستقرة. تتناقص Nمجموعات (M ,Pt) Ti =، مع زيادة حجم العناقيد . تشير تقارب الإلكترون الرأسي (VEA)، وإمكانية التأين الرأسي (VIP)، والصلابة الكيميائية (η) إلى أن مجموعات MAu_n معينة تظهر خصائص فريدة. يؤدي استبدال ذرات Ti وPt إلى تعديل العزوم المغناطيسية لمجموعات الذهب الخالص. تم إجراء حسابات الحالة المثارة للأشكال الهندسية المحسنة للحالة الأرضية لمجموعات Au_n و$TiAu_n$ و$PtTiAu_n$ n=1-6 باستخدام منهجية تفاعل التكوين (CI) على مستويات مختلفة. في حين أن المجموعات تظهر انزياحًا أحمر قويًا مقارنة بالذهب الخالص، فإن القمم السائدة في $PtTiAu_{4-6}$ تظهر تحولًا طفيفًا إلى اللون الأزرق مقارنة بأنظمة $TiAu_{4-6}$ الأكثر نشاطًا. يعمل مكون Pt، بقشرته d الأكثر كثافة،على تثبيت التفاعلات من خلال تعزيز التحولات منخفضة الطاقة. يمتد طيف الامتصاص لـ $PtTiAu_{4-6}$ إلى منطقة الأشعة تحت الحمراء القريبة حتى 700 نانومتر، مما يشير إلى حالات نقل الشحنة منخفضة الطاقة (CT) التي يسببها Ti، على الرغم من أن قوة مذبذبها أضعف مقارنة بتحويلات Au أو Pt. يُظهر التحليل الاهتزازي أن التناظر الجزيئي يؤثر على أطياف Au_n، حيث يُظهر Au_3 المتماثل نشاطًا محدودًا (بسبب الاستبعاد المتبادل مبدا باولي)، على عكس الأطياف المعقدة لمجموعات Au_{4-6} ذات التناظر المنخفض. تؤدي إضافة Ti إلى تغيير بيئة الترابط، مما يتسبب في تحول أزرق في امتصاص الأشعة تحت الحمراء الرئيسي من (165 سم $^{-1}$ في Au4 إلى 340-380 سم $^{-1}$ في $TiAu_3$) بسبب أوضاع تمدد MAu_n عالية التردد. تظهر مجموعات سبائك Ti وPt؛ Ti ميزات رامان أكثر كثافة وأوضاع تردد منخفض مكثفة (50-150 سم $^{-1}$)، مما يؤكد الاستقطاب المعزز والاقتران البلازمي، وهو أمر بالغ الأهمية لتطبيقات SERS المتفوقة.

الكلمات المفتاحية: محاكاة DFT ، مجموعات $PtTiAu_n$ -$TiAu_n$، الخصائص ا لفيزيائية ، حزمة Siesta ، محاكاة TDDFT ، حزمة Gaussian ، أطياف UV-Vis/IR/Raman .

Acknowledgements

I offer my heartfelt thanks and appreciation to my supervisor. I would like to express my thanks and appreciation to the supervisors, both of **Pr.O. Bentouila** and **Pr. K.E. Aiadi,** where this research was supervised in the laboratory of LENREZA, Optoelectronics Team, Kasdi Merbah Ouargla University,In parallel with the applied part of the simulation, there are enormous and distinguished capabilities for informants ,Theoretical Physics Laboratory Bejaia University, laboratory of Oldenburg Germany, and for opening the way for me to explore the field of nanotechnology, and for providing access to various training courses, as well as introducing me to senior professors and scientists, who shared their expertise in the research and in-depth study of nanoparticles of noble metals. This motivated me and gave me the enthusiasm to gain more knowledge, which constantly pushes me to strive to achieve excellence and complete the deep and tiring thesis issue.

I would also like to express my sincere appreciation and greetings to the great professor, the good angel, **Pr. S. Mahtout** .I did not miss his guidance, continuous support, and motivation for the better throughout my research, and for sharing his wisdom, comments, suggestions, and his wonderful team, which was a bridge for me towards the leading countries in this field, as my first opportunity in Germany to come up with creative ideas for this journey, which was crowned with success and learning the best skills, according to **Pr. C. Coccchi** testimony.

I would also like to thank you. I extend my deepest greetings to **Pr. C. Cocchi** and her assistant, **Dr. Ana Maria**, for their efforts in assisting with various high-performance devices at the Accounting Center of the University of Oldenburg/Germany, and for the progress achieved in my materials science studies. And valuable tips from my research on developing detection techniques using nanomaterials.

I would also thank. I extend my deepest greetings to this **Pr.Dr. Al. FORTUNELLI** and her . assistant, **Dr.E.T. Roongcharoen**, **Dr.E.G. Alfonso**, in their efforts in assisting at the Center This contributed to delving deeper into understanding the .of Research of CNR PIZA/ITALY optical properties and effects of doping with metals and transition metals, which was crowned with success. The use of modern codes, such as Gaussian16, with high skill enabled the completion of research and the development of detection systems in the field of materials science and nanotechnology, yielding many valuable insights.

I can't find the words to express my gratitude to my family for their boundless love and support. The encouragement and motivation I constantly receive from them is the constant fuel that keeps me moving forward. I am grateful to everyone who supported me, and I also extend special thanks to **Dr. M.lasmi**, **Dr. F. Zabaar, and Dr.W. Agaunne** With a pillow. for their continued support of me. My sincere thanks to my co-workers and friends. **Dr.S.Djaddi** and **W.SWISSI** for their spontaneous jokes, beautiful discussions, insightful comments, and tolerance for me all this time.

I sincerely thank my doctoral committee, **Pr. A. Boukraa, Pr.Y. Bouhadda, Pr. B. Daoudi,** and **Pr.L. Mehammdi** for thoroughly evaluating my research progress in Materials Science. I am especially grateful to Prof. A. Boukraa for their generous guidance, valuable insights, and mentorship throughout this work.

List of figures

List of Tables

General Introduction:

Nanotechnology has emerged as a significant challenge in materials science in many promising fields, including energy and biomedicine. Materials have been studied, created, and recombined from nanoclusters and nanoparticles, bridging the gap between atomic-scale phenomena and bulk material properties. These systems are a unique platform: Structure and properties due to precisely tunable electronic, magnetic, and optical behavior changes at the atomic level. Exceptions and applications range from clean energy technologies (e.g., photovoltaics, hydrogen storage, and advanced batteries) to medical developments (e.g., targeted drug delivery, biosensing, and non-invasive cancer therapies) **[1,2]** Not to mention playing a crucial role in nanocatalysts, where engineered core-shell and hybrid nanostructures enhance reaction efficiency **[3]** Moreover, their incorporation into nanogold-based nanomaterials, polymer matrices, and ferrofluids emphasizes their wide applicability in industrial processes and advanced materials engineering **[4,5]** . Due to their economic and scientific importance. The relentless pursuit of miniaturization and improved functionality in modern technology has propelled the field of nanotechnology to the forefront of scientific research. In this context, noble metals, particularly gold, have emerged as key players, driving innovation in diverse sectors, from electronics and optics to catalysis and biomedicine. Unlike their bulk counterparts, materials confined at the nanoscale exhibit dramatically variable physical and chemical properties due to quantum mechanical effects and increased surface-to-volume ratios. Bridging the gap between atomic resolution and macroscopic functionality.

Gold clusters represent a unique class of nanomaterials that bridge the gap between atomic and bulk metallic behavior. Unlike semiconducting quantum dots, whose optical properties are governed by quantum confinement effects. **[6,7]** When reduced to nanoclusters typically consisting of a few to tens of atoms, gold exhibits unique quantum volumetric effects, such as discrete energy levels and tunable band gaps, that are not found in pure gold. Gold clusters (Au_n, where n = 10-100 atoms) exhibit distinctive size-dependent properties arising from their metallic character and relativistic 5d-6s electron coupling [8]The introduction of dopants such as platinum and titanium creates novel hybrid systems ($PtTiAu_n$) where Pt contributes catalytic activity through its accessible 5d orbitals **[9]**, while Ti introduces localized magnetic moments via its unpaired 3d electrons. Such doped clusters exhibit synergistic effects - the Pt sites enhance electronic interactions at cluster surfaces for catalytic applications **[10,11,12]** While Ti doping modifies the overall charge distribution and introduces spin polarization, these tailored properties make doped gold clusters particularly

promising for advanced applications ranging from heterogeneous catalysis to biomedical imaging, where their stability, tunable electronic structure, and multifunctionality offer significant advantages over conventional nanomaterials **[13]**. The precise control of dopant incorporation in these systems presents both a fundamental challenge in nano synthesis and an opportunity to engineer materials with customized electronic, magnetic, and catalytic properties**[14]**

Recent research highlights a surge in advanced biosensors using gold nanoclusters doped with metals like silver, copper, and platinum for cancer detection. These clusters offer exceptional fluorescence, conductivity, and enzyme-mimicking properties, enabling ultra-sensitive detection of biomarkers in blood or urine. Enzyme-stabilized gold nanoclusters, for instance, combine the specificity of biological recognition with the signal amplification of nanomaterials. Also, Platinum-doped gold clusters achieve molecular detection of tumor DNA (10^{-18} M) **[15]**, while titanium-doped systems enable combined MRI/fluorescence imaging with 92% accuracy in early-stage ovarian cancer **[16]** Silver-gold hybrids enhance surface-enhanced Raman spectroscopy (SERS), detecting pancreatic exocrine vesicles at single-particle resolution. Challenges remain in scalability and long-term biocompatibility, but machine-learning-designed catalyst combinations (e.g., palladium-$gold_n$) now predict tumor margins in real time**[17]**, improving early diagnosis accuracy **[18,19]**. Meanwhile, global cancer statistics remain sobering nearly 20 million new cases diagnosed in 2022, with late detection still a major challenge. These biosensors are paving the way for faster, less invasive, and more affordable cancer screening**[20]**

In light of the above, critical questions that remain unanswered include: What are the main structural differences between pure gold nanoclusters and those doped with titanium and platinum? How does the doping of gold nanoclusters with platinum affect their electronic properties, especially the HOMO-LUMO gap? What role does density functional theory (DFT) play in the computational simulation of the properties of gold nanoclusters? How can the stability and reactivity of pure gold nanoclusters be compared to those doped with titanium and platinum? Which applications in nanotechnology and medicine are most affected by the unique properties of gold nanoclusters, both pure and doped? Therefore, we will explain more deeply and preferably through the chapters of our thesis as outlined.

Our thesis is organized as follows:

In our presentation of this thesis, we detail the most important points addressed in this thesis: Chapter 1: Researching and collecting previous studies of nanoparticles and detailing their smallest parts, grafted gold clusters and their various promising applications, which are

the current knowledge challenges for nano physicists, biomedical folding and cancer research, We will then focus on the theoretical background of DFT simulation using one of the famous SIESTA codes that we have adopted in this work. We will also briefly discuss the linear time-dependent response sensitivities of TDDFT using GAUSSIAN to gain a deeper understanding of the optical absorption properties and explore the advantages of such precious and effective metals for medical detection and optimization applications in Chapter 2.

The results are presented and discussed over the course of the next two chapters. In Chapter 3,4. We will present the different structures of pure and doped gold clusters obtained from DFT calculations as well as investigations into cluster structure, electronic, and optical properties, using quantum mechanical methods.

TDDFT calculations of the most stable structures of the studied clusters, such as changes in optical absorption spectra, excitation energies, and oscillator strength. Finally, in the conclusion of this thesis, we summarize the success of these methods in describing and studying the finest molecules that help us understand and discover new active materials that may be the cradle of improved detection methods for cancer and malignant diseases, as well as suggesting possible avenues and future aspirations.

FUNDAMENTALS

Chapter1

1. Literature Review

Introduction and motivation:

We will provide a succinct overview of earlier research on noble metal gold clusters in this chapter. We will summarize the primary areas of work that we have completed thus far: structural, magnetic, and optical calculations. Recent years have seen significant advancements in nanoscience and related technologies across a wide range of scientific disciplines **[21]** and have witnessed great progress in various aspects of life and the broad field of materials science, computer science and engineering, physics, medicine, and chemistry... etc.

This chapter will concentrate on nanotechnology methods in the domains of physics, materials science, and biomedicine:

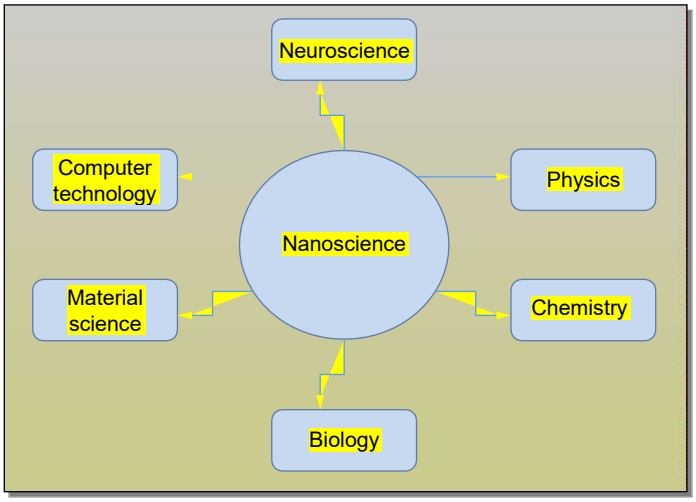

Figure 1: Relationship between nanoscience and major fields [22]

1.1. Nanotechnology revolution:

Nanotechnology encompasses a wide range of materials, devices, and applications that involve nanoscale phenomena. It involves the manipulation of materials at the nanoscale in terms of physical dimensions that are defined in terms of nanometers (one billionth of a meter (10^{-9} m), including devices, structures, and systems with new features and functions resulting from the arrangement of atoms on a scale between 1 and 100 nanometers**[22]** The field of Nanotechnology grew out of the desire to understand and control matter at the atomic and molecular levels, leading to the development of new materials and technologies with unique properties and applications **[23]**.

1. Literature Review

The word "nano," derived from a Greek word meaning "very small," is the birthplace of nanotechnology, the study of systems with very small dimensions. It combines chemistry, materials science, and biology. Although the exact origins of nanotechnology are unknown, Richard Feynman is widely regarded as its father. Nanomaterials were already being used in medicine before Feynman. In 1449, John Utynam filed the first patent for glass containing gold nanoparticles [24].

Nanoparticles of noble metals have received great attention in the research community, as nanoscience and nanotechnology, which control structural properties such as shape, size, and crystallinity, have been characterized by unique properties [25]. It emerged mainly in the medical field to successfully deliver the drug to a specific target, investigate the structure of DNA, protein detection, tissue engineering, detection, and destruction of pathogens and cancer cells, or malignant cancer cells, it is a promising tool after it has proven itself through various technical models in vitro and in vivo, has clinical efficacy; this has been successfully achieved through advances in nanotechnology[26].

1.1.1. Metal nanostructures:

Nanostructured metals are highly sought after due to their small size and superior properties, making them suitable for various applications. Their increased surface area to volume ratio and significant percentage of surface atoms make them advantageous in catalytic reactions. They are also being used in electrochemical sensing for developing next-generation non-enzymatic glucose sensors. The correlation of metal nanostructures to electrocatalytic properties is being studied to enhance performance [28,29]

The correlation study of metal nanostructures has received attention from researchers due to their unique catalytic properties for mass transfer and electron transfer kinetics[30,31,32].In particular, the use of nanostructures for noble metals such as gold (Au), Palladium (Pb), Platinum (Pt), Nanometals, and copper metals is of particular interest [31].

1.1.2. Classifications of Nanoparticles:

Nanoparticles (NPs) are a unique type of nanomaterial with sizes ranging from 1 to 100 nm, and have unique physical and chemical properties due to their small dimensions. It can also be classified according to its nature, shape, and dimensions [32].

Nanoparticles are categorized into different types based on their shape and size. This categorization helps in understanding their unique properties and applications. Some important categories of nanoparticles are mentioned in the review

- organic nanoparticles

- inorganic nanoparticles (such as metal and metal oxide nanoparticles),
- ceramic nanoparticles
- carbon nanoparticles (such as fullerenes, carbon nanotubes, graphene, etc.).

Each class of nanoparticles offers distinct properties that make them suitable for diverse fields ranging from medicine to electronics and environmental science **[32]**

1.1.3. Classification of nanomaterials based on dimension:

Paul Ehrlich once referred to nanomaterials as "Magic Bullets" (Kreuter 2007). These materials are among the most extensively studied materials of the 20th century, and their discovery gave rise to a brand-new scientific field known as nanotechnology (Nasir Khan et al. 2017) **[33]**

Chemical compounds or materials that are produced or utilized at a microscopic scale are known as nanomaterials. In fact, the term "material" refers to an infinite set of elements that together demonstrate an average statistical performance. The performance of nanomaterials is therefore influenced by particular interface effects and exhibits properties that are influenced by the limited size and number of constituents (Guo et al. 2014)**[34]**. This classification is greatly reliant on the electron association along the dimensions of the nanomaterials **[32]**

❖ **Zero-dimensional (0-D):**
- These nanomaterials are characterized by being amorphous or crystalline and exist as single-crystalline or polycrystalline nanoparticles.
- Examples include nanoclusters that are sphere-shaped nanostructures with dimensions ranging from 1 to 100 nm in all space-based directions.

❖ **One-dimensional (1-D):**
- 1-D nanomaterials can be either amorphous or crystalline and include nanotubes, nanowires, nanofibers, and nanorods.
- They have electrons that can shift along a single axis, typically less than 100 nm in size.

❖ **Two-dimensional (2-D):**
- These nanomaterials are amorphous or crystalline and include nanofilms, dendrimers, nanolayers, and nanocoatings.
- Electron associations in 2-D nanomaterials occur along the x and y-axes.

❖ **Three-dimensional (3-D):**
- 3-D nanomaterials are typically crystalline and include quantum dots, fullerenes, nanoparticles, nanocrystals, and colloids.

- Electron associations in 3-D nanomaterials occur along the x, y, and z-axes[25]

In general, nanomaterials exhibit unique surface effects compared to fine or bulk materials due to several factors. First, nanomaterials have a much larger surface area and a greater number of particles per unit mass. Second, the fraction of atoms on the surface increases in nanomaterials.

Third, atoms on the surface of nanomaterials have fewer immediate neighbors. These differences in surface properties lead to changes in the chemical and physical properties of nanomaterials. For example, the lower binding energy per atom on the surface affects the melting temperature, making it lower in nanomaterials compared to bulk materials. The larger surface area and surface-to-volume ratio also increase the reactivity of nanomaterials and have significant effects on their structure. However, it is important to prevent agglomeration and aggregation of nanomaterials, as this can negatively affect their surface area and nanoscale properties. Increasing the zeta potential can help prevent agglomeration [35]

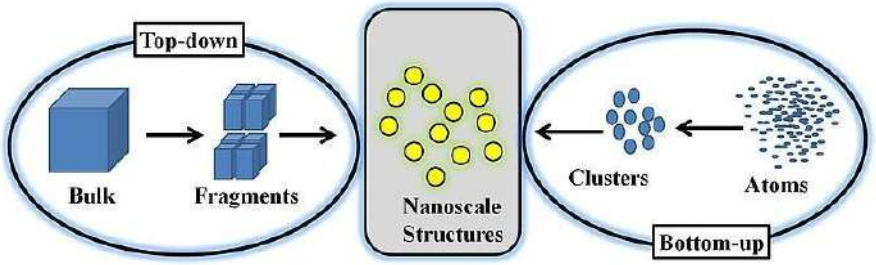

Fig.2 A representative diagram showing the model of nanoscale structure (Source:nanoscience.com). Top-down/Bottom-up approach[36]

1.1.4. Biomedical Metals clusters:

Metal nanoclusters (NCs) have received much attention due to their unique properties. These nanoclusters, composed of several to tens of atoms with a core size of less than 2 nanometers, exhibit discrete energy levels and particle-like properties. For example, they demonstrated HOMO-LUMO transitions, tunable luminescence, large Stokes shifts, quantum charging, molecular chirality, and magnetism. [37], [38], [39]

In recent applications, metallic NCs such as gold (Au), silver (Ag), and copper (Cu) NCs have been widely used in biosensing, labeling, imaging, and therapeutics. Their ultrafine size, narrow size distribution, good image stability, and biocompatibility make them superior to larger nanoparticles (NPs) in biomedical contexts. Notably, metallic NCs can be

eliminated from the body efficiently without causing severe side effects, unlike larger NPs that may accumulate in organs such as the liver and spleen. These properties position metal NCs as promising candidates for various applications, including electrocatalysis, bioanalysis, imaging, and targeted drug delivery [37], [40]

1.2. Nanocluster and Noble Metal:

Nanoclusters are a collection of a few atoms, typically between a few and about 100 (1-3 nanometers in size), occupying the interesting regime between isolated atoms and bulk materials. Unlike larger nanoparticles, nanoclusters exhibit discrete electronic states and size-dependent properties, governed by quantum confinement effects. Their behavior is not fully described by molecular orbital theory or solid-state physics, making them a unique arena for fundamental research and technological applications.

Table 1. Distinction from Nanoparticles:

Feature	Nanocluster	Nanoparticle
Size	<2 nm	2-100 nm
Electronic structure	Discrete energy levels (molecular-like)	Quasi-continuous bands (bulk-like)
Optical behavior	No plasmon resonance; photoluminescent	Surface plasmon resonance
Stability	Often governed by "magic numbers"	Size-dependent, less discrete

1.2.1. Relevance to Noble and Precious Metals:

- Nanoclusters of Au, Ag, Pt, and Cu are of particular interest due to:
  - High surface-to-volume ratios enhance catalytic activity.
  - Size-tunable optical properties are useful in sensing and imaging.
  - Superatom behavior, where clusters mimic atomic electronic configurations (e.g., $Au_{52}(SR)_{18}$ with 8 valence electrons behaves like a noble gas[41], [42]
- These clusters are synthesized via methods such as:
  - Ligand-protected reduction (e.g., Brust-Schiffrin method)
  - Gas-phase condensation
  - Laser ablation and molecular beam techniques[43]

1.3. Gold (Au) and doped Clusters in DFT Simulations:

1.3.1. Gold (Au) Cluster:

Gold nanoclusters have received significant attention due to their unique quantum

confinement effects. Their size- and shape-dependent electronic, optical, and catalytic properties are a direct result of quantum confinement effects and a high surface-to-volume ratio **[44], [45].** Unlike chemically inert gold, small gold clusters exhibit remarkable catalytic activity in a variety of reactions, producing discrete electronic states and enhanced optical properties. Density functional theory (DFT) simulations have played a key role in exploring their structural, electronic, and vibrational properties. DFT enables the prediction of stable geometric structures, electronic band gaps, ionization potentials, electron affinities, and vibrational frequencies, providing important insights into their stability, interaction, and interactions with molecular species at the atomic level **[46]**. Studies show that ultrasmall gold clusters (typically <2 nm) exhibit size-dependent HOMO-LUMO gaps, photoluminescence, and catalytic behavior, making them promising candidates for applications in nanophotonic and biomedicine**[47]**

1.3.2. Doped gold clusters (Ti;Pt):

The strategic incorporation of foreign atoms into gold cluster frameworks results in doped gold clusters, which represent an effective means of tailoring and enhancing their intrinsic properties, thereby unleashing new functionalities not observed in pure gold counterparts. Doping gold clusters with transition metals such as titanium and platinum significantly modifies their electronic and catalytic properties, charge distribution, active site availability, optical responses, and improved stability. For example, the introduction of platinum (Pt) atoms into gold clusters can significantly improve their catalytic performance, often by promoting specific reaction pathways, modifying the adsorption energies of reactants, or enabling bifunctional catalysis through synergistic effects between gold and platinum sites **[48]** Similarly, the inclusion of titanium (Ti) or other transition metals can lead to unique electronic interactions or create new active sites for specific chemical transformations, particularly in redox reactions or photocatalysis, due to the diversity of oxidation states and electronic configurations of Ti **[49]** DFT simulations are essential for understanding these complex activation effects. They enable a systematic search for preferred activation sites, the effect of activator concentration on the cluster's stability and electronic properties (e.g., density of states, charge transfer), and the identification of active sites for specific chemical reactions. By accurately modeling the local atomic environment and electronic interactions, DFT simulations can predict how platinum and titanium atoms modify the reactivity of gold clusters, guiding experimental synthesis toward functional materials desired for catalysis, sensing, and other applications. **[50]**

1.3.3. General Distinctive Properties when using DFT:

- **Atomistic Level Understanding:** DFT provides the unique ability to probe properties at the atomic and electronic level, which is difficult or impossible to achieve purely experimentally. This includes precise atomic positions, bond lengths, charge distributions, and magnetic moments.
- **Predictive Power:** DFT allows for the prediction of new materials, stable configurations, and their properties before experimental synthesis, guiding experimental efforts.
- **Mechanism Elucidation:** For catalytic reactions, DFT can map out entire reaction pathways, identify transition states, and calculate activation energies, providing insights into reaction mechanisms.

1.3.4. Interaction of Gold Nanoclusters with Biological Molecules:

DFT investigations reveal that gold nanoclusters strongly interact with nucleic acid bases, such as guanine and guanine-cytosine base pairs, with substantial charge transfer occurring upon binding. These interactions influence the electronic properties of the clusters and are important for potential biomedical applications, including drug delivery and biosensing**[51]**

1.3.5. Size-Dependent Structural and Electronic Properties of Gold Clusters:

DFT studies have extensively characterized how the size and geometry of gold clusters (from a few atoms up to several tens) influence their structural stability, binding energies, and electronic properties. These size-dependent effects are crucial for tailoring cluster properties for nanotechnological applications**[52]**

1.3.6. Gold Bulk, Crystal Structure with physical properties:

Gold (Au), a noble metal in Group 11 (Transition Metals), exhibits exceptional stability and distinctive properties rooted in its electronic configuration ([Xe] $6s^1 4f^{14} 5d^{10}$) and face-centered cubic (FCC) crystalline lattice. Its bulk structure (lattice parameter *a* = 4.078 Å at 298 K) is characterized by close-packed atomic planes (e.g., {111}) that dictate its high ductility, electrical conductivity (4.52×10^7 S/m), and thermal conductivity (318 W/m·K)[53].The relativistic contraction of Au's 6s orbital, due to high nuclear charge and electron velocity (~0.58*c*), shortens interatomic bonds (2.88 Å in bulk) and elevates its work function (~5.1 eV), explaining its chemical inertness and resistance to oxidation. **[54]**
At the nanoscale, gold's properties diverge sharply from bulk behavior. While bulk Au exhibits a characteristic plasmon resonance at ~520 nm (arising from collective d-band to sp-band transitions), finite-size effects in clusters (<2 nm) quantize electronic states, suppressing plasmons in favor of molecule-like HOMO-LUMO transitions **[55], [56]**. This

shift is critical for applications in catalysis and optoelectronics, where Au's FCC stability permits precise engineering of defects (e.g., twin boundaries, stacking faults) to modulate mechanical strength and catalytic activity [57].

1.3.7. Distinctions from Bulk to Cluster:

1.3.7.1.Electronic Structure:

Bulk Au's $5d^{10}6s^{1}$ configuration yields a half-filled 6s band, enabling metallic conductivity. In contrast, small clusters (e.g., Au_{20}) exhibit discrete energy levels and semiconductor-like gaps (~1.5 eV)[58]

1.3.7.2.Thermodynamics:

The surface energy of bulk Au (~1.5 J/m²) dominates its stability, whereas clusters (<100 atoms) are governed by ligand interactions and quantum confinement[59]

1.3.8. Practical Applications of Size-Dependent Gold Nanoclusters:

1.3.8.1.Catalysis:

Gold nanoclusters exhibit exceptional catalytic activity that varies with size due to changes in surface atom coordination, electronic structure, and d-band center.

- CO Oxidation: Au_8 and Au_{20} clusters show high activity at low temperatures.
- Water-Gas Shift Reaction: Pt- or Cu-doped AuNCs enhance activity via synergistic effects.
- Electrocatalysis: Size-tuned AuNCs are used in fuel cells and hydrogen evolution reactions[60]

1.3.8.2.Optoelectronics and Photonics

Size-dependent optical absorption and emission make AuNCs suitable for:

- Light-Emitting Devices (LEDs): Tunable emission for white-light generation.
- Photodetectors: Enhanced sensitivity due to discrete energy levels.
- Nonlinear Optics: Used in second harmonic generation and two-photon absorption.

1.3.8.3.Chemical Sensing

The HOMO–LUMO gap and surface reactivity of AuNCs vary with size, enabling:

- Gas Sensors: Detection of NO_2, CO, and H_2S via changes in conductivity or fluorescence.
- pH and Ion Sensors: Fluorescence quenching or enhancement in response to environmental changes.

1.3.8.4.Quantum Devices and Superatoms

Certain AuNCs (e.g., $Au_{25}(SR)_{18}$) behave as superatoms, mimicking atomic orbitals:

- Quantum Dots: Used in quantum computing and single-electron transistors.
- Molecular Electronics: Serve as building blocks for atomically precise circuits.

1.3.8.5. Medical Detection:

a. **Biosensing and Diagnostics:** Specific examples of using AuNCs (pure and doped) for detecting biomarkers, pathogens, or diseased cells.
b. **Bioimaging:** In vivo and in vitro imaging (fluorescence imaging, CT contrast agents).
c. **Theragnostic:** Combining diagnostic and therapeutic capabilities (e.g., photothermal therapy, drug delivery)**[61], [62]** .

Chapter 2

2. Theory and Computational Methods

Introduction:

The characterization of the physical properties of materials is rarely executed with precision, owing to the intricate nature of these multiparticle systems. Indeed, the resolution of these so-called "N-body" problems must invariably resort to approximations, not solely to facilitate the computational processes but also to achieve a satisfactory representation of this exceedingly complex system. The methodologies for calculating the electronic structure based on Density Functional Theory (DFT) can be categorized into two distinct groups: the "all-electron" approach and the pseudopotential approximation. The former explicitly incorporates both core and valence electrons within the computational framework. Given that core electrons exhibit strong localization, these methodologies necessitate the utilization of suitable functions. As an application of quantum mechanics that aims to emulate genuine electronic behavior in a more accessible manner, we employ density functional theory**[63]**The inception of DFT can be traced back to 1920, initiated by Thomas and Fermi to address the "many-body problem," which is regarded as the most fundamental challenge within condensed matter theory. As a pragmatic application of quantum mechanics, to faithfully represent the authentic electronic system in a more streamlined fashion, we implement Density Functional Theory**[64]**

2.1. The Schrodinger Equation:

Condensed matter physics relies on the laws of quantum mechanics, based on solving The Schrödinger equation to model a many-body system of interacting nuclei N_n, and electrons N_e. The time-independent Schrödinger equation is given as:

$$\hat{H}\,\Psi(R, r) = E\Psi(R, r) \qquad 2.1$$

where R and r represent the position vectors of nuclei N_n and electrons N_e, respectively. The quantities E and Ψ(R, r)are the energy and wave function of the interacting electron-nucleus system, respectively. $\hat{H}$ is the Hamiltonian operator of the system**[65]** The following expression gives it:

$$\hat{T}e + \hat{T}n + \hat{V}ee + \hat{V}en + \hat{V}nn \qquad 2.2$$

where :

T^e: Kinetic energy of electrons

T^n : Kinetic energy of the nuclei

V^ee: Electron-electron interaction energy

V^en: Electron-nucleus interaction energy

V^nn: Energy of nuclei-nuclei interaction

Equation:

$$\hat{H} = -\sum_i \frac{\hbar^2}{2m_e} \cdot \nabla_{r_i}^2 - \sum_i \frac{\hbar^2}{2M_i} \cdot \nabla_{R_i}^2 - \sum_{i,j} \frac{Z_i e^2}{4\pi\epsilon_0 |R_i - r_i|} + \sum_{i \neq j} \frac{e^2}{8\pi\epsilon_0 |r_i - r_j|} + \sum_{i \neq j} \frac{e^2 Z_i Z_j}{8\pi\epsilon_0 |R_i - R_j|} \quad 2.3$$

The many-body system ($N = N_e + N_n$) makes it impossible to achieve analytical and numerical accuracy and solve the Schrödinger equation. Several approximations have been proposed to ease and simplify the calculations, such as the Born-Oppenheimer approximation, the Hartree-Fock approach, and density functional theory (DFT).

2.2. The Born-Oppenheimer (adiabatic) approximation:

The Born-Oppenheimer Approach (BOA) [66] is used as an initial methodological framework for the independent multibody treatment of the dynamics of electrons and nuclei by their separation.

This approximation is based on the observation that the mass of the nucleus exceeds the mass of the electron (Mn ≈1800 me), and it is inevitable, according to the principle of inertia, that the motion of the nuclei acts independently of the motion of the electrons. In light of this understanding, Born and Oppenheimer [66] assumed that nuclei are effectively stationary, in the sense that their positions remain fixed (R = cste), while electrons are in a constant state of motion.

Thus, the dynamics of electrons and nuclei are separate, leading to the conclusion that the kinetic energy of the nuclei T^e becomes null. The term encapsulating the electrostatic interaction V^nn between nuclei becomes constant, while the term V^ne depends on r_i. The Hamiltonian that arises from this approximation is expressed as follows:

$$\boldsymbol{H = -\sum_i \frac{\hbar^2}{2m_e} \cdot \nabla_{r_i}^2 + \sum_{i \neq j} \frac{e^2}{8\pi\epsilon_0 |r_i - r_j|} + V_{ext}} \quad 2.4$$

$$\boldsymbol{= \quad T \quad + \quad V \quad + V_{ext}}$$

Even with the use of approximations, a core challenge remains in quantum theory when determining the electron eigenvalues for a material: how do we rigorously derive these equations given the immense number of interacting electrons (on the order of $10^{\wedge 23}$) and the fact that the many-electron wavefunction depends on the coordinates of all N electrons?

2.3. The Hohenberg and Kohn Theorems (1964):

The concept of expressing a system's total energy as a functional of its electron density dates back to the Thomas-Fermi model (1927) **[63], [64]** a semiclassical approximation that neglects quantum exchange and correlations. It gained a rigorous theoretical footing with Hohenberg and Kohn's seminal 1964 work. Their pivotal theorems laid the cornerstone for modern Density Functional Theory (DFT), establishing that the ground-state electron density uniquely determines all ground-state properties of a many-electron system. This profound insight subsequently paved the way for Kohn and Sham's practical approach to calculating electronic structures, revolutionizing our ability to study complex materials. They proved two seminal theorems:

- The ground-state density uniquely determines the external potential (and thus all system properties).
- A universal energy functional exists, whose minimum yields the exact ground-state density

❖ Theorem 1

where they postulate that the total energy of a poly-electronic system in the ground state E is a unique charge density functional ρ(r) for a unique external potential $V_{ext}(\rho(r))$.
The total energy is written in the following form: F[ρ(r)] is a universal functional independent of the external potential, $V_{ext}(\rho(r))$.

$$E[\rho(\mathbf{r})] = F[\rho(\mathbf{r})] + \int \rho(\mathbf{r}) V_{ext}(\mathbf{r}) d^3r \quad (2.5)$$

Or

$$\mathbf{F[\rho(r)] = T[\rho(r)] + \hat{V}_{ee}[\rho(r)]} \quad (2.6)$$

$$EGS = E[\rho GS(r)] = E_{min}[\rho(r)] = \min\{F[\rho(r)] + \int \rho(r)V_{ext}(r)d^3r\} \quad 2.7$$

❖ **Theorem 2**

The minimum of the total energy functional $E_{min}[\rho(r)]$ corresponds to the ground state $EGS[\rho(r)]$ and the ground state particle density $\rho GS(r)$.

Note that the ground state energy is obtained through the application of the variational principle:

$$\frac{dE[\rho]}{d\rho} = 0 \quad 2.8$$

In practice, the two Hohenberg-Kohn theorems do not form a complete solution for the poly-electronic problem. The difficulty lies in expressing the universal functional $F[\rho(r)]$ independent of the external potential**[67], [68]**.

2.4. The Kohn-Sham Equations:

The Kohn-Sham (KS) theory, developed by Walter Kohn and Lu Jeu Sham in 1965, is a fundamental framework in density functional theory (DFT) that reformulates the many-body problem of interacting electrons into a more tractable non-interacting reference system. The key idea is to replace the complex interacting system with a fictitious system of non-interacting electrons that exactly reproduces the same ground-state electron density $\rho(r)$. while the remaining electron-electron interactions are lumped into an exchange-correlation term, which must be approximated **[68]** The approach reduces the complexity of solving the Schrödinger equation for interacting electrons, making DFT computationally feasible while maintaining accuracy. This allows for an exact expression of the kinetic energy of the non-interacting system, significantly simplifying calculations while retaining the essential physics. According to the formalism, the total energy functional

- For the non-interacting (Kohn-Sham) system can be written as:

$$E(\rho) = T_S(\rho) + \int [V_{eff}(r)]\rho(r)d^3r \quad 2.9$$

where:

- $T_s[\rho]$= Kinetic energy of the non-interacting electrons.

- $V_{eff}(r)$= Effective potential ensuring the same density as the interacting system.

- For the real interacting system (general form):

$$E[\rho]=T[\rho]+V_{ee}[\rho]+\int \rho(r)V_{ext}(r)\, d3r \quad 2.9$$

$$E[\rho] = T[\rho] + V_{ee}[\rho] + \int \rho(r)v_{ext}t(r)d^3r \quad 2.10$$

$$E[\rho] = T[\rho] + V_{ee}[\rho] + \underbrace{Ts[\rho] - Ts[\rho]}_{0} + \underbrace{Vs[\rho] - Vs[\rho]}_{0} + \int \rho(r)v_{ext}t(r)d^3r \quad 2.11$$

$$E[\rho] = Ts[\rho] + Vs[\rho] + \underbrace{T[\rho] - Ts[\rho]}_{Ec} + \underbrace{V_{ee}[\rho] - Vs[\rho]}_{Ex} + \int \rho(r)v_{ext}t(r)d^3r \quad 2.12$$

The final expression of the total energy in the Kohn-Sham method is expressed in the following form:

$$E[\rho] = Ts[\rho] + \underbrace{V_H[\rho]+Exc[\rho]+ V_{ext}t[\rho]}_{V_{ks}[\rho]} \quad 2.13$$

where:

- $T[\rho]$ = True kinetic energy of interacting electrons.
- $V_{ee}[\rho]$= Electron-electron interaction (Coulomb + quantum effects).
- $V_{ext}(r)$ = External potential (e.g., from nuclei).

The Kohn-Sham equations decompose the total energy: $Ts[\rho]$ is the non-interacting kinetic energy and the Hartree correlation term, and the EC correlation term is expressed as the difference between the true kinetic energy and that of an electron gas with no interaction; $V_H[\rho]$ is the classical Coulomb electron-electron (Hartree) repulsion; and $V_{ext}(r)$ is the electron-nuclei potential. All non-classical electron interactions and the remaining kinetic energy are absorbed into the crucial exchange-correlation term, $E_{XC}[\rho]$**[69].** This function, when approximated, enables practical DFT calculations. By identifying equations **2.8** and **2.13**, we obtain:

$$V_{KS} = \int V_{eff}(\mathbf{r})\rho(\mathbf{r})d^3r \qquad 2.14$$

The development of the effective Kohn-Sham potential in integral form can be written as:

$$V_{KS} = \int \rho(\mathbf{r})V_H d^3r + \int \rho(\mathbf{r})V_{ext}(\mathbf{r})d^3r + \int \rho(\mathbf{r})V_{XC}d^3r \qquad 2.15$$

The monoelectronic Schrödinger equations in the Kohn-sham approach can be written as:

$$\left[\frac{\nabla_i^2}{2} + V_{eff}(r)\right]\psi_i(r) = \varepsilon_i\psi_i(r) \qquad 2.16$$

The Kohn-Sham eigenstates obtained from solving these equations enable the reconstruction of the ground-state electron density through the following expression:

$$\rho(r) = \sum_{i=1}^{Ne} |\psi_i(r)|^2 \qquad 2.17$$

The Kohn-Sham framework describes a self-consistent loop where the electron density ρ(r) and the effective potential (sum of Hartree V_H, exchange-correlation V_{XC}, and external V_{ext} terms) are interdependent with the single-particle orbitals ψi(r). This nonlinear problem is solved iteratively, initializing with a trial density ρin(r)and cycling until convergence, ensuring the output density and potentials mutually agree. In the following, a Self-consistent algorithm for the solution of Kohn-Sham equations is presented in **Figure 2.1**:

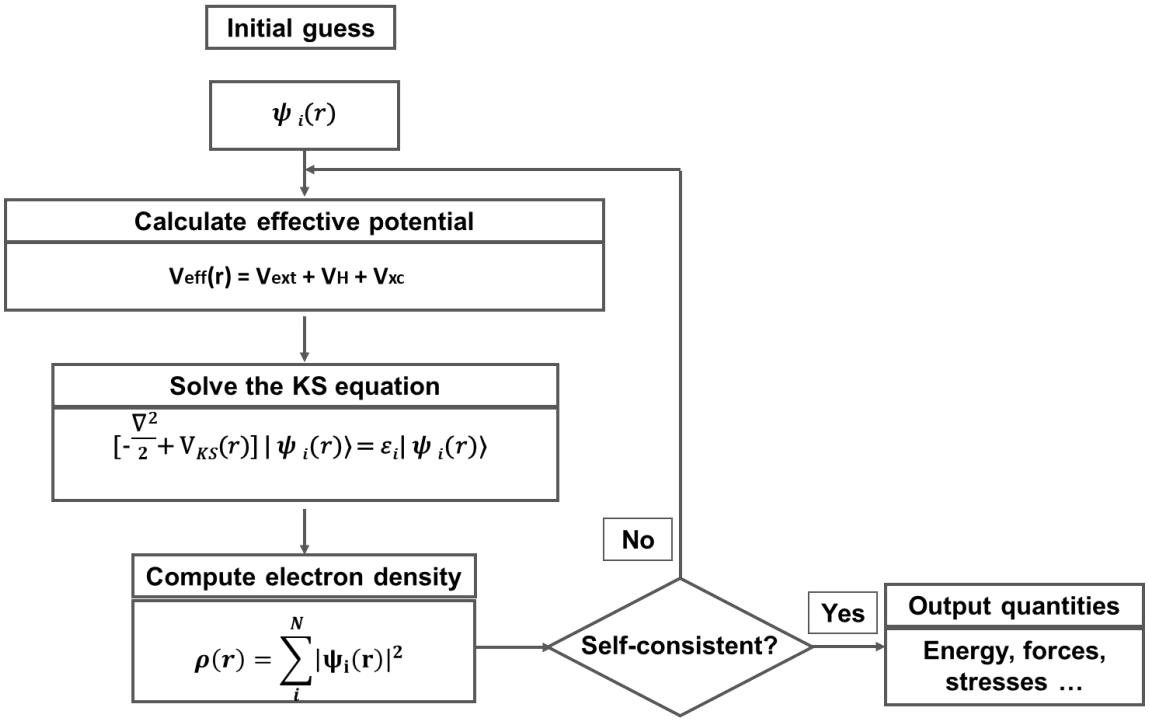

Figure .3 : Self-Consistency in Density Functional Theory[70]

2.5. Approximations to the exchange-correlation functional:

The exchange-correlation functional (E_{xc}) is the cornerstone of Density Functional Theory, encapsulating the intricate many-body effects of electron-electron repulsion and quantum mechanical exchange. As its exact form remains elusive, the accuracy of a DFT calculation hinges critically on the chosen approximation for E_{xc}. In the realm of computational materials science and quantum chemistry, two families of approximations have become ubiquitous due to their balance of computational efficiency and practical accuracy: the Local Density Approximation (LDA) and the Generalized Gradient Approximation (GGA).

2.6. LDA Local Density Approximation:

The Local Density Approximation (LDA), introduced by Kohn and Sham in 1965, simplifies the exchange-correlation functional $E_{XC}[\rho]$ by treating the electron gas as locally uniform. This means the exchange-correlation energy at any point is approximated by that of a homogeneous electron gas with the same local density. While effective for systems with slowly varying densities like metals, LDA often overestimates binding energies and underestimates band gaps in molecules and semiconductors. The term E_{XC} $[\rho]$will be written[68]:

$$E_{XC}^{LDA}[\rho(r)] = \int \rho(r)\varepsilon_{xc}[\rho(r)]d^3r \qquad 2.18$$

Where $\varepsilon_{XC}(\rho(r))$ denotes the exchange-correlation energy of an elementary volume d^3r for a homogeneous electron gas of uniform density $\rho(r)$.The E_{LDA} energy $[\rho(r)]$.

2.7. Generalized Gradient Approximation (GGA):

While Local Density Approximation (LDA) accurately predicts structural and mechanical properties for systems with slowly varying charge densities, it significantly underestimates band gaps and fails for inhomogeneous materials like oxides and transition metals. To overcome these limitations, the Generalized Gradient Approximation (GGA) was developed[71], incorporating the gradient of the electron density ($\nabla\rho(r)$) into the exchange-correlation functional. The expression for the resulting exchange-correlation energy is written as follows:

$$E_{XC}^{GGA}[\rho(r)] = \int \rho(r)\varepsilon_{xc}(\rho(r), |\nabla\rho(r)|)d^3r \qquad 2.19$$

This crucial refinement of the GGA allows the density inhomogeneity to be taken into account, leading to improved accuracy for a wide range of systems, including molecular geometries, reaction energies, and surface properties, making the exchange part generally the Becke function (B), the correlation part the Li, Yang, and Parr (LYP) function or the Perdew-Wang function (PW) and Ernzerhof (E) with 86 and 91 variables. Wang (PW) and Ehrenzerhof (E), with variables 86 and 91, hybrid functions like PBE and BLYP are standard tools in computational physics and chemistry. Hence, the keywords PBE, BLYP, BPW86, and BPW91 [72]

2.8. Pseudopotential methods:

Pseudopotential methods simplify the N-electron problem by distinguishing between chemically inert core electrons and reactive valence electrons. Core orbitals, localized and energetically deep, exhibit strong oscillations near the nucleus, making them computationally demanding to represent with plane waves. In contrast, valence orbitals extend farther and primarily govern chemical interactions. By replacing the full atomic potential with a smoother, fictitious pseudopotential, this approach reduces the number of equations in the Schrödinger framework. As a result, it significantly improves computational efficiency and lowers memory demands in ab initio simulations [73].Three main pseudopotential formulations are commonly used in electronic structure calculations:

- The pseudo-potentials with conserved norm introduced by Hamman et al [74]

- The ultra-soft pseudo-potential introduced by Vanderbilt **[75]**
- The "dual-space Gaussian" pseudo-potentials introduced by Goedecker et al**[76], [77]**

The criteria for satisfying the building blocks of these types of pseudopotentials:

- It must be smooth and not contain any knots, i.e., this minimizes the number of plane waves describing the evolution of wave pseudopotentials.
- Must be additive, i.e., the total effective potential must be the sum of the atomic pseudopotentials when there are multiple atoms.
- It must be transferable, meaning that the pseudopotential generated for a given atomic distribution should reproduce the calculations of all electrons in the environment in which it was generated, but we would also like it to reproduce the calculations of all electrons in different environments.

a. Norm-conserving pseudopotential:

The conserving pseudopotential method, pioneered by Hamann **[78]**, and further developed by Trullier and Martens **[79]**, is an advanced technique based on solving the Kohn-Sham equations. Its basic approach is based on manipulating the radial part of the electron wave function, (r)) for an isolated atom. The basic concept is to construct a pseudo-wavefunction that exactly matches the real AE wavefunction beyond a certain cutoff radius, while maintaining greater smoothness and no knots in the nucleus region. More importantly, it ensures that the norm (the quadratic wave function integral) of the semi-wave remains identical to that of the full electron wave function within the radius of the cut**[80]**n beyond a certain cutoff radius, while maintaining greater smoothness and no knots in the nucleus region. More importantly, it ensures that the norm (the quadratic wave function integral) of the semi-wave remains identical to that of the full electron wave function within the radius of the cut**[80]**

The general form of the atomic wave function $\Psi(n, l, m) = R(r)Y_{l.m}(\theta,\varphi)$ is approximated by a knotless semi-wave that preserves the logarithmic derivative and first energy derivative of the real solution, preserving the total charge, and ensuring excellent portability across different chemical environments. This enables the use **[81], [82]**onally efficient basis sets, such as plane waves, by eliminating the need to describe the rapidly oscillating fundamental electron orbitals. Where **n, l,** and **m** represent, respectively, the principal quantum number, angular momentum, and spin momentum. $Y_{l.m}(\theta,\varphi)$ are the spherical harmonics**[81], [82]**

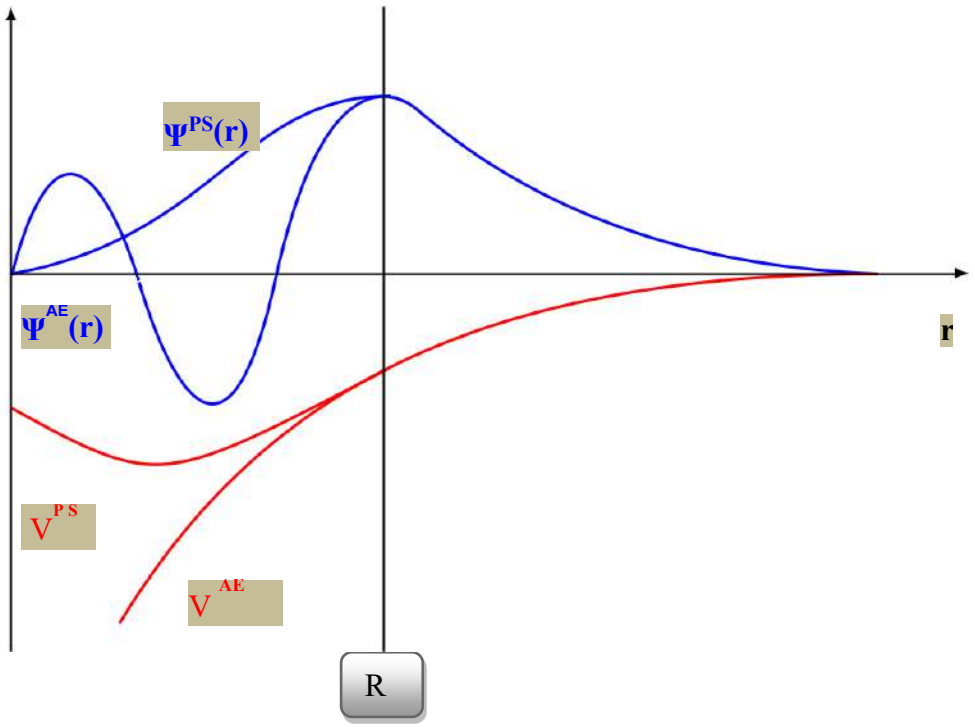

Figure.4 Shapes of the all-electron potential V^{AE}, the pseudopotential V^{PS}, and their wave functions Ψ^{PS}, Ψ^{AE}, respectively. Rc is the cut-off radius separating the core zone from the valence zone.

b. Norm-Rolaxed pseudopotential:

Relaxed-norm pseudopotentials, introduced by Vanderbilt, differ from norm-conserving methods by not strictly upholding the norm conservation condition[83]. This approach focuses on generating exceptionally smooth pseudowave functions within the core region, specifically designed to be free of nodes. The advantage of this smoothness is a considerable reduction in the required cutoff energy, as it permits the use of a larger cutoff radius compared to norm-conserving pseudopotentials. This is particularly beneficial for accurately describing localized orbitals. However, a consequence of this method is that the generated wave functions do not fully account for the system's total charge density, necessitating an increase in the electron density around atoms to compensate for the missing portion. Despite this, Vanderbilt's approach, particularly in the form of ultrasoft pseudopotentials (USPPs), is highly advantageous for ab-initio calculations, especially when

dealing with transition metals[73], [75]. Their primary benefit lies in their rapid convergence with respect to cutoff energy, which directly translates into reduced computational time and memory consumption. Nevertheless, USPPs do have drawbacks, including the difficulty of generating them for certain types of materials and potential issues with transferability for some systems, notably those with high magnetic moments[84]

2.9. LCAO approximation method:

The LCAO approximation, established by Lennard-Jones in 1929, models molecular orbitals as a superposition of constituent atomic orbitals due to the analytical intractability of molecular electronic functions To Together, these methods, DFT with advanced pseudopotentials and LCAO basis sets, provide practical frameworks for electronic structure calculations, despite inherent trade-offs in accuracy, system dependence, and functional selection. This method expresses a molecular wavefunction Ψ as a linear combination of n atomic orbitals $_i$ from the molecule's atoms:

$$\Psi \Sigma_{i=1}^{n} C_i \varphi_i \qquad 2.20$$

In the LCAO approximation, the term quantifies the contribution of each atomic orbital to a given molecular orbital, where is its corresponding coefficient. Solving the Schrödinger equation within this framework necessitates computing approximately n^4 integrals, with n representing the total number of atomic orbitals in the system.

2.10. Success and Limits of Density Functional Theory:

The accuracy of *ab initio* DFT hinges on the exchange-correlation functional, with LDA and GGA performing well for ground states in diverse systems like metals and transition metals. However, these approximations struggle with non-local correlations, such as van der Waals interactions, and consistently underestimate band gaps (30-50%) in insulators and semiconductors. While DFT reliably predicts ground-state properties (e.g., geometries, vibrations) for diverse systems, its limitations include ad hoc functional selection, poor treatment of dispersion forces, and inaccessibility of excited states without time-dependent (TDDFT) extensions. Vanderbilt's ultrasoft pseudopotentials (USPP) complement DFT by enhancing computational efficiency for transition metals via relaxed norm conservation, albeit at the cost of reduced transferability in magnetic or complex systems. Together, these methods balance efficiency and accuracy but require careful validation for material-specific challenges.

2.11. Exploring TDDFT theory of excited states and optical properties:

The ability to accurately predict and understand the behavior of matter at the atomic and molecular levels is a fundamental element of contemporary science, underpinning developments in everything from materials science and catalysis to quantum technologies **[86].** Electronic structure theory, which aims to solve the fundamental many-electron problem of quantum mechanics, is at the center of this effort. Due to its exceptional balance between computational efficiency and accuracy in describing the ground state, density functional theory (DFT) has become a vital and widely used method**[87]** DFT has made it possible to gain previously unheard-of insights into molecular geometry, reaction mechanisms, and the structural and mechanical properties of solids by substituting the simpler electron density as the fundamental variable for the more complex many-body wavefunction **[67]** Nonetheless, systems in excited states are the source of the vast majority of remarkable natural and technological phenomena, particularly in fields such as light-matter interaction. The dynamic response of electrons to external perturbations controls photochemistry, light absorption and emission, and the emergence of plasmonic resonance in nanostructured materials. Although the DFT ground state offers a great starting point, these non-equilibrium dynamical processes cannot be directly described by its inherent formulation. Due to this constraint, DFT must be extended to the time domain.**[67], [70]**

To overcome these constraints, Time-Dependent Density Functional Theory (TDDFT) has emerged as a powerful extension, enabling the study of dynamic and optical responses critical to understanding nanoscale systems**[88]** Gold nanoclusters, in particular, present an intriguing platform due to their size-dependent electronic structure and tunable optical characteristics **[89]** This study investigates how TDDFT can address the limitations of conventional DFT in modeling excited-state behaviors, focusing on optical absorption spectra, charge-transfer excitations, and transition dipole moments. By systematically exploring TDDFT formulations and comparing them against ground-state DFT predictions, we aim to illuminate the theoretical boundaries and potential enhancements necessary for accurate excited-state simulations of gold-based nanomaterials **[90]**

2.12. Time-Dependent Density Functional Theory (TDDFT):

Time-dependent Density Functional Theory (TDDFT) provides precisely this crucial extension to ground-state DFT, enabling the accurate prediction of excited-state properties. Grounded in the Runge-Gross theorem, TDDFT accounts for the evolution of electronic

systems under time-dependent perturbations. Through its linear-response formulation, it has become the benchmark for simulating excitation energies, oscillator strengths, and optical phenomena such as UV-Vis absorption spectra. In the context of nanoscience, particularly for gold nanoclusters, TDDFT's favorable computational scaling enables the study of complex systems where quantum confinement and surface effects significantly influence the optical response. These capabilities make TDDFT not only a theoretical tool but a practical framework for exploring the limitations of conventional DFT and proposing enhanced methodologies for simulating nanoscale optical phenomena. Its computational scaling makes it uniquely suited for studying larger and more complex systems.

a. The Runge-Gross Theorem for Excited States:

The Runge-Gross (RG) theorem serves as the foundational principle of time-dependent density functional theory (TDDFT), extending the Hohenberg-Kohn theorem to time-evolving systems. Formulated in 1984**[91]**It rigorously establishes a unique one-to-one mapping between the time-dependent external potential (up to a time-dependent constant) and the time-dependent electron density, contingent upon a specified initial many-electron wavefunction and the Taylor expandability of the density around the initial time. This fundamental mapping implies that all system properties are uniquely derivable from the evolving density and initial state**[92]** However, the practical application of TDDFT to excited-state dynamics necessitates careful attention to challenges such as the precise preparation of initial excited states, the treatment of inherent degeneracies, and the ongoing development of advanced exchange-correlation functionals capable of accurately describing complex, time-dependent electronic behavior beyond the ground state**[93]**

Where:

- An initial many-electron wavefunction Ψ_0
- The assumption that the external potential $\mathbf{V(r,t)}$is Taylor-expandable around $\mathbf{t=0}$.
- The electron density $\boldsymbol{\rho(r,t)}$ is also Taylor-expandable.**[90]**

b. Time-Dependent Kohn-Sham Equations:

The Time-Dependent Kohn-Sham (TDKS) equations are a central component of TDDFT, offering a computationally tractable way to describe the time evolution of many-

electron systems. The TDKS equations are derived from the Runge Gross theorem, which guarantees that the time-dependent electron density uniquely determines the external potential (up to a time-dependent constant). This allows us to replace the complex many-body problem with a set of non-interacting single-particle equations that produce the same density.

The TDKS equations are a set of coupled, nonlinear, single-particle Schrödinger-like equations for the time-dependent Kohn-Sham orbitals, {**Φi(r,t)**}, evolving under[94] :

$$\boldsymbol{H_{KS}[\rho(r,t)]\Phi_i(r,t) = i\frac{\partial}{\partial t}\Phi_i(r,t)} \qquad 2.21$$

- Where: ***Φi(r,t)***are the time-dependent Kohn-Sham orbitals.
- is the time-dependent Kohn-Sham Hamiltonian.

c. Exchange-Correlation Functional in TDDFT:

The exchange-correlation (XC) functional lies at the heart of Time-Dependent Density Functional Theory (TDDFT), but its explicit time dependence introduces significant challenges. Since the Runge–Gross theorem of 1984 established that a system's time-dependent density uniquely defines its potential, researchers have devoted considerable effort to devising practical XC approximations. In the early 1990, the adiabatic approximation, which applies ground-state XC functionals at each instant, gained popularity due to its simplicity. A prime example is the Adiabatic Local Density Approximation (ALDA). However, by ignoring memory effects and frequency dependence, adiabatic TDDFT often fails for high-frequency excitations and strongly correlated systems, as highlighted in the work of Gross, Burke, and co-workers around 2005. To address these shortcomings, non-adiabatic methods emerged in the 2000. Vignale and Kohn (1996) introduced a current-dependent XC functional that captures some memory effects, and Ullrich and collaborators (2011) extended this idea to produce frequency-dependent kernels. These developments have proven vital in fields such as ultrafast laser spectroscopy and plasmonics, where dynamic electron correlations are crucial**[95].** More recently, hybrid schemes and machine learning techniques have been explored to enhance accuracy further. Maitra and colleagues (2010) investigated exact-exchange kernels, while Burke's group in the 2020s has applied data-driven models to construct more reliable frequency-dependent

XC functionals, particularly for charge-transfer excitations. Despite these advances, a universally accurate XC functional remains elusive. Most quantum-chemistry packages (e.g., Gaussian, VASP) still rely predominantly on adiabatic formulations because non-adiabatic corrections carry a hefty computational cost, but non-adiabatic corrections are indispensable when probing phenomena on attosecond timescales or in systems with pronounced dynamical correlation **[96], [97]**

❖ **Adiabatic Approximations**

The adiabatic approximation, being the most common and computationally affordable scheme in TDDFT, assumes that the exchange correlation potential at time t is determined solely by the electron density ρ(r,t) at that same instant, thereby omitting any dependence on the system's history**[98], [99]**.

$$\boldsymbol{V_{xc}^{adia}[\rho(r,t)] = V_{xc}^{GS}(\rho(r,t))} \qquad 2.22$$

where is an exchange-correlation potential derived from a ground-state DFT functional (e.g., LDA, GGA, or hybrid functionals like B3LYP). They are relatively inexpensive to compute, as they simply reuse well-established ground-state functionals. This allows TDDFT calculations for systems with hundreds of atoms. Adiabatic functionals often provide remarkably accurate excitation energies for low-lying valence excited states, particularly those of single-excitation character. This has made linear-response TDDFT (which relies on adiabatic kernels) a standard tool for UV/Vis spectroscopy**[100], [101], [102]**.

❖ **Non-adiabatic (memory-dependent) approximations**

In time-dependent density functional theory (TDDFT), the limitations of purely adiabatic functionals are overcome, where the exchange-correlation (XC) potential at each instant is determined solely by the instantaneous electron density. Although this adiabatic treatment is computationally efficient and adequate for many applications, it fails to capture memory effects and double excitations**.** By incorporating an explicit dependence on the time history of the electron density or current, non-adiabatic schemes restore the missing frequency dependence and properly account for dynamic correlation**[103], [104]**.

2.13. Linear Response Theory and Excited States:

Time-Dependent Density Functional Theory (TDDFT) employs linear response theory to determine how a system's electron density reacts to a small, time-dependent perturbation, typically an oscillating electric field that mimics electromagnetic radiation**[105], [106], [107]**. Solving the TDDFT response equations, often via the Casida formalism, yields excitation energies and oscillator strengths, which together construct an absorption spectrum. To reduce computational effort, the Tamm-Dancoff approximation (TDA) may be applied; this generally has a negligible effect on predicted excitation energies and intensities for many systems**[108], [109]**. As a frequency-domain method, TDDFT (also called LR-DFT) calculates vertical excitation energies with an accuracy of about 0.3 eV at relatively low computational cost, making it well suited for modeling electronic absorption spectra. TDDFT, grounded in the Runge-Gross theorem **[106]**, however, TDDFT's accuracy depends strongly on the chosen exchange-correlation (XC) functional and suffers from systematic errors, most notably, the underestimation of charge-transfer (CT) excitation energies and an incorrect description of ground-state conical intersections **[101], [106], [110], [111], [112]**. For noble metal nanoparticles, including pure and Ti/Pt-doped Aun clusters, TDDFT is essential to model surface plasmon resonance (SPR) and CT excitations accurately. Simplifications such as the Tamm-Dancoff approximation (TDA) are commonly adopted, where TDDFT modeling of the optical response of critical materials with tailored properties is used for advanced biosensing and biomedical applications.

2.14. DFT/TDDFT implemented via SIESTA and Gaussian for property calculation:

2.14.1. SIESTA:

SIESTA code, "Spanish Initiative for Electronic simulations with Thousands of atoms " is a computational method designed to study ground-state properties of materials within the framework of density functional theory (DFT). It enables the calculation of energy-volume relationships, phase diagrams, phonon spectra, and molecular dynamics.**[113]**. Since its initial development, advances in computational power have significantly expanded its applicability, allowing simulations of systems containing more than a thousand atoms. In this work, we employed the Fortran 95 implementation of SIESTA. Also relies on the concept of periodic boundary conditions (PBCs), where the system is represented by a repeating unit cell.**[114], [115], [116]** To define such a cell, one specifies the three lattice vectors (including their magnitudes and relative angles) and the atomic positions within the cell. This approach is well-suited for crystalline solids, where periodicity

is a natural feature. However, when studying finite systems such as molecular clusters, the use of PBCs introduces artificial replicas of the system in neighboring cells**[117]**. To avoid unphysical interactions between the cluster and its periodic images, the simulation cell must be chosen sufficiently large so that the replicas are effectively isolated. This ensures that the calculated properties reflect the intrinsic behavior of the cluster rather than artifacts of the boundary conditions.

a. Program execution:

To run a calculation with the SIESTA program, three essential components are required:

- **Input File (.fdf):** This flexible data format file contains all simulation parameters, including system geometry, calculation settings, and basis set details**[113], [118]**.
- **Pseudopotential Files:** These files (commonly in .psf, vps, or ASCII format) provide the necessary atomic pseudopotentials for each element in the system, ensuring accurate treatment of core electrons **[113], [119]**.
  - ✓ **VPS:** (Valence Pseudo Potential, binary format) is common in older versions or for computationally efficient inputs.
  - ✓ **PSF:** (PSeudoFile format, ASCII) is easily readable and portable.
  - ✓ **PSML:** (Pseudo Markup Language, XML-based, introduced in SIESTA 5.x and above) enables rich metadata and high transferability.
  - ✓ **ASCII:** Generic text-based format; retains readability and editability.
- **SIESTA Executable:** The compiled SIESTA program is needed to process the input and pseudopotential files and perform the calculation **[113], [119], [120]**.

Attention to detail in constructing and validating these core files ensures reliable, performant, and reproducible atomistic simulations. Whether your aim is basic materials discovery or frontier theoretical research, mastery of these requirements is the stepping stone to successful, high-impact simulations with SIESTA.

b. Basics:

SIESTA is a computational method based on localized atomic orbitals (Numerical Atomic Orbitals (NAOs) or Pseudo-Atomic Orbitals (PAOs). Uses atom-centered orbitals for reduced computational load and faster convergence, which enables efficient simulations due to its compact basis set and fast convergence. Unlike other methods with large basis

sets, SIESTA is well-suited for large systems without excessive computational cost.**[74], [113], [114], [121]**

c. Density Functional Theory (DFT): Implements the Kohn-Sham approach with:

- Local Density Approximation (LDA)
- Generalized Gradient Approximation (GGA)
- Non-local functionals, including Van der Waals (VDW-DF)

✓ **Norm-Conserving Pseudopotentials**: Employs the Kleinman-Bylander form for accurate atomic interactions.

✓ **Real-Space Grid Projection**: Calculates Hartree and exchange-correlation potentials by projecting wavefunctions and densities onto a real-space grid.

✓ **Linear Scaling Capability**: Supports linear combinations of localized orbitals (e.g., valence bond or Wannier functions), enabling simulations of hundreds of atoms on standard workstations.

of the linear computer with the number of atoms. Simulations with several hundred atoms are possible with modest workstations

d. Details of calculation:

Our calculations on pure and doped gold clusters were conducted within the framework of DFT, as implemented in the SIESTA code **[122], [123]** The exchange-correlation (XC) interaction was treated using the Generalized Gradient Approximation (GGA), specifically the Perdew-Burke-Ernzerhof (PBE) functional **[107]**. The study employed norm-conserving Troullier-Martins pseudopotentials generated by the ATOM code according to the Troullier-Martins scheme**[124]**, To ensure high accuracy, a double-zeta polarized (DZP) basis set was utilized, which was combined with a mixed basis set incorporating the effective core potential (DZ) cc-pVDZ-PP **[107], [113]**. solves the Kohn-Sham Hamiltonian for isolated pseudo-atoms**[71]**, accounting for the size, range, and radial shape of atomic orbitals . Structural optimization and electronic property calculations were performed by sampling only the gamma point (Γ), which was used for k-grid integration in the Brillouin zone. The convergence criteria were set to atomic units (10^{-5},10^{-6} u.a.) for the total energy and a stringent tolerance of 10^{-2} eV/atom for the interatomic forces, which were minimized using the conjugate gradient method **[87,117]** The real space mesh cut-off

was initially 250 Ry for the pure gold cluster optimization and was increased to 400Ry following the doping process. To effectively model the isolated nature of the clusters and prevent interactions with adjacent images, a large cubic supercell was employed: 40Å on the side for pure clusters and 1000Å for the Ti, Pt, and other-doped compound clusters, simulating a model. The validity of this computational methodology is established by reproducing and comparing our results with existing experimental and theoretical data.

2.14.2. Gaussian

The GAUSSIAN program is a widely used computational chemistry software package first developed in 1970 by John Pople and his team at Carnegie Mellon University (released as Gaussian 70). It employs Gaussian-type orbitals (GTOs) rather than Slater-type orbitals to enhance computational efficiency, especially for Hartree-Fock calculations on the limited hardware of the time. designed to perform ab initio, semi-empirical, and density functional theory (DFT) calculations. Continuously updated since its inception, the current version is Gaussian 16. Originally distributed through the Quantum Chemistry Program Exchange, it has been commercially developed and licensed by Gaussian. **[125], [126], [127]** since 1987. where TDDFT models the dynamic response of a quantum system to a time-dependent external perturbation, typically represented by an oscillating electric field. This field simulates the effect of incident electromagnetic radiation, mathematically analogous to illuminating the system with light.**[128], [129], [130]** In the context of nanocluster simulations, this approach enables the study of how electronic structures respond to optical stimuli. It offers a comprehensive computational platform for analyzing the electronic structure, molecular properties, and spectroscopic signatures of systems ranging from small molecules to nanoscale clusters. Its strength lies in the implementation of both ground-state and excited-state methodologies, enabling researchers to investigate structural stability, electronic excitations, and vibrational dynamics with high accuracy.

a. Program execution:

The computational protocol I provided previously should be combined into a single **input file**, typically saved with a **.com** or **.gjf** extension (e.g., **Au4_TDDFT.gjf**).

- **Input File (.com):** This flexible data format file contains all simulation parameters, including system geometry, calculation settings, and basis set details

- **Output file:** results to(**.log** or **.out**) files, and intermediate data **checkpoint file (.chk)**.
- **ECPs:** Effective Core Potentials for heavy atoms
- **Local Workstation / PC or HPC Cluster Execution:** This is the simplest way to run a job, ideal for smaller systems. Run the Gaussian program (g16) and use redirection and create the SLURM Submission Script (submit.sh) like our work (eg, **run g16.sh**)

Crucially, the TDDFT calculation is dependent on the optimized geometry. For efficiency, it is best practice to run the Optimization and the TDDFT calculation sequentially in the same input file using the **Opt...Freq** and then the TD keywords, along with the **Geom=Check Guess=Read** option for the excited state calculation.

b. Basics:

Gaussian basis sets are constructed from Gaussian-type orbitals (GTOs), which are mathematical functions centered on atoms. These can be used as primitives or combined into contracted functions to balance computational efficiency and accuracy. Popular families include atomic natural orbital, correlation consistent, polarization consistent, and Def2 basis sets, each optimized for different properties and levels of theory **[131], [132]**. Specialized basis sets exist for core properties, relativistic effects, and continuum states. The most critical aspects are treating relativistic effects and selecting a functional that correctly models the electronic transitions (interband d→sp and intraband sp→sp) that give rise to the optical spectrum. Selecting the functional and basis set is critical for accurate results, especially for noble metal clusters where plasmonic effects and d-electron transitions play a role. A Generalized Gradient Approximation (GGA) or meta-GGA functional like PBE or TPSS is a good starting point, as they are often used for larger noble metal clusters. For smaller clusters, or to account for charge-transfer excitations and improve accuracy, a hybrid functional like B3LYP or a long-range corrected functional like CAM-B3LYP may be benchmarked, although they are more computationally expensive. Studies often find that the choice of functional (especially the amount of HF exchange) is highly sensitive for these systems**[131], [133]**.

- **Minimal Basis Sets**

✓ Use the smallest number of functions necessary to represent each occupied atomic orbital, **STO-3G** (Slater-type orbital approximated by 3 primitive Gaussians).

❖ **Split-Valence Basis Sets**

✓ Represent valence orbitals with more than one function, allowing flexibility in describing bonding, **LANL2DZ, 3-21G, 6-31G, 6-311G**.

❖ **Polarized Basis Sets**

✓ Add extra functions (denoted by * or **) to allow orbitals to distort in response to bonding, **6-31G*** (adds polarization functions on heavy atoms).

❖ **Diffuse Basis Sets**

✓ Include functions with very small exponents to describe electrons far from the nucleus, **6-31+G*** (adds diffuse functions on heavy atoms; ++ adds them on hydrogens too).

❖ **Correlation-Consistent Basis Sets**

✓ Designed for post-Hartree-Fock methods (e.g., MP2, CCSD), for high-accuracy excited-state calculations, correlation-consistent basis sets .cc-pVDZ, cc-pVTZ, cc-pVQZ (D = double-zeta, T = triple-zeta, Q = quadruple-zeta).

✓ The **augmented versions** (aug-cc) include diffuse functions, making them especially suitable for optical spectra**[131,132,134]**.

c. Details of calculation:

The UV absorption and IR, Raman spectra of Au_n gold clusters (n = 2 -10) were studied using time-dependent density functional theory (TDDFT). The calculations utilize several long-term corrected xc functions, including B3LYP and CAM-B3LYP, where "CAM-B3LYP" refers to a variable with a corrected approach, the latter subject to first-principles adjustment according to the recipe of Stein et al. **[135]** By changing the range separation parameter. In the GAUSSIAN software package, TDDFT is implemented through the framework of linear response theory. This method enables the determination of a system's excited-state properties by analyzing how its electron density responds to a time-dependent perturbation. All the calculations were performed using the first-

principles wave function-based electron-correlated approaches, using the standard Hamiltonian within the Born-Oppenheimer approximation. The molecular orbitals are expressed in terms of the linear combination of Cartesian-type basis functions, also called atomic orbitals (AOs)**[131], [132], [133]**. Although for such calculations, a number of program packages are available, we employed GAUSSIAN16 for our calculations. employing a large augmented correlation-consistent polarized valence triple-ζ Def2TZVP/PP basis set. We perform excited-state calculations for various clusters employing their ground-state optimized geometries, using the configuration-interaction (CI) methodology at various levels of approximation. The CI calculations yield the vertical excitation energies, the ground and excited state wave functions, and the transition dipole matrix elements connecting the ground and the excited states, which, in turn, are used to compute the optical absorption spectra of various clusters**[127,136,137,138,139]**.

The program calculates two fundamental quantities:

- ✓ **Excitation energies**, which represent the energy required to promote electrons from occupied to unoccupied molecular orbitals.
- ✓ **Oscillator strengths**, which quantify the probability of these electronic transitions.

From these results, GAUSSIAN builds the absorption spectrum from these findings, determining the photon energies (or wavelengths) that the system can absorb. Crucially, actual photons are not used in the process. Rather, the interaction with electromagnetic radiation is simulated by applying a theoretical electric field perturbation to the electronic structure. The resulting absorption spectrum bridges theory and experiment by directly comparing with experimental UV/Vis absorption measurements and reflecting the probability of electronic transitions caused by this perturbation.

2.15. Success and Limits of Time-Dependent Density Functional Theory (TDDFT):

Despite its widespread success, both DFT and TDDFT are fundamentally constrained by the approximations made for the elusive exchange-correlation functional. The quality of these approximations directly determines the accuracy of predicted ground-state properties, and, critically, it propagates into the description of excited states in TDDFT. For challenging systems, such as transition metal complexes, strongly correlated materials, and nanoscale gold clusters, which exhibit unique plasmonic and molecular-like

optical properties that are sensitive to their size and morphology, the limitations of standard exchange-correlation functionals become particularly evident. Issues such as accurately predicting charge-transfer excitations, Rydberg states, and fundamental band gaps, as well as describing localized surface plasmon resonances, pose significant challenges to conventional DFT and TDDFT methodologies

Chapter 3

3. Electronic Properties, Structural, and Magnetic of Au_{n+2}, $TiAu_{n+1}$, and $PtTiAu_n$ clusters

3.1 Introduction

This chapter investigates the structural evolution and electronic properties of pure gold clusters (Au_n), titanium-doped clusters ($TiAu_n$), and platinum-titanium co-doped clusters ($PtTiAu_n$) for n = 1-17 atoms using Density Functional Theory calculations. Understanding how cluster geometry and composition influence electronic stability is fundamental to designing nanomaterials for biomedical applications. We systematically examine the transition from planar to three-dimensional structures, quantify stability through binding energies and second-order energy differences, and characterize electronic properties via HOMO-LUMO gaps, ionization potentials, electron affinities, and chemical hardness. The dual-doping strategy with titanium and platinum is motivated by their complementary properties: titanium enhances biocompatibility and chemical stability, while platinum improves catalytic performance and electron transfer. This comprehensive characterization establishes the foundation for understanding the optical behaviors that will be explored in Chapter 4 and provides design principles for creating application-specific nanoclusters with predetermined functional properties.

3.2 Theoretical Background of Gold Nanoclusters

3.2.1 Structural and Electronic Properties of Pure Gold Clusters

Density Functional Theory (DFT) is a widely used computational method for determining the stable geometries, electronic structures, and energetics of gold (Au) clusters.[141] Recent structural analyses have uncovered distinctive geometric patterns in small gold clusters: for Au_n (n=3−12), planar (two-dimensional) configurations are energetically preferred.[141], [142], [143] Notably, first-principles calculations indicate that the ground-state structures remain planar up to Au_6, Au_7, and Au_8, with some studies even suggesting planarity for Au_{13}.[144] Further investigations confirm that Au_{10} also exhibits a two-dimensional geometry, underscoring the persistence of low-dimensional configurations in medium-sized clusters. The stability of metal clusters, including gold nanoparticles (NPs), is influenced by their size and electronic structure.[145]

3.2.2 Stability and Magic Numbers

The stability of metal clusters, including gold nanoparticles (NPs), is influenced by their

size and electronic structure.[145]In smaller clusters (less than 1.6 nm in size), magic numbers denote specific atom counts in a cluster that are particularly stable due to complete electron shells or geometric arrangements.[146]

The spherical jellium model for three-dimensional monovalent metals offers a theoretical framework for comprehending electronic magic numbers, where stability peaks when electron shells are filled (2, 8, 18... electrons).[147]Furthermore, geometric magic numbers emerge from shell closings, leading to highly symmetric shapes like icosahedra or decahedra. These magic number configurations bolster stability for clusters of specific sizes.[148]

3.3 Motivation for Doping and Research Objectives

3.3.1 Challenges in Nanostructure Modeling

Modeling the chemical and physical properties of complex nanostructures, particularly those containing precious metals, remains a significant challenge. Researchers are actively working to refine modeling techniques to unlock the potential of these nanomaterials.[149], [150] Numerous studies have shown that introducing impurity atoms into metal clusters can significantly alter their properties.[151], [152]

3.3.2 The Role of Dual-Doping in Gold Nanoclusters

Recent research has concentrated on modifying the properties of gold (Au) clusters through doping for applications in microscopy, plasmonics, toxicology, catalysis, fluorescence, magnetism, and nanolithography. A key area of investigation is the impact of dopants on the electrical conductivity of Au clusters, which is crucial for optimizing their functional performance.[153], [154], [155] Comparative evaluations of various doping elements are limited, leaving performance comparisons largely unexplored in this and other emerging fields. [156], [157]

3.3.3 Selection of Dopants and Research Focus

We plan to select double noble gold groups saturated with platinum (Pt) and titanium (Ti), based on previous comparative studies, in order to investigate their catalytic properties, light absorption intensity, and electronic and optical stability. To our knowledge, several systematic investigations of $TiAu_n$ groups ($n \leq 18$) have been performed to date, where the incorporation of the $PtTiAu_n$ group complex may serve as a precursor to various cancer detection materials and biosensors.

In this proposed study, we aim to examine the effect of substituting one gold atom with one titanium (Ti) atom in TiAun groups. First, we intend to analyze pure gold clusters to track the evolution of their electronic, structural, and magnetic properties as a function of size and shape. Subsequently, we will extend our investigation to explore the optical properties of more complex clusters ($n \leq 7$) as an initial model to evaluate the effectiveness of these stimulants and gain a deeper understanding of their potential applications.

3.3.4 Filling the Research Gap

This research seeks to fill existing gaps by exploring the effects of dual-doping gold nanoclusters with titanium (Ti) and platinum (Pt), with a focus on their structural, electronic, magnetic, and optical properties. The addition of Ti is expected to enhance biocompatibility and chemical stability, while Pt is anticipated to improve catalytic performance and electron transfer. The resulting $PtTiAu_n$ clusters are expected to hold great potential for applications in biosensing and early cancer detection.

The study will begin with pure Au clusters, gradually replacing Au atoms with Ti and then Pt to evaluate the resulting changes. These doped clusters are projected to serve as advanced materials for diagnostics and nanotechnology applications.

3.4 Computational Details

3.4.1 DFT Implementation and Simulation Details

In our study, we utilized Density Functional Theory (DFT) by implementing Ab-Initio first-principles calculations **[158]**employing the Generalized Gradient Approximation (GGA) with the Perdew-Burke-Ernzerhof (PBE) exchange-correlation functional**[159]**This approach was combined with a mixed basis set of the effective core potential (ECP) cc-pVDZ-PP.**[160]**

The calculations were performed using the SIESTA code,**[161], [162]**which is designed to solve the Kohn-Sham Hamiltonian for isolated pseudo-atoms, taking into account the size, range, and radial shape of atomic orbitals. **[163], [164]**A double-ζ polarized (DZP) basis set was used in conjunction with norm-conserving Troullier-Martins pseudopotentials.**[165]**

The real space mesh cut-off was set to 250 Ry for the optimized pure gold cluster and increased to 400 Ry following doping. Simulations were performed in a large cubic supercell measuring 40 Å for pure clusters and 1000 Å for Ti and Pt-doped clusters, employing a face-centered cubic (fcc) model to prevent interactions between adjacent clusters. Owing to the substantial size of the supercell, Brillouin zone sampling was confined to the Γ point (k=0)

approximation.

3.4.2 Initial Structure Generation and Optimization

Various potential initial structures were assessed for each size, and, informed by prior research and literature,[166] The initial probability of the cluster structures of Au_{n+1} and mixed Au_n clusters with transition metals (Ti; Pt) was established. Furthermore, the hypothesized structures of MAu_n were derived through local relaxation following the substitution of one of the Aun atoms with the M atom in several Au_{n+1} cluster isomers, as the size of the original pure clusters increased. By substituting the M atom with an Au atom in various Au_{n+1} cluster isomers, thereby expanding the original pure clusters, the anticipated structures of MAu_n were derived through local relaxation. The diversity of MAu_n isomers stems from the varied initial placements of Au atoms within the Au_{n+1} clusters. Nevertheless, it cannot be definitively claimed that a more stable structure does not exist beyond what our calculations have identified, as the search for the lowest energy isomers does not involve a global optimization of the potential energy surface. Here, only the lowest-energy isomers for each cluster size are presented, with different initial positions of the Au atoms in the Au_{n+1} cluster leading to distinct MAu_n isomers.

3.4.3 Convergence Criteria and Analysis

Structural optimizations were conducted without imposing symmetry constraints, utilizing a conjugate gradient (CG) algorithm in conjunction with Hellman-Feynman forces.[167] The electronic structure calculations utilized self-consistent field (SCF) computations, adhering to convergence criteria of 10^{-6} a.u. for pure gold clusters and 10^{-5} a.u. for doped clusters.[168]The clusters were allowed to relax until the interatomic forces were reduced to below 10^{-2} eV/Å. Mulliken population analysis was employed to ascertain the TSMM of the optimized structures.[164]

3.4.5 Validation of Methodology

We conducted test calculations on the Au_2, Ti_2, and Pt_2 dimers to validate our DFT methodology. The results, as presented in Table 1, demonstrate good agreement with the available calculated and experimental data.

Table 2. Averaged bond length or Dimer R (Å) Au_2, Ti_2, Pt_2: Comparing the obtained result with previous theoretical and experimental data.

Dimer [R]	Our Work	Experimental values	Theoretical values
Au_2	2.564	2.47[a,b], 2.49[c]	2.488[d], 2.52[e,f], 2.53[f], 2.55[g], 2.56[h], 2.57[i]
Ti_2	2.084	1.943[j], 1.945[k], 1.97[l]	1.969[m], 1.971[n], 1.994[o], 2.059[p],2.38[a,q]
Pt_2	2.382	2.44[r], 2.40[s]	2.34[t], 2.37[v]

[a]Ref.**[168]**; [b]Ref.**[169]**; [c]Ref**[170]**; [d]Ref.**[171]**; [e]Ref**[172]**; [f]Ref.**[173]**; [g]Ref.**[174]**; [h]Ref.**[175]**; [i]Ref.**[176]** [j]Ref**[177]**; [k]Ref.**[178]**; [l]Ref.**[179]**; [m]Ref.**[180]**; [n]Ref.**[181]**; [o]Ref.**[182]** [p]Ref.**[168]**; [q]Ref.**[183]**; [r]Ref.[184]; [s]Ref.**[185]**; [t]Ref.**[186]** [v]Ref.**[187]**.

3.5 Geometries and Structural Analysis.

3.5.1 Structural Evolution Pure Gold Clusters:

Figure 1 illustrates the most stable ground states of the pure Au clusters obtained. As the size of small gold clusters increases, their structural properties are increasingly influenced by functional cross-correlation, leading to regular geometric shapes with high symmetry.

For the Au_2 dimer, multiple convergence test calculations were conducted to determine the most stable structure, which exhibits C_∞ symmetry and an average Au-Au bond length of a = 2.56(Å). This measurement closely approximates the experimental values of 2.47 (Å) and 2.49 (Å) and aligns with theoretical results reported in the literature **[181], [188]**

The pure gold cluster compounds Au_2 and Au_3 exhibit D_∞ symmetry, with bond lengths of 2.564 Å and 2.576 Å, and E_b values of 1.255 eV/atom and 1.414 eV/atom, respectively. For n = 4-9, planar two-dimensional (2D) structures were observed. The Au_4 cluster features a quaternary structure with D_{2h} symmetry, and its average bond length of 2.704 Å closely aligns with the 2.8 Å value reported in another study **[168]**

For Au_5, which displays C_{2v} symmetry, the bond length is 2.719 Å and an Eb of 2.019 eV/atom. The computational analysis employing the conjugate gradient (CG) method corroborated the planar ground-state geometries for clusters in this size range, **[168], [189]** revealing size-dependent stability patterns through variations in binding energy per atom.

3.5.1.1 Three-Dimensional Transition n= Au_{10}-Au_{17}

For pure gold particles, the most stable three-dimensional cluster structures were identified for sizes ranging from n=10 to n=17. For Au_{10}, the most favorable isomer was a compact

structure exhibiting C_2 symmetry with a bond length of 2.757 Å. Upon careful consideration of the findings and research from previous studies, it becomes evident that the results align closely with expectations. Specifically, the bond lengths for clusters ranging from Au_3 to Au_8 are approximately between 2.56Å and 2.74Å. The binding energy values for these pure clusters range from 1.24 to 2.09 eV/atom,**[155]** which is consistent with the findings of previous research. **[189]**

3.5.2 Single-Doped Gold Clusters $TiAu_n$

Gold clusters were doped with Pt and Ti atoms by substituting gold atoms in stable pure gold clusters with these elements. Figures 2 and 3 display the global structural configurations of the stabilized nanoparticles, ranging in size from 1 to 17 for Ti-1st doped clusters ($TiAu_n$).

3.5.2.1 linear $TiAu_n$ Clusters n=1-3

The $TiAu_1$ and $TiAu_2$ clusters exhibit linear configurations with C_∞ and D_∞ symmetry, respectively, possessing binding energy (E_b) values of 1.327 eV/atom and 2.091 eV/atom, and bond lengths of 2.492 Å and 2.463 Å. Upon doping, the $TiAu_3$ cluster, identified as the most stable triangular pyramid structure, exhibits D_3h symmetry and an E_b of 2.243 eV/atom. The average bond length is 2.418 Å.

3.5.2.2 Planar $TiAu_n$ Structures n=4-8

A symmetry rhombus D_2h exhibits a binding energy (E_b) of 1.839 eV/atom, which is consistent with previous research findings of 1.556 eV **[186]** and 1.487 eV.**[187]** Similarly, a two-dimensional pentahedral configuration was identified for $TiAu_4$, exhibiting C_{2v} symmetry and a bond length of 2.530 Å. This contrasts with Au_5, which also displays C_{2v} symmetry but has a bond length of 2.719 Å and an E_b of 2.019 eV/atom. The $TiAu_8$ octahedral structure, characterized by C_s symmetry and a bond length of 2.718 Å, possesses an E_b of 2.658 eV/atom, making it the most favorable structure.

The findings indicate that first-order doped clusters demonstrate enhanced structural and energetic characteristics, characterized by optimized average bond lengths and increased binding energy (E_b), which align with previous research. Regarding the initial doping with Titanium atoms, this area of research is relatively underexplored in the literature. However, the presence of two pertinent studies **[168], [190]** provides a foundational basis for further investigation.

3.5.2.3 Three-Dimensional $TiAu_n$ Clusters n=9-17

Various structures with distinct symmetries emerged following the initial doping with Ti. The optimal structural model for $TiAu_9$ was characterized by C_2 symmetry, a binding energy of 2.888 eV/atom, and an average bond length of 2.786 Å. The models for the $TiAu_{14}$ and $TiAu_{17}$ clusters, comprising 14 and 17 atoms respectively, exhibited compact structures characterized by D_2d and Cs symmetry, with Eb values of approximately 2.894 and 2.944 (eV/atom).

$TiAu_{14}$ and $TiAu_{17}$ are particularly noteworthy for their enhanced stability, which is attributed to their unique structural and electronic configurations. $TiAu_{14}$ features a highly stable, closed-cage structure centered around the Ti atom, representing a "magic number" cluster with a substantial HOMO-LUMO gap, indicative of electronic shell closure. In contrast, $TiAu_{17}$ adopts a three-dimensional form that reduces surface energy, further enhancing its remarkable stability

3.5.3 Double-Doped Gold Clusters $PtTiAu_n$

Figure 7 displays the global structural configurations of platinum-doped clusters ranging in size from 1 to 16 for Pt-2nd-doped platinum clusters $PtTiAu_n$. During the second doping phase of two-dimensional planar triangular isosceles structures, it was noted that double doping of $PtTiAu_1$ clusters with Cs symmetry led to a bond length of 2.566 Å. A two-dimensional tetrahedral model was created for $PtTiAu_4$, a ternary nanocomposite also exhibiting Cs symmetry, which showed a binding energy of Eb = 2.765 eV/atom and a bond length of 2.353 Å.

When Pt is introduced as a double dopant into the $TiAu_5$ cluster, the optimal configuration for planar states with Cs symmetry leads to the final two-dimensional pentahedral model for $PtTiAu_4$.

For $PtTiAu_n$ clusters, various initial structures with different doping atom positions were examined. Here, we present only the most stable configuration for each size. As the cluster size increases from n = 8 to n = 17, the structure evolves from 2D planar to compact 3D geometries, significantly impacting their energetic and electronic properties. Platinum atoms tend to occupy peripheral positions and, in conjunction with titanium, form near-spherical cage-like structures at larger sizes.

More detailed information on the structures of each species and different clusters can be found in Tables 3, 4, and 5. Our findings align with those of previous studies and papers **[168]**

3.5.4 Implications for Cancer Detection

Numerous studies have investigated the influence of the structural configuration of gold clusters on their efficacy in identifying cancer cells.**[191]**These clusters exhibit affinity for both

cancerous and normal cells, with the binding sites potentially facilitating charge transfer, which may affect detection methodologies.[192] By analyzing these binding sites and their impact on charge transfer, researchers can assess the hypothesis that gold clusters distinguish between cancerous and healthy cells based on their surface structure.[193]

Further research has underscored the importance of the geometric configuration of gold clusters and their effect on their potential for cancer cell detection.[199] Gold particles, particularly in cluster form, are acknowledged for their capacity to bind to cancer cells, rendering them valuable tools for cancer detection.[193]This targeting capability represents a significant advantage of gold clusters over other metal particles.[194]

The exact mechanisms by which these clusters develop into either normal or malignant cells remain incompletely understood.[194]Achieving a more thorough understanding of the structural geometry of these clusters is crucial for advancing detection methodologies that employ gold clusters.[195]

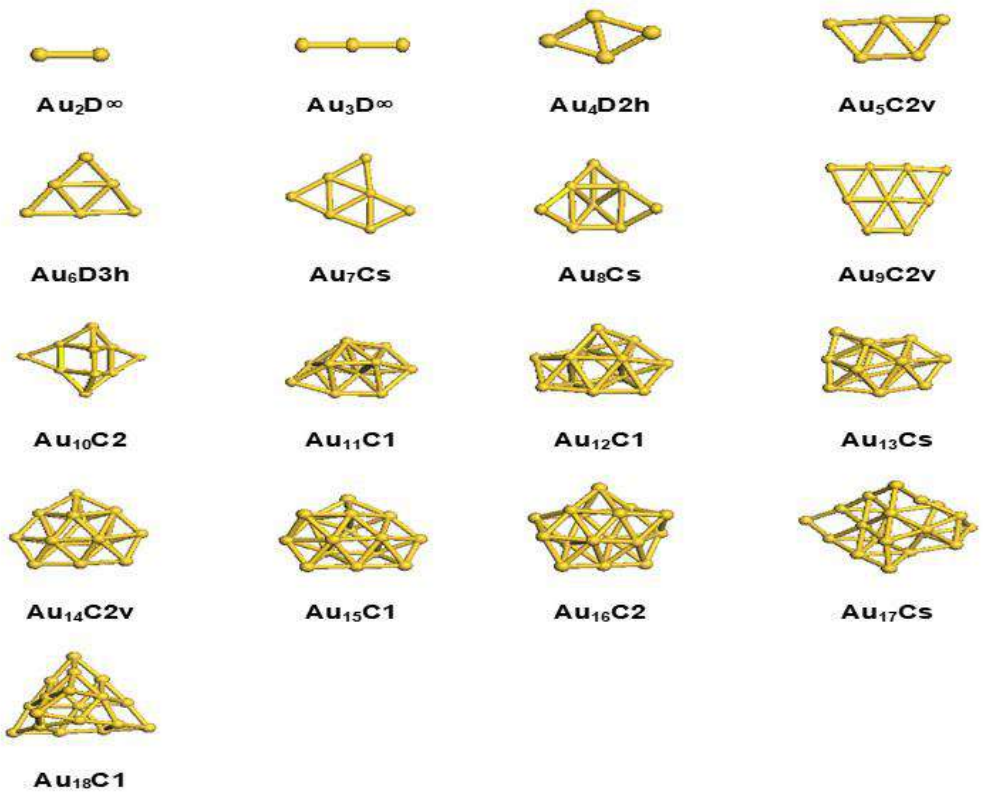

Figure 5. The most stable structures of Au_{n+2}(n = 1–17) clusters.

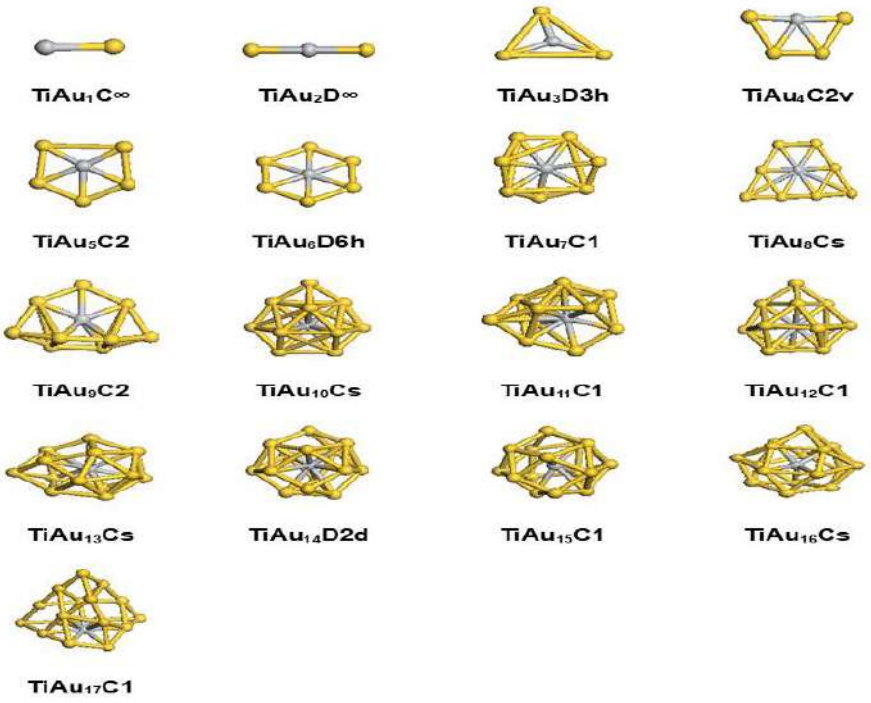

Figure 6. The most stable structures of $TiAu_{n+1}$ (n = 1–17) clusters.

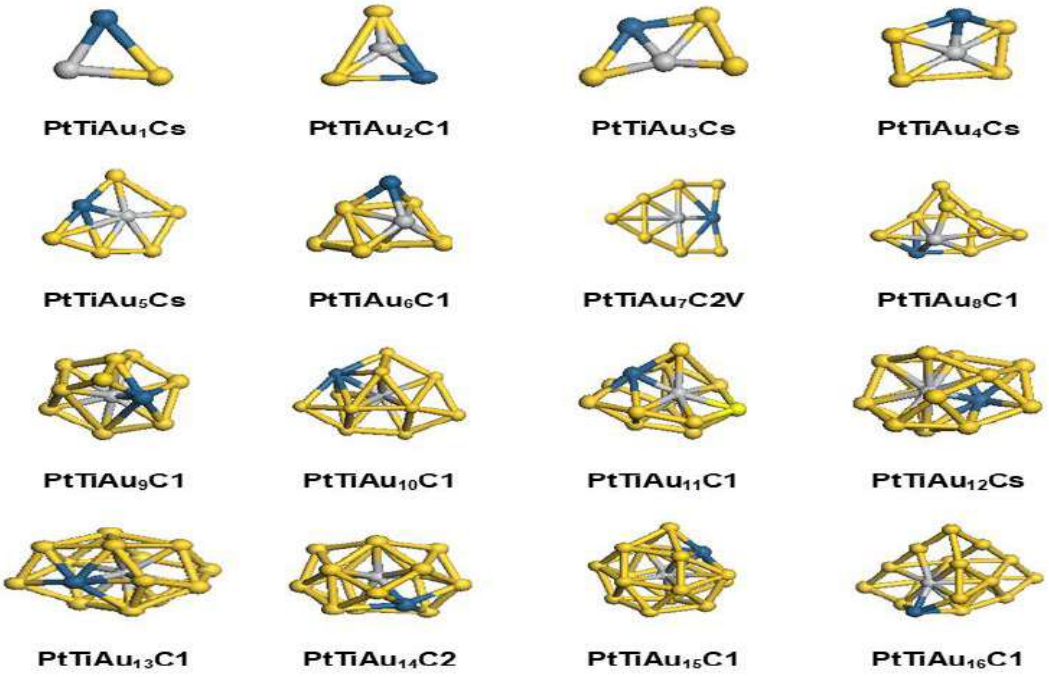

Figure 7. The most stable structures of $PtTiAu_n$ (n =1–16) clusters.

3.6 Electronic Properties

3.6.1 Binding Energies (Eb)

In the field of solid-state physics and cluster studies, the relative stability of atomic groups constitutes a critical parameter. This stability can be evaluated by examining factors such as binding energy, the second binding energy difference (Δ2E), energy gaps, Vertical Ionization Potential (VIP), and electron affinity (VEA).

3.6.1.1 Calculation Methodology

The specific binding energy Eb for each cluster was determined using the following formulas:

$$E_b\ (Au_{n+2}) = ((n+2)\ E(Au_n) - E\ (Au_{n+2}\ ))\ /\ (n+2) \quad (1)$$

$$E_b\ (TiAu_{n+1}) = ((n+1)\ E(Au) + E(Ti) - E(TiAu_{n+1}))\ /(n+2) \quad (2)$$

$$E_b\ (PtTiAu_n) = (nE\ (Au) + E(Ti) + E(Pt) - E(PtTiAu_n))\ /\ (n+2) \quad (3)$$

3.6.1.2 Size Dependence of Binding Energy

Tables 2, 3, and 4 present the calculated binding energies for all the gold clusters, while Figure 4, panels (A) and (D), illustrate the variation of these energies with cluster size. As expected, the binding energy generally increases with cluster size, indicating enhanced stability in larger clusters. This increase in stability is attributed to the average numerical density of neighboring atoms. From n = 1 to n = 6, there is a marked increase in binding energy across all systems, followed by a slower, non-linear progression.

3.6.1.2 Effects of Doping on Binding Energy

It is also observed that doped clusters exhibit significantly higher binding energies compared to pure clusters. This finding suggests that the introduction of Pt and Ti atoms generally enhances the stability of gold clusters. Double doping of gold (Au) clusters with transition metals such as titanium (Ti) and platinum (Pt) enhances their binding energies, electronic stability, and chemical reactivity, which are critical for high-performance nanomaterials used in medical detection.

Ti and Pt introduce new electronic interactions to the gold cluster, such as charge transfer and orbital hybridization, which strengthen the metal-metal bonds.**[196]**The stabilization of the

structure results in an increase in the average atomic binding energy, with minor fluctuations observed in odd-even sizes.**[197]**

3.6.1.3 Magic Number Stability

Doped clusters exhibit enhanced electronic and catalytic properties, thereby improving their sensitivity and selectivity for biomolecule detection. Their increased stability and reactivity render them ideal for application in biosensors and targeted imaging agents, facilitating rapid and accurate diagnostics. This behavior is likely attributable to the bonding characteristics of the $PtTiAu_n$ species. Notable peaks were observed in the binding energy of the MAu_n clusters at n = 5, 7, and 16, indicating that these clusters possess greater stability compared to others. The pronounced stability of the MAu_5, MAu_7, and MAu16 clusters may be attributed to their high symmetry and alignment with magic numbers.

3.6.2 Second-Order Energy Difference (Δ_2E)

3.6.2.1 Theoretical Background

In the domain of cluster solid-state physics, the second-order energy difference (Δ_2E) is acknowledged as a pivotal metric for assessing the stability and relative stability of both pure and doped clusters. Positive Δ_2E values indicate that the clusters possess substantial stability, rendering the dissociation of that atom an energetically unfavorable process.

3.6.2.2 Calculation Formulas

The calculated second-order energy differences for the Au_{n+2}, Au_{n+1}, and MAun groups are as follows:

$$\Delta_2E\,(Au_{n+2}) = E\,(Au_{n+3}) + E\,(Au_{n+1}) - 2\,E\,(Au_{n+2}) \quad (6)$$

$$\Delta_2E\,(TiAu_{n+1}) = E\,(TiAu_{n+2}) + E\,(TiAu_n) - 2\,E\,(TiAu_{n+1}) \quad (7)$$

$$\Delta_2E\,(PtTiAu_n) = E\,(PtTiAu_{n+1}) + E\,(PtTiAu_{n-1}) - 2\,E\,(PtTiAu_n) \quad (8)$$

3.6.2.3 Odd-Even Oscillations

The second-order energy difference (Δ_2E) is utilized as an indicator for evaluating the relative stability of clusters, with a larger Δ_2E value indicating a more stable cluster. Research has demonstrated that Δ_2E exhibits an odd-even pattern, which aligns with the observed pattern of

cluster abundance.[172]This suggests that clusters with an odd number of atoms tend to be more stable than those with an even number.

3.4.2.4 Stability Patterns

Δ_2E was calculated for clusters with the lowest energy configurations of Au_{n+1}, Au_{n+2}, and MAu_{n-1}, MAu_{n-2} (n =1-17; n=1-16) and is illustrated in Figure 4(B) and (E). The graphs display distinct positive peaks at (n = 1,6) for all MAu_n clusters (M = Ti, Pt). Furthermore, the diagrams indicate an increase in relative stability for $TiAu_4$, $TiAu_{14}$, and $TiAu_n$ (n = 2, 4, 8, 11, 13). The stability of the $TiAu_{14;4}$ volumes can be attributed to their alignment with the magic numbers in the traditional jellium model,[198]$PtTiAu_n$ (n = 5, 7, 8, 14), and Au_n (n = 3, 5, 9, 11, 13). This is primarily due to the interactions between the metal and gold, as the initial pure gold clusters suggest that these clusters are more stable than their adjacent counterparts.

3.6.3 HOMO-LUMO Gap Energy

The energy difference, referred to as the HOMO-LUMO gap, represents the disparity between the highest occupied molecular orbital (HOMO) and the lowest unoccupied molecular orbital (LUMO). Our results for the clusters are presented in Tables 2, 3, and 4. The findings suggest that the values of the HOMO-LUMO gap function exhibit a fluctuating pattern, with a general trend of decreasing as the cluster size increases.

Table 3. Symmetry group, Binding energy per atom Eb(eV/atom), HOMO-LUMO gap energy ΔE(eV), total spin magnetic moments μ (μB), Vertical Electronic Affinity (VEA) (eV), Vertical Ionization Potential (VIP) (eV), Chemical Hardness η (eV), and average bond distance $\alpha_{Au\text{-}Au}$ (Å) for the best isomers of Au_{n+1}(n=2-18) clusters.

cluster size[n]	symmetry	Eb[eV/atom]	ΔE [eV]	μ [μB]	VIP [eV]	VEA [eV]	η [eV]	α_{Au-Au} [Å]
Au2	D∞	1.255	1.501	0	8.208	0.091	8.299	2.564
Au3	D∞	1.414	0.167	1	7.537	1.889	5.648	2.576
Au4	D2h	1.839	1.017	0	6.706	0.408	6.298	2.704
Au5	C2v	2.019	1.326	1	6.203	1.136	5.068	2.719
Au6	D3h	2.286	1.962	0	6.798	0.193	6.605	2.714
Au7	Cs	2.261	0.824	1	5.863	1.437	4.427	2.722
Au8	Cs	2.339	1.460	0	6.013	0.391	5.622	2.775
Au9	C2v	2.399	0.149	1	6.034	1.992	4.041	2.738
Au10	C2	2.477	1.184	0	5.710	0.729	4.981	2.757
Au11	C1	2.496	0.711	1	5.142	1.158	3.985	2.824
Au12	C1	2.587	0.746	0	5.493	0.956	4.537	2.839
Au13	Cs	2.598	0.583	1	5.388	1.583	3.806	2.828
Au14	C2v	2.685	1.624	0	5.810	0.596	5.214	2.816
Au15	C1	2.683	0.705	1	4.902	1.280	3.621	2.840
Au16	C2	2.726	0.810	0	5.280	1.021	4.258	2.842
Au17	Cs	2.751	0.259	1	4.726	1.210	3.516	2.843
Au18	C1	2.794	0.825	0	5.488	1.263	4.225	2.898

Table 4. Symmetry group, Binding energy per atom E_b (eV/atom), HOMO-LUMO gap energy ΔE(eV), total spin magnetic moments μ (μB), Vertical Electronic Affinity (VEA) (eV), Vertical Ionization Potential (VIP) (eV), Chemical Hardness η (eV), and average bond distance $\alpha_{Au\text{-}Ti\ (Å)}$ for the best isomers of $TiAu_n$ (n=1-17) Clusters:

cluster size[n]	symmetry	Eb [eV/atom]	ΔE [eV]	μ [μB]	VEA [eV]	VIP [eV]	η [eV]	$\alpha_{Au\text{-}Au}$ [Å]	$\alpha_{Au\text{-}Ti}$ [Å]
TiAu1	C∞	1.327	0.320	3	-0.143	5.926	5.783	2.564	2.492
TiAu2	D∞	2.091	1.041	2	-0.118	6.885	6.767	2.576	2.463
TiAu 3	D3h	2.243	1.096	1	0.683	7.266	7.950	2.704	2.418
TiAu 4	C2v	2.360	0.800	2	0.528	6.127	6.655	2.719	2.491
TiAu 5	C2	2.466	0.887	1	0.806	5.978	6.783	2.714	2.530
TiAu6	D6h	2.548	0.318	2	1.270	5.889	7.159	2.722	2.708
TiAu 7	C1	2.567	0.996	1	1.013	5.716	6.729	2.775	2.930
TiAu 8	Cs	2.658	0.867	2	1.118	5.569	6.688	2.738	2.718
TiAu 9	C2	2.716	0.974	1	0.938	5.816	6.754	2.757	2.725
TiAu 10	Cs	2.738	0.848	2	0.607	5.316	5.923	2.824	2.970
TiAu11	C1	2.758	0.813	1	0.947	5.438	6.386	2.839	2.811
TiAu 12	C1	2.794	0.633	2	1.146	5.066	6.212	2.828	2.820
TiAu 13	Cs	2.846	0.924	1	1.073	5.448	6.521	2.816	2.731
TiAu 14	D2d	2.894	0.963	0	1.378	5.479	6.857	2.840	2.897
TiAu 15	C1	2.931	0.918	1	0.817	5.137	5.954	2.842	2.851
TiAu 16	Cs	2.944	0.634	2	0.499	4.724	5.223	2.843	2.894
TiAu17	C1	2.896	0.841	3	1.301	4.791	3.490	2.898	2.833

Table 5. Symmetry group, Binding energy per atom E_b (eV/atom), HOMO-LUMO gap energy ΔE(eV), total spin magnetic moments μ (μB), Vertical Electronic Affinity (VEA) (eV), Vertical Ionization Potential (VIP) (eV), Chemical Hardness η (eV), and average bond distance $\alpha_{AuTi-Pt}$ (Å) for the best isomers of $PtTiAu_n$ (n=1-16) Clusters:

cluster size [n]	symmetry	Eb [eV/atom]	ΔE [eV]	μ [μB]	VEA [eV]	VIP [eV]	η [eV]	α_{Au-Au} [Å]	α_{Au-Ti} [Å]	$\alpha_{AuTi-Pt}$ [Å]
PtTiAu1	Cs	2.356	0.933	3	0.796	6.055	5.260	2.564	2.492	2.566
PtTiAu2	C1	2.693	1.210	2	0.838	6.737	5.898	2.576	2.463	2.513
Pt TiAu3	Cs	2.770	1.075	1	0.704	6.619	5.915	2.704	2.418	2.630
PtTiAu4	Cs	2.765	0.868	2	1.162	6.253	5.091	2.719	2.491	2.353
PtTiAu5	Cs	2.845	0.575	1	0.877	6.346	5.470	2.714	2.530	2.804
PtTiAu6	C1	2.768	1.119	2	0.882	5.496	4.614	2.722	2.708	2.800
PtTiAu7	C2v	2.916	0.373	1	0.713	6.353	5.639	2.775	2.930	2.650
PtTiAu8	C1	2.819	0.583	2	0.788	5.324	4.536	2.738	2.718	2.794
PtTiAu9	C1	2.888	0.579	1	0.979	5.311	4.332	2.757	2.725	2.786
PtTiAu10	C1	2.914	0.340	2	1.301	5.448	4.147	2.824	2.970	2.750
PtTiAu11	C1	2.958	0.765	1	1.010	5.399	4.389	2.839	2.811	2.824
PtTiAu 12	Cs	2.998	0.739	0	0.986	5.318	4.332	2.828	2.820	2.828
PtTiAu 13	C1	3.023	0.734	1	1.074	5.781	4.707	2.816	2.731	2.840
PtTiAu 14	C2	3.057	0.933	0	1.338	5.256	3.917	2.840	2.897	2.847
PtTiAu 15	C1	3.080	1.042	1	0.786	5.209	4.423	2.842	2.851	2.829
PtTiAu16	C1	3.073	0.627	2	1.292	4.973	3.681	2.843	2.833	2.819

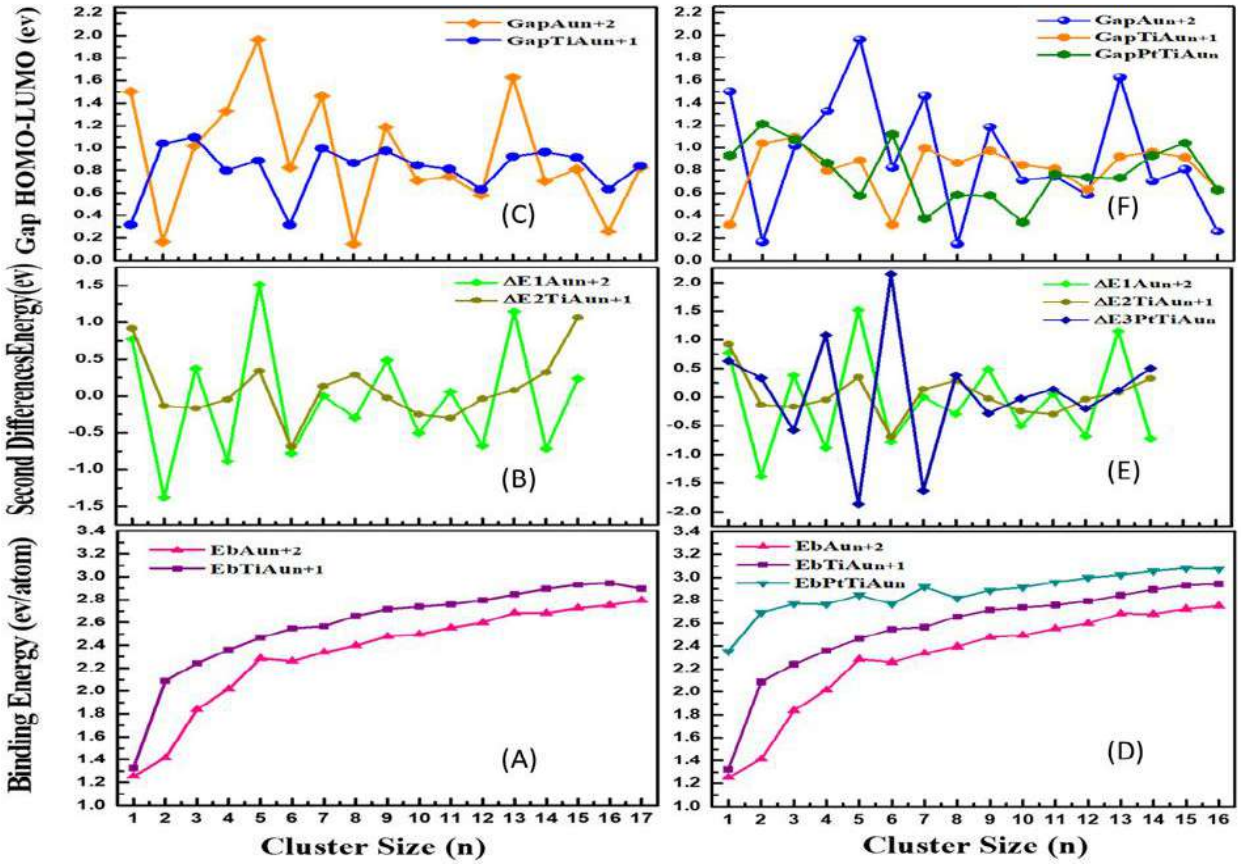

Figure 8. Size dependence of (A), (D) the binding energy, (B), (E) the second-order energy difference, and (C), (F) the HOMO–LUMO gap of Au_{n+1}; Au_{n+2} and MAu_n (MT_1 =Ti, MT_2 = Pt) clusters.

3.6.3.1 Structural and Electronic Origins

The variability in the HOMO-LUMO gap function can be ascribed to structural alterations or electron shell dynamics, particularly following the introduction of doping, and in accordance with the magic numbers that significantly influence the gap due to these electronic shell effects. When a shell is filled, the gap typically expands due to reduced electronic delocalization. Conversely, partially filled shells result in narrower gaps, leading to an oscillatory pattern as the cluster size increases.**[199,200]**

3.6.3.2 Relationship to Chemical Stability

Clusters with larger energy gaps require more energy for electron transitions and exhibit lower chemical reactivity, indicating greater chemical stability. Figure 4(C) demonstrates how

the HOMO-LUMO gaps of the most favorable isomers vary with size. The most pronounced peaks occur at n = 3,5,7,9,11,13,15, and 17, suggesting that open-shell $TiAu_{3,5,7,9,11,13,15,17}$ clusters exhibit enhanced stability.

3.6.3.3 Metallic Behavior in Even-Numbered Clusters

Conversely, the even-numbered $TiAu_{2,4,6,8,10,12,14,16}$ clusters exhibit the smallest HOMO-LUMO gaps and are closed-shell systems, thereby demonstrating metallic-like characteristics during electronic transitions. As illustrated in Figure 4(F), distinct local peaks in the HOMO-LUMO gaps are observed at n = 2, 4, 8 for $PtTiAu_{2,4,8}$ clusters, indicating that these clusters are the most stable within these systems. The $PtTiAu_{12,14}$ cluster, which possesses the smallest HOMO-LUMO gap, also exhibits metallic behavior.

3.6.3.4 Enhancement Through Dual Doping

In this discussion, we examine how the incorporation of both titanium (Ti) and platinum (Pt) atoms into gold clusters enhances their electronic stability by expanding the HOMO-LUMO energy gap. This expansion results in improved fluorescence quantum yields and more specific electrochemical signals, thereby facilitating the ultrasensitive detection of biomarkers.**[201]**Notably, the addition of Pt promotes electron delocalization, which further stabilizes the cluster, enlarges the HOMO-LUMO gap, reduces chemical reactivity, and enhances stability. In comparing and considering previous literature on the HOMO-LUMO energy gaps of pure Au and those doped with Ti, the gaps range from size n = 2-8-18, with values between 1.458 to 1.922/0.35 to 1.47 (eV).**[201]** and from $TiAu_n$ cluster. **[201]**

3.6.4 Vertical Ionization Potential (VIP) and Vertical Electron Affinity (VEA)

In this section, we examine the vertical ionization potential (VIP) and vertical electron affinity (VEA) of the system under analysis. These parameters can provide insights into the stability of atomic masses and small clusters. The calculations were performed using the following equations:

$$VIP = E^{+} - E \quad (10)$$

$$VEA = E - E^{-} \quad (11)$$

The total energy of the neutral mass is represented by E, while E^{+} and E^{-} denote the total energies of the cationic and anionic groups, respectively, all maintaining the same geometry as the neutral mass.

3.6.4.1 VIP Trends

Figure 9 and Tables 3, 4, and 5 present the values obtained for the vertical ionization potential (VIP) and vertical electron affinity (VEA) for the most stable configurations of Au_{n+2}, Au_{n+1}, and MAu_n (where M = Ti, Pt). These values indicate the energy required to add or remove an electron from neutral groups following structural relaxation. Higher VIP values suggest greater cluster stability. Figure 9(A) illustrates the VIP values for pure gold clusters, while Figure 5(E) depicts them after first-degree doping. The progression of the curve reveals a downward trend for n > 3 as the cluster size increases.

In MAu_n clusters, a fluctuating pattern was observed for sizes less than 7, followed by a decline as the cluster size increased. Notably, higher peaks were detected at n = 7 for $PtTiAu_n$ and $TiAu_n$, and at n = 3, 1, 5, 13 for pure Au_n, indicating that these specific groups exhibit greater stability compared to others.

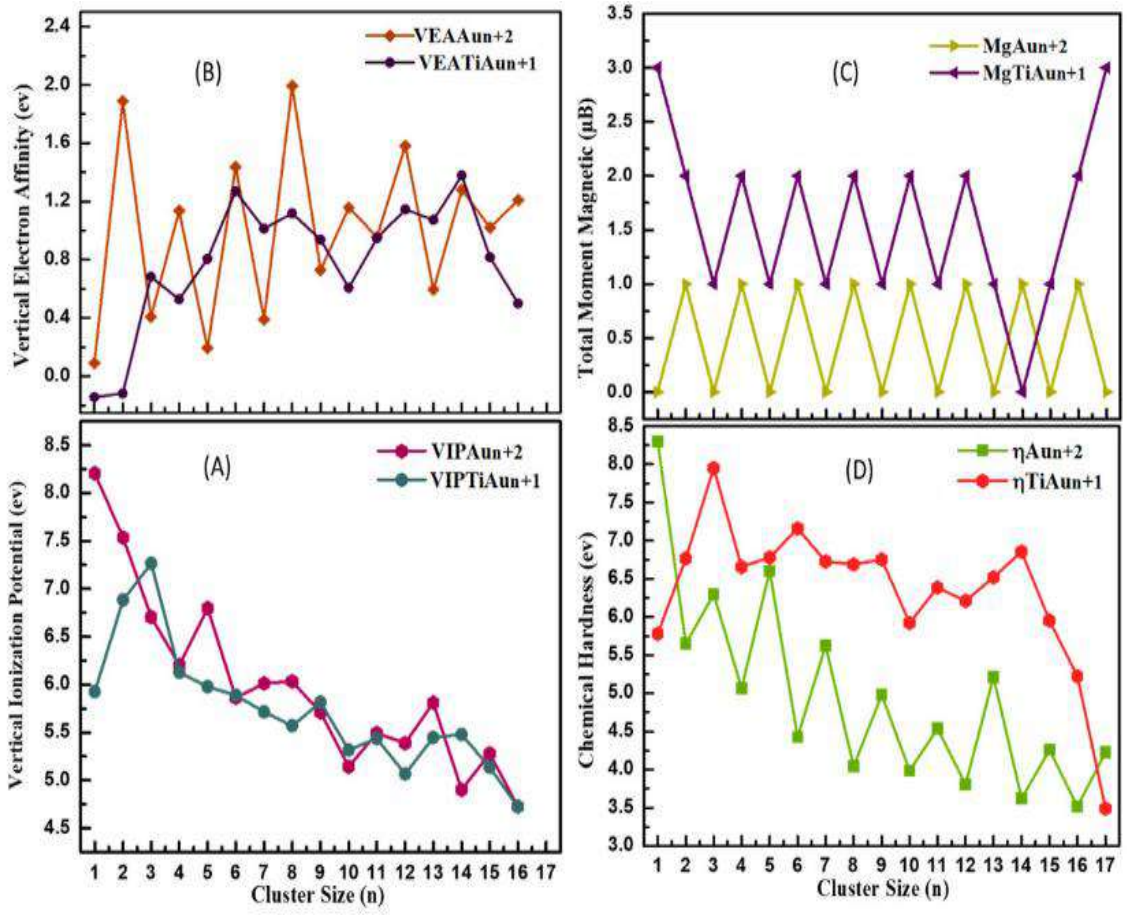

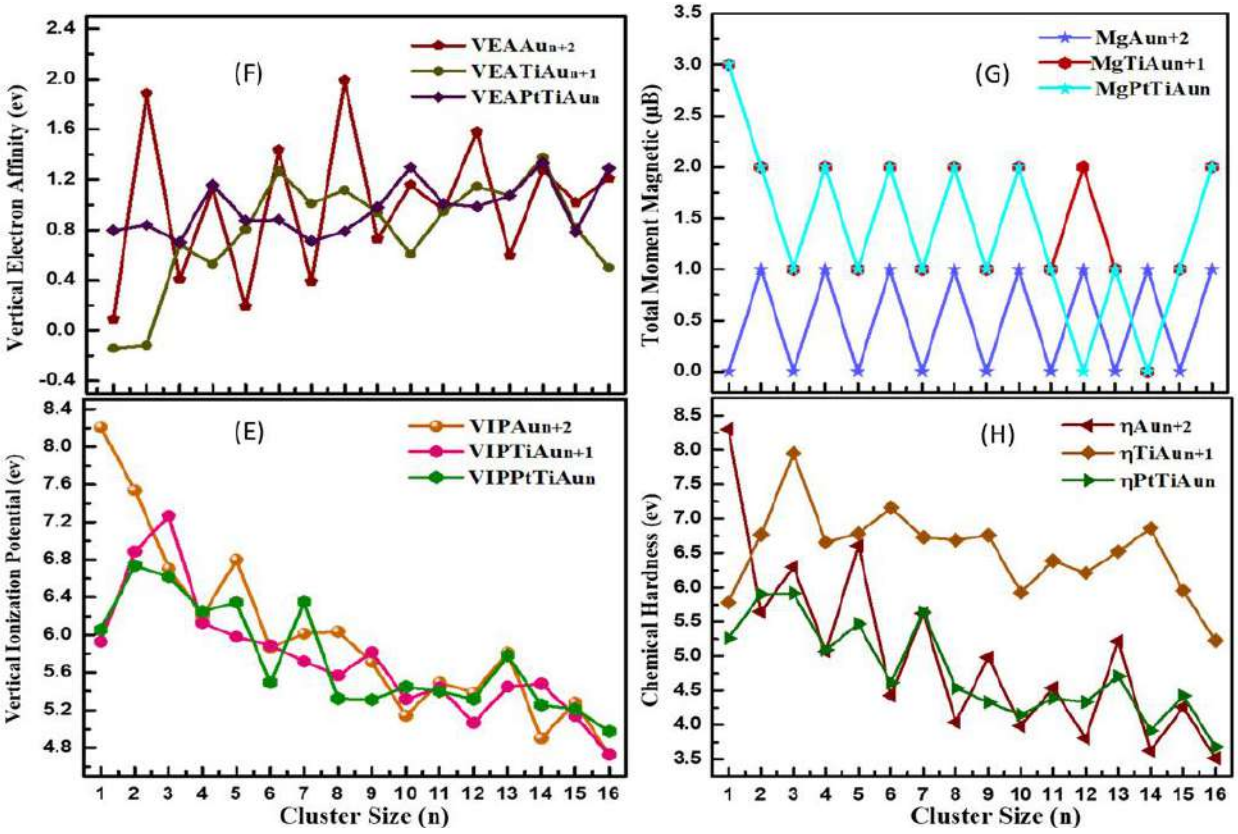

Figure 9. Size dependence of: (A),(E) vertical ionization potential, (B),(F)vertical electronic affinity, (C),(H) total spin magnetic moment and (D),(G) chemical hardness of Au_{n+1}, $Au_{n+2}$and MAu_n (MT_1= Ti, MT_2=Pt) clusters.

3.6.4.2 VEA Behavior

Electron affinity energy, denoted as VEA (refer to Figure 9), is a critical determinant of the stability of atomic clusters, as it is influenced by the cluster's size. Previous research has generally indicated that VEA tends to increase with the growth of the block size. Our study corroborated this trend, with the most pronounced peaks observed at n=14, specifically for $TiAu_{14}$ and $PtTiAu_{14}$, where VEA was measured at 1.338 eV. The VEA was calculated under the assumption that the geometry of the charged cluster was congruent with that of the neutral cluster. Typically, VEA increases with an increase in block size. Following the initial doping, VEA values were 0.143 eV for $TiAu_1$ and 0.118 eV for $TiAu_2$. A negative VEA value indicates that the electron-receiving mass is less stable than previously. Notably, VEA significantly decreased at n=1 and n=16 during the second doping for PtTiAu16 and TiAu1, as illustrated in Figure 9, (F) and (B).

3.7 Magnetic Properties

3.7.1 The Total Spin Magnetic Moment (TSMM) and PDOS:

Figure 10 presents the partial density of states (PDOS), which delineates the variation in magnetic characteristics of low-energy clusters in relation to the total spin magnetic moment (TSMM) as the cluster size n increases, as shown in Figure 9, (G) and (C). Notably, the most prominent peaks are observed for the $TiAu_{1,17}$; $PtTiAu_1$ compounds, whereas they are absent for the $TiAu_{14}$; $PtTiAu_{12,14}$ size cases.

Furthermore, we have plotted the PDOS for MT_1=Ti; MT_2=Pt, for pure Au_{n+1}; Au_{n+2}, and MAu_n groups for MT_1=Ti, (n = 1-17); MT_2 = Pt clusters, (n = 1-16), to elucidate the origin of the magnetic behavior in these various systems. The total magnetic moment value for low-energy structures is determined by the difference in total Mulliken charge populations between electrons with spin up and those with spin down.

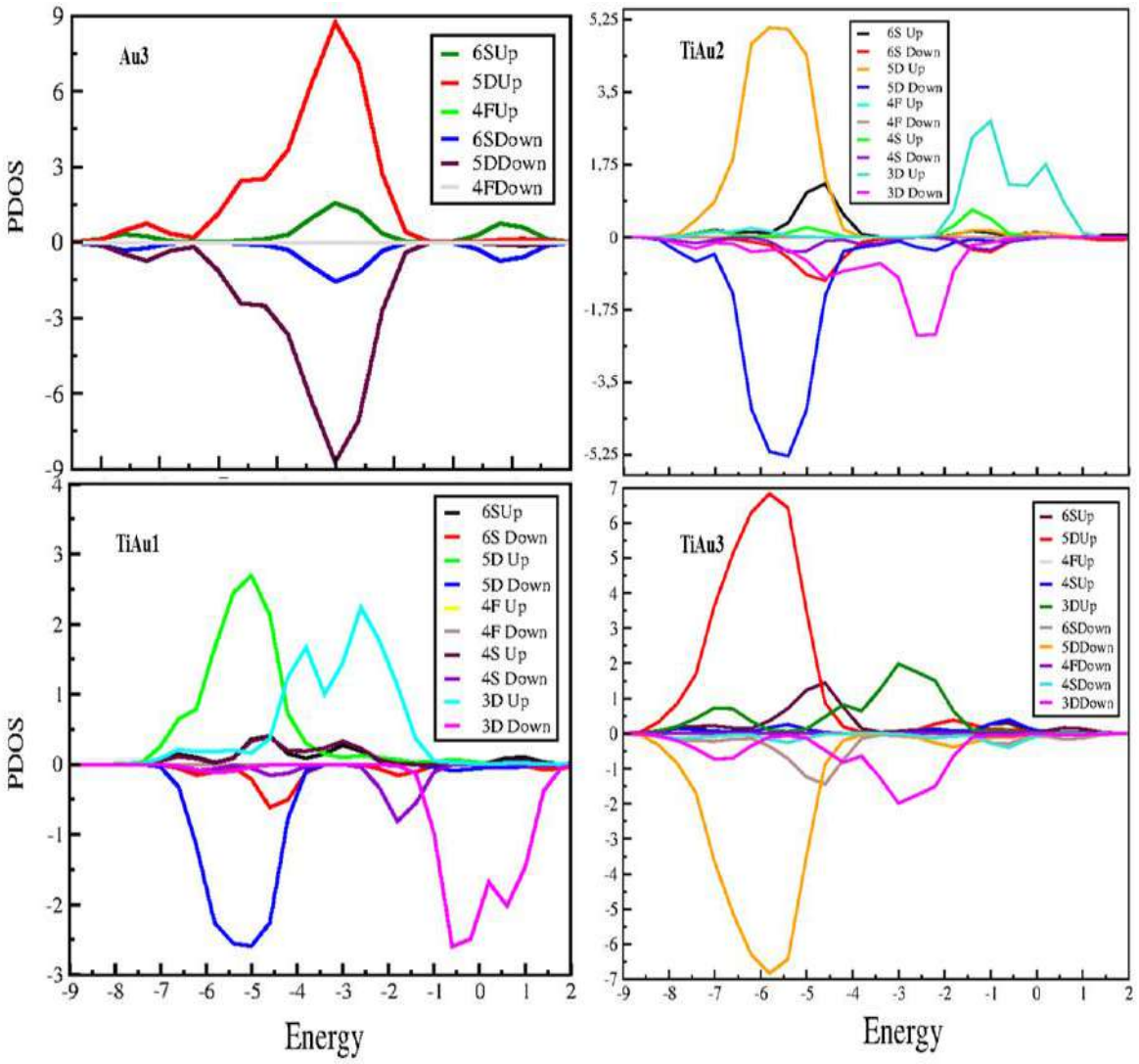

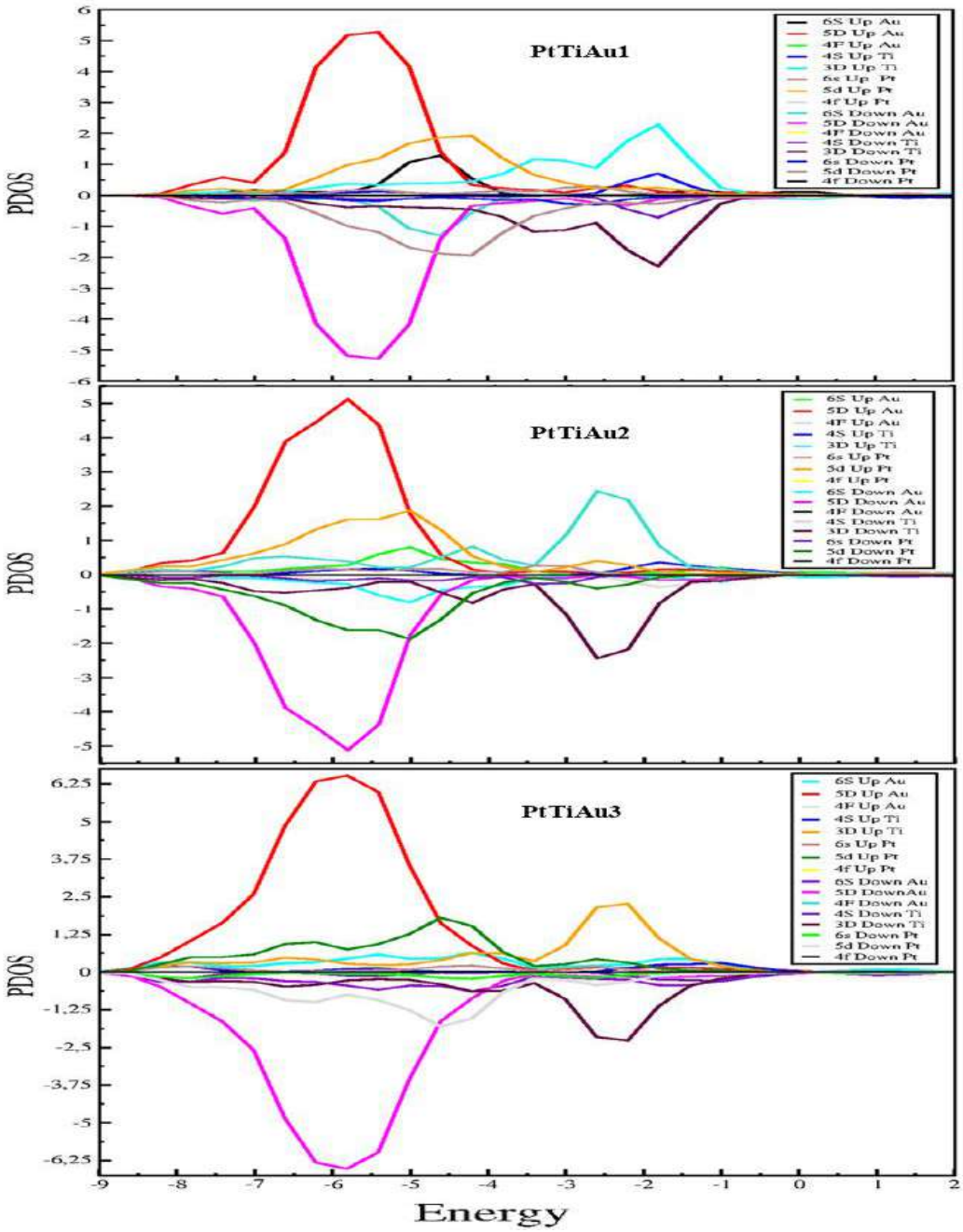

Figure 10. Partial densities of states (PDOS) for Au3, TiAu1,2,3(1st dop) than (2nd dop) PtTiAu1,2,3clusters.

3.7.2 Magnetic Behavior of Pure Gold Clusters:

3.7.2.1 Even-Numbered Clusters

The TSMM values for gold and doped gold clusters are presented in Tables 3, 4, and 5 (Chapter 3), with their size-dependent progression illustrated in Figure 9.It was observed that the TSMM for pure gold nanoclusters with even numbers is typically quenched at 0μB. Even-numbered gold clusters frequently exhibit stable, closed-shell electron configurations, where all electrons are paired, resulting in zero net spin and no overall magnetic moment.**[202]**as demonstrated by the Au_4 magnetic moment.

3.7.2.2 Odd-Numbered Clusters

In contrast, odd-sized gold clusters tend to have a magnetic moment of 1μB. For even-sized clusters, all valence electrons in the molecular orbitals are paired, whereas odd-sized clusters have one unpaired electron, leading to a net spin S=1/2 due to their electronic structure and relativistic effects. This phenomenon highlights the interaction between electron coupling, symmetry, and quantum mechanics in determining magnetic properties.

3.7.3 Magnetic Properties of Titanium-Doped Clusters

3.7.3.1 Enhanced Magnetic Moments

Upon doping with Pt and Ti atoms, the maximum total spin magnetic moment reached 3μB, observed for size n=1 in the ternary and binary compounds $PtTiAu_1$ and $TiAu_1$. For even values of n=2, 4, 6, 8, 10, 12, and 16 in the doped clusters, the total spin magnetic moment (TSMM) is 2μB for the $TiAu_n$ compounds. A significant feature of these metal clusters is the formation of closed shells, as evidenced by the even-sized systems of the studied compounds, whereas the open-shell systems correspond to the individual sizes of the jellium models.**[168]**This phenomenon has been emphasized in recent studies.**[168]**

3.7.4 Magnetic Properties of Ti-Pt doped Clusters:

3.7.4.1 Double-Doping Effects

Upon secondary doping of biomedical nanoparticles with platinum, the magnetic moments exhibit fluctuations, with the even clusters of the ternary metal compound $PtTiAu_n$ maintaining a binary magnetic moment of 2μB for n = 2, 4, 6, and 10. Notable deviations were observed in the $PtTiAu_{12}$ and $PtTiAu_{14}$ clusters, where the magnetic moments were reduced.

3.7.4.2 Odd-Sized Clusters

Additionally, odd-sized clusters (n=3,5,7,...,15) in the double doping of gold clusters display a TSMM of 1 μB, except for the initial case of size n=1, which shares the same magnetic moment as the single-doped $TiAu_1$ cluster. Furthermore, due to the high electronegativity of the titanium semiconductor atom, all chemical structures and compounds became more compact following the double doping of $PtTiAu_n$, adhering to a unique evolutionary pattern.

3.7.5 Origin of Magnetic Behavior: PDOS Analysis

a. Orbital Contributions

To elucidate the TSMM effect, we analyzed the PDOS curves depicted in Figure 6. This phenomenon is particularly evident in the smaller doped clusters at $TiAu_1$ within the 3d orbital, in contrast to the pure clusters. The effect diminishes as the cluster size increases, as observed in the $TiAu_2$ and $TiAu_3$ clusters.

b. Double-Doping Enhancement

Moreover, with double doping, the $PtTiAu_3$ cluster exhibits a more pronounced enhancement of the effect, with most centers attaining a value of 3μB in the 5d orbital. The effect decreases with increasing size, indicating an inverse relationship. However, all the PDOS curves in Figure 6 demonstrate that the total spin magnetic moment primarily originates from the 4s and 3d orbitals of the Ti atoms.

In this study, we utilized Density Functional Theory (DFT) to investigate the relative stability as well as the electronic and magnetic properties of gold clusters, specifically focusing on pure Aun, $TiAu_n$, and $PtTiAu_n$ clusters (n=1-17, n=1-16). Employing the SIESTA code, our research identified structural similarities in $PtTiAu_n$ and planar $TiAu_n$ for n=1-7, while in larger two-dimensional/three-dimensional structures, Ti atoms exhibited a tendency to position themselves in proximity to Pt (n=8-16). Various configurations with doping atoms either within or outside the cage demonstrated that titanium significantly influenced the geometries, particularly near platinum in $PtTiAu_n$ clusters. Stability was evaluated through binding energy, second-order difference energy, HOMO-LUMO gaps, ionization potential, and chemical hardness, revealing that double doping with $TiAu_1$ and $PtTiAu_1$ enhanced the magnetic moments, with 3μB observed in $TiAu_1$ and $PtTiAu_1$. Magnetic moment quenching was selectively observed in $TiAu_{14}$, $PtTiAu_{12}$, and $PtTiAu_{14}$, in contrast to the pure gold clusters of the same size. These findings elucidate the impact of

transition metals on the properties of gold clusters and provide insights into their behavior. The findings of this study enhance our comprehension of the impact of transition metal doping on gold nanoclusters, highlighting their potential in biomedical applications, particularly in cancer diagnostics. This research establishes a foundational framework for the design of nano-composites aimed at reducing fabrication costs and expediting diagnostic processes for the detection of malignant diseases. These materials are characterized by their non-toxic and biocompatible nature, as well as their exceptional catalytic and biosensing capabilities, rendering them ideal for early diagnosis through biosensors. Their applications extend to various illnesses, including cancer and renal diseases. Future investigations will focus on examining the optical absorption, fluorescence, and polarization properties of diseased cells to refine diagnostic accuracy. The results advocate for the replacement of conventional diagnostic tools, such as MRI, with safer and less physically demanding alternatives, potentially leading to more rapid and patient-friendly diagnostics. Furthermore, the high surface-area-to-volume ratio of nanoparticles enhances their efficacy in biomedical applications. Overall, these findings represent a significant advancement in the development of medical imaging and biosensing technology.

3.7.6 Chemical Hardness (η)

a) Definition and Calculation

Chemical hardness (η) is utilized as a parameter to evaluate the relative stability of clusters. A high η value indicates that the associated clusters demonstrate reduced reactivity.**[86], [203]**It is defined as follows:

$$\eta = VIP - VEA \tag{12}$$

b) Size-Dependent Trends

The chemical hardness (η) for the most stable configurations of Au_{n+2}, Au_{n+1}, and MAu_n (M = Ti, Pt) clusters is presented in Tables 2, 3, and 4, and depicted in Figure 5 in sections (D) and (H) as a function of cluster size. Figure 5 demonstrates that the chemical hardness (η) varies with cluster size, exhibiting changes influenced by their composition and structure. It was observed that as the size of the Au_{n+2}, Au_{n+1}, and MAu_n (M = Ti, Pt) clusters increased, their chemical hardness decreased, indicating a reduction in electronic stability. This suggests that larger clusters (Cluster Size > 5) are more reactive and less stable compared to smaller ones.

c) Effects of Dual Doping

As the size of gold clusters increases and they are doubly doped with Ti and Pt, their chemical hardness diminishes due to increased electron delocalization and a reduced HOMO-LUMO gap, which enhances reactivity. Ti contributes electrons while Pt stabilizes the structure, resulting in a synergistic effect that enhances the metallic nature and surface activity. Furthermore, larger clusters possess an increased number of surface atoms that are weakly bound. The introduction of doping disrupts the uniformity of bonding, thereby diminishing their overall stability and hardness **[204,205,206,207]** ,rendering these clusters particularly suitable for catalytic applications. Conversely, small clusters characterized by high hardness are ideal for applications requiring significant stability.

d) Application-Specific Implications

Incorporating titanium (Ti) and platinum (Pt) into pure gold clusters enhances their reactivity and adaptability and modifies their hardness, thereby facilitating a range of applications. $TiAu_n$ clusters generally exhibit greater chemical hardness compared to Au_n and $PtTiAu_n$ clusters, indicating superior chemical stability. This characteristic renders them suitable for medical applications that require inert and stable materials, such as biosensors and drug delivery systems. Conversely, $PtTiAu_n$ clusters, while less stable, demonstrate increased reactivity, making them advantageous for chemical catalysis and specific reactions.

3.8 Conclusion

This chapter has successfully characterized the structural and electronic properties of pure, titanium-doped, and platinum-titanium co-doped gold nanoclusters through comprehensive DFT calculations. The results demonstrate clear size-dependent transitions from planar to three-dimensional geometries, with doping accelerating this transition and enhancing cluster stability through increased binding energies. Magic number clusters at n = 5, 7, 14, and 16 exhibit exceptional stability due to electronic shell closures and favorable geometric configurations. Electronic property analysis reveals that dual doping systematically enhances binding energies, creates tunable HOMO-LUMO gaps (0.318-1.210 eV), and modifies chemical reactivity in predictable ways. The comprehensive dataset of structures, energies, and electronic descriptors provides crucial design principles for creating biomedically relevant nanoclusters. These findings establish that strategic doping enables precise control over cluster stability and electronic characteristics, positioning $PtTiAu_n$ systems as promising candidates for biosensing and cancer detection applications, explored further in Chapter 4 by optical properties.

Chapter 4

4. Optical Absorption, IR, and Raman spectra of Au_{n+2}, $TiAu_{n+1}$, and $PtTiAu_n$ clusters

4.1. Introduction

Building upon the structural and electronic foundations of Chapter 3, this chapter explores the optical properties of pure, titanium-doped, and platinum-titanium co-doped gold nanoclusters. Optical properties are investigated using time-dependent density functional theory to simulate UV-Visible absorption spectra, complemented by infrared and Raman spectroscopy calculations to characterize vibrational behaviors relevant to surface-enhanced sensing applications. The size-dependent evolution of optical absorption across the UV to near-infrared regions demonstrates how compositional control enables tuning of properties for specific biomedical functions. These optical characteristics, combined with the stability and electronic properties discussed in Chapter 3, provide a comprehensive understanding of how atomic-level design determines functional responses in multifunctional nanomaterials for cancer diagnostics and biosensing.

4.2. Optical Properties

4.2.1 Theoretical Background of Optical Properties

a. Electronic Structure and Optical Response

The optical properties of nanomaterials are intricately linked to their electronic structure, with changes in the band structure influencing the absorption and luminescence spectra. These properties, such as spectral width, peak position, and polarization sensitivity, are governed not only by intrinsic factors, such as composition, size, and shape, but also by environmental conditions (Rezaie et al., 2013).

b. Quantum Confinement Effects

As particle dimensions decrease, quantum confinement effects emerge, altering the energy level spacing and enhancing optical responses. In metallic nanoparticles, surface plasmon resonance (SPR) arising from the collective oscillations of conduction electrons under electromagnetic excitation plays a pivotal role in UV-visible absorption (Pattnaik, 2005). When particle size falls below the electron mean free path, SPR-induced absorption intensifies, enabling precise optical tuning (Homola et al., 1999)**[208]**.

c. Surface Plasmon Resonance Mechanism

The SPR effect is a resonance that occurs due to the interaction between the outer electron bands of the prepared nanoparticles and the light's wavelength. Light photons excite the outer electrons, causing the emission of particles, and consequently, the outer electrons of the metal particles vibrate at a certain wavelength and absorb light, which corresponds to that resonance. The mathematical scattering theory of both Mies and Rayleigh scattering clarifies the link between particle size and color (González et al. 2014).**[208], [209]**.

4.2.2. Computational Methodology for Optical Properties

4.2.2.1. TDDFT Framework

In this study, the UV absorption spectra of pure Au_n clusters (n = 2-6) and Ti and Pt-doped Au_n clusters were studied using time-dependent density functional theory (TDDFT). The calculations utilize several long-term corrected xc functions, including the B3LYP hybrid function and CAM-B3LYP, where "CAM-B3LYP" refers to a variable with a corrected approach, the latter subject to first-principles adjustment according to the recipe of Stein et al.**[135]**by changing the range separation parameter**[210], [211]**.

4.2.2.2. Implementation Details

In the GAUSSIAN software package, TDDFT is implemented using the linear response theory framework. This method enables the determination of a system's excited-state properties by analyzing the response of its electron density to a time-dependent perturbation. All calculations were performed using first-principles wave function-based electron-correlated approaches, using the standard Hamiltonian within the Born-Oppenheimer approximation. The molecular orbitals are expressed in terms of a linear combination of Cartesian-type basis functions, also called atomic orbitals (AOs). **[212]**

4.2.2.3. Basis Set Selection

We performed excited-state calculations for different combinations of ground-state optimized geometries of the SIESTA code, using the configuration interaction (CI) methodology **[211]**at different levels with several convergence tests to obtain the best basis set, where we chose Def2-TZVPP /Def2-TZVP basis sets of split-valence, triple-zeta containing 40-56 basis functions, which were experienced in the Linear Combination of Atomic Orbitals (LCAO) scheme.**[210], [212], [213]**

4.2.2.4. Accuracy Considerations

For accuracy and closer experimental results for excited states, Studies show that augmented basis sets (e.g., Aug-cc-pVDZ, Def2-TZVPP) yield relative errors in atomic and molecular polarizability calculations are 2.5% for augmented triple-zeta valence basis sets and yield more reliable excitation energies and absorption spectra**[213]**, especially for Rydberg and charge-transfer states, which in turn are used to calculate optical absorption spectra for different groups. We obtained the following results from the TDDFT simulation and several convergence tests.

Figures11, 12, and 13 show the spectra of small clusters of pure Au_n and their doped with Ti, Pt, and UV-Vis, and (IR/Raman vibration spectra) in **Figures 14,15,16**.

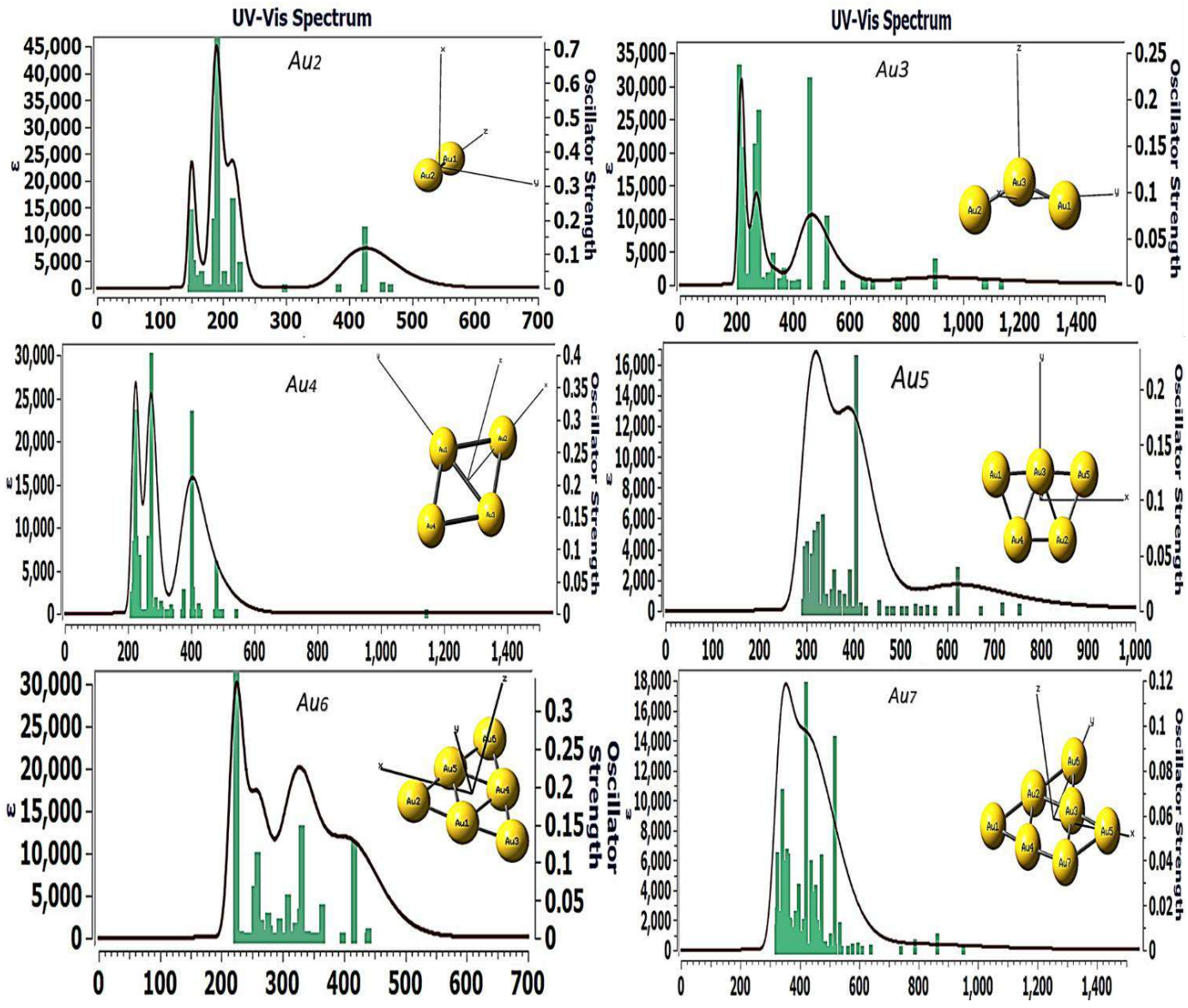

Figure 11. UV visible spectra of pure gold Cluster Au_{n+2} (n=2-7) in different excited states.

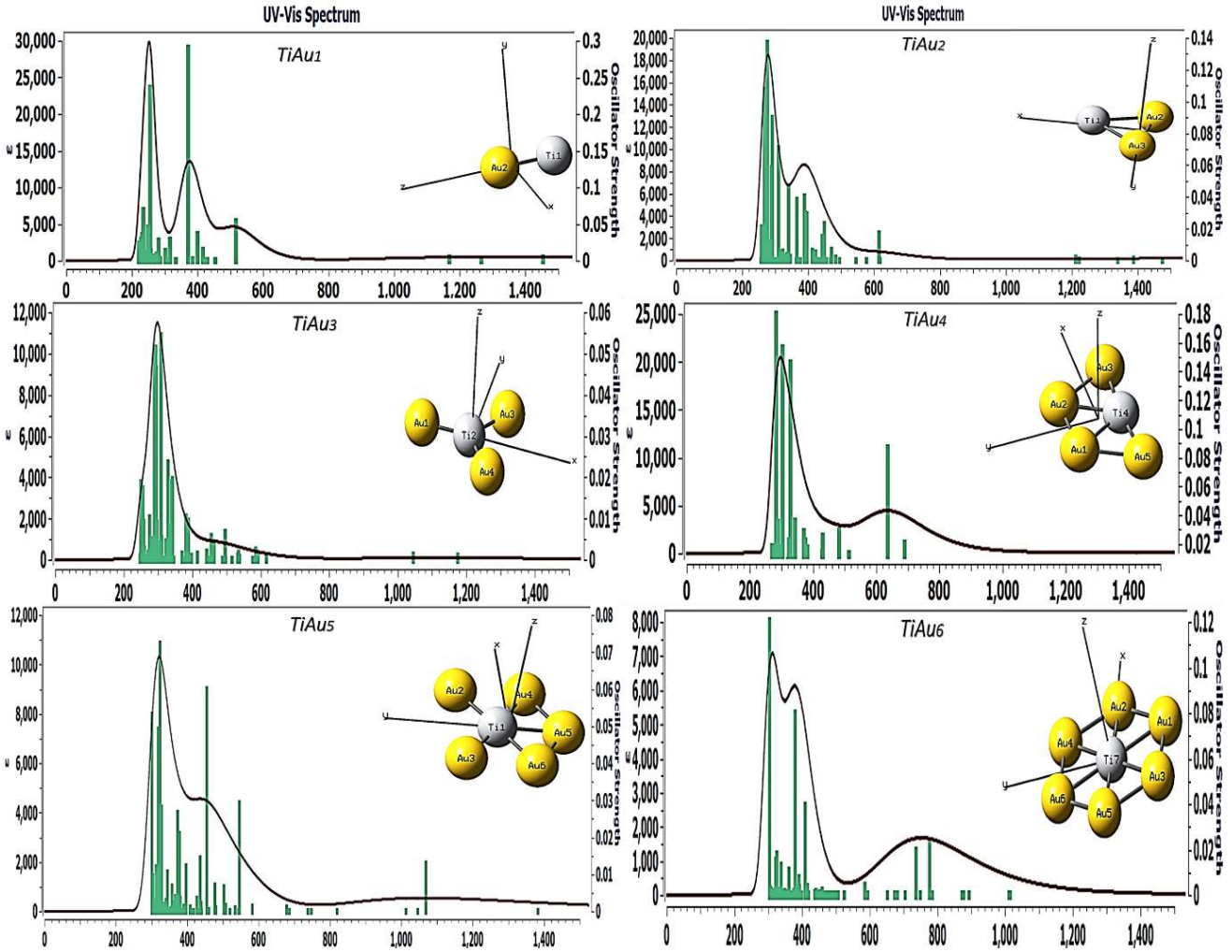

Figure 12. UV visible spectra of 1st doped gold Cluster Au_{n+1} ($TiAu_{n=1-6}$) in different

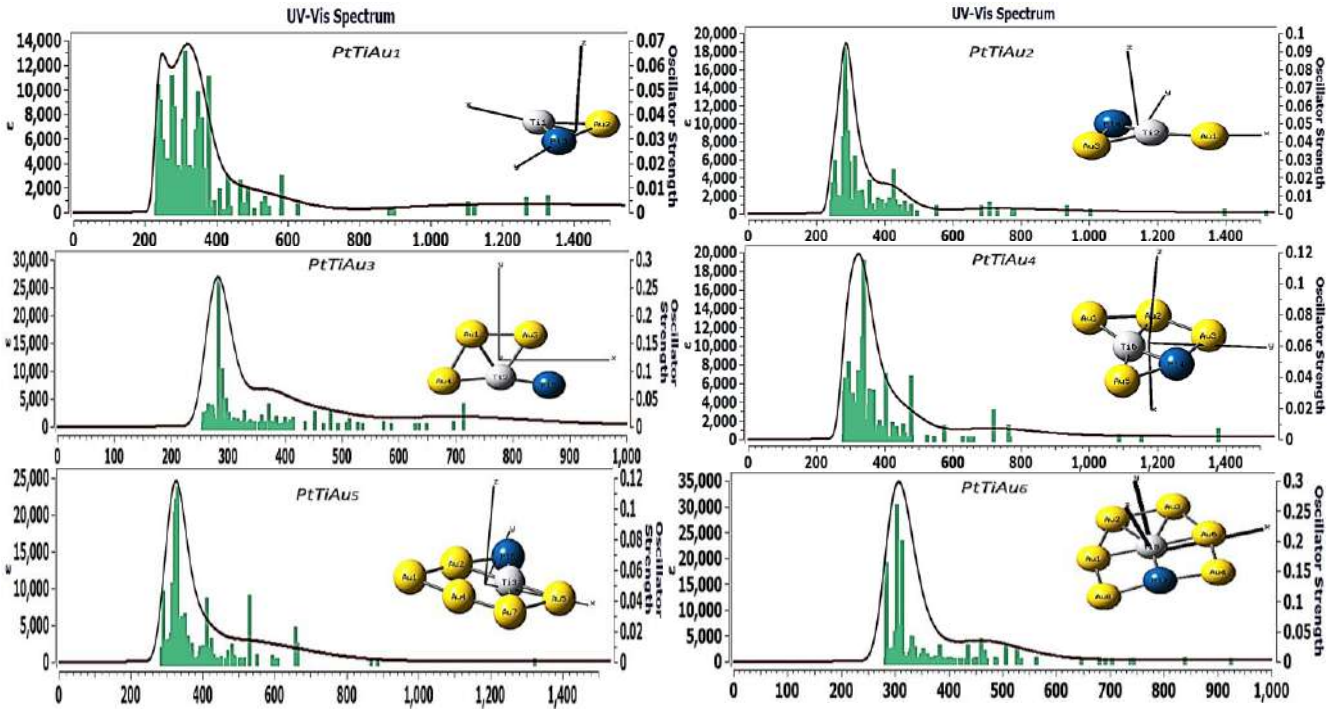

4.2.3. UV-Visible Absorption Spectra

4.2.3.1. Pure Gold Clusters Au_n n=Au_2-Au_4

The smallest clusters exhibit Au_{2-4} **Fig.11**: their strongest absorption bands are mainly in the deep UV region (less than 300 nm), indicating high-energy electron transitions (i.e., large HOMO-LUMO gaps). Double-bonded gold (Au_2) has a characteristic absorption shell with a prominent peak at a wavelength of approximately 190 nm, and a secondary maximum approximately 220 nm, accompanied by a large oscillator force extending into the visible region approximately 450 nm. This spectral signature reflects the molecular nature of the Au-Au bond, where discrete electronic transitions rather than collective plasmonic resonances dominate.

In addition, the triple configuration (Au_3) has a slight redshift of the maximum major absorption (~200-240 nm) with increasing complexity in the exact spectral structure. The appearance of multiple distinct transitions between 200-400 nm indicates an increase in the decay lifetime and symmetry-breaking effects inherent in trigonometric geometry. Au_4 (planar ring structure) presents its strongest peaks around 200-240 nm, characterized by intense absorption at wavelengths of approximately 200 and 280 nm, with a broad, structured envelope extending to 400 nm. The rhombic or planar tetrahedral geometry generates multiple semi-deteriorating excitation states, manifested by the complex vibrational progression observed in the calculated spectrum**[160], [166]**.

4.2.3.2. Emergence of Plasmonic Character n=Au_5-Au_7

As the size increased and the clusters began to adopt more compact, quasi-3D structures, the absorption extended significantly into the visible region (350-550 nm), with the initial peak redshifted. Both gold and gold exhibit a broad, intense absorption centered near 350-400 nm,**[214]** with edges extending into the visible range. This is consistent with the emerging development of the surface plasmon resonance (SPR) phenomenon, a collective oscillation of s-electrons, a hallmark of gold nanostructures**[215]**. The overall oscillator strength and spectral complexity increase with size, reflecting approximately the higher density of available excited states.

4.2.4. Effects of 1St doped $TiAu_n$ on Optical Properties

The simultaneous incorporation of Pt and Ti yields a further in **Fig. 8,9**, distinctive modulation of the optical spectra, often resulting in features characteristic of both constituent dopants. The introduction of the transition metal Ti dramatically alters the optical properties, primarily due to strong d orbital hybridization and altered electronic structure.

4.2.4.1. Red-Shift Phenomena

Titanium incorporation systematically introduces lower-energy absorption features, with $TiAu_6$ exhibiting absorption extending to (1200 nm), with the substantially red-shifted relative to Au_7. This phenomenon is derived from the energetic positioning of Titanium 3d orbitals, which introduces mid-gap states that reduce the effective optical gap.

4.2.4.2. $TiAu_n$ Clusters (n=1-3)

The $TiAu_{1-3}$ clusters showed a pronounced red shift compared to their pure Au_n counterparts:

- $TiAu_{1-2}$ has its strongest peak near 300-350 nm.
- $TiAu_{2-3}$ exhibits a dominant peak at approximately 260 nm, with a significant extension into the visible region.

This red shift signifies a reduction in the effective HOMO-LUMO gap relative to pure Au_n, likely due to the highly reactive Ti atom creating new mid-gap states through d-orbital interactions with Au s/d orbitals.

4.2.4.3. $TiAu_n$ Clusters (n=4-6)

The $TiAu_{4-6}$ clusters maintain this trend, showing complex, broad absorption spanning the UV to NIR region (up to ~1000 nm), particularly evident in $TiAu_{4-5}$.

4.2.5. Effects of 2nd Doped Clusters $PtTiAu_n$

4.2.5.1. Universal Red-Shift and Visible Activity $PtTiAu_n$ (n=1-3)

All small $PtTiAu_{1-3}$ clusters exhibited their main, strong absorption features in the UV/Visible boundary (250-350 nm), and all showed notable, albeit less intense, absorption extending into the Visible (400-600 nm):

- $PtTiAu_{1-2}$ has a dominant peak near 260 nm.

- $PtTiAu_2$ shows a main peak near 250 nm.
- $PtTiAu_3$ displays a powerful peak at 290 nm.

The consistent location of these main peaks suggests a stabilization of the electronic structure compared to that of the highly variable pure Au clusters, likely due to the strong Pt-Ti bonds dictating the core electronic framework.

4.2.5.2. Intermediate Behavior $PtTiAu_{4-6}$

While the clusters are strongly red-shifted compared to pure Au, the dominant peaks in $PtTiAu_{4–6}$ are slightly blue-shifted relative to the most visible-active $TiAu_{4–6}$ systems. This suggests that the Pt component, known for its denser d-shell, introduces stabilizing interactions that slightly increase the lowest-energy transitions. All $PtTiAu_{4–6}$ absorption extends into the NIR (up to 700 nm), indicating that the Ti-induced low-energy CT states are still present, but their oscillator strength is diminished compared to Au-based or Pt-based transitions.

4.2.5.3. Ternary System Characteristics

The ternary Pt-Ti-Au systems demonstrated intermediate behavior, with absorption characteristics positioned between pure Au_n clusters and Ti-Au_n binaries. This suggests that the electronic contribution of Platinum partially compensates for the gap-reducing effect of Titanium, yielding tunable optical properties that depend on the composition ratios. Heterometallic systems exhibit spectroscopic signatures consistent with interfacial charge transfer. The Titanium dopant, with its lower electronegativity and partially filled d-orbitals, acts as an electron donor, modifying the Fermi level and introducing occupied-to-unoccupied transitions at lower energy levels. Conversely, the higher electronegativity of Platinum induces complementary effects, creating complex charge distributions that manifest as the observed spectral patterns.

4.2.5.4. Symmetry Effects

The oscillator strength distributions revealed correlations with the cluster symmetry. Higher-symmetry configurations (e.g., D_3h, Oh) exhibit fewer, more intense transitions owing to orbital degeneracy, whereas lower-symmetry structures display complex, multi-peaked spectra reflecting symmetry-breaking effects. The calculated spectra for planar versus three-

dimensional isomers of equivalent compositions differ substantially, underscoring the critical role of geometry in determining the optical response.

4.2.6. Infrared and Raman Spectroscopy

d. Overview of Vibrational Properties

Both infrared (IR) and Raman spectroscopy provide complementary information regarding bonding properties and molecular symmetry. As shown in **Figures 14, 15, 16**, the larger the size, the more intense the IR/Raman spectra become, with new peaks emerging, as shown at size $Au_{3,4,5,6}$ in **Fig. 14**.

e. Pure Gold Clusters: Vibrational Analysis

b.1 IR/Raman Spectra of Au_3 Cluster

The Au_3 triplet exhibits remarkably sparse infrared activity, with only two important features: very weak absorption near 50 cm^{-1} and an intense dominant peak at about 165 cm^{-1} ($\varepsilon \approx 0.043$ $M^{-1}cm^{-1}$, $D(\alpha \rightarrow \sigma) \approx 0.33$ cm^{-2}). This spectral simplicity reflects the high symmetry of the more stable Au_3 geometry of an equilateral triangle with point group symmetry D_3h. The 165 cm^{-1} intense feature corresponds to the infrared active asymmetric E' expansion mode, in which two Au atoms move in a phase opposite to the third, creating a net change in dipole moment.

b.2 IR/Raman Spectra of Au_4 Cluster

Au_4 exhibits significantly enhanced vibrational complexity compared to Au_3, with prominent features at about 70 cm^{-1} ($\varepsilon \approx 17$ $M^{-1}cm^{-1}$) and dominant absorption at 155 cm^{-1} ($\varepsilon \approx 24$ $M^{-1}cm^{-1}$, $d(\alpha \rightarrow \sigma) \approx 170$ cm^{-2}). The presence of multi-active infrared modes reflects the low symmetry of the tetragonal cluster, with a rhombic geometry (D_2h).

b.3 IR/Raman Spectra of Au_5 and Au_6 Clusters

The Au_5/Au_6 cluster exhibits an infrared spectrum of 170 cm^{-1} ($\varepsilon \approx 9$ $M^{-1}cm^{-1}$, $D(\alpha \rightarrow \sigma) \approx 55$ cm^{-2}), with much weaker features distributed between 40-130 cm^{-1}. This spectral pattern indicates a highly symmetrical planar structure, while the Raman spectrum shows at least five distinguishable peaks extending from 40 to 170 cm^{-1}. The dominant peak near 90 cm^{-1} (~11

Å⁴/AMU), and the additional features at 55 cm^{-1} and 145 cm^{-1} (~9 Å⁴/AMU) reflect the increasing vibrational density of states associated with the five-atom system.

Au_6 presents a complex infrared signature with prominent absorptions at approximately 40 cm^{-1} and 90 cm^{-1}, and a dominant feature near 180 cm^{-1} ($\varepsilon \approx 30$ $M^{-1}cm^{-1}$, $D(\alpha \rightarrow \sigma) \approx 95$ cm^{-2}). The Raman activity spectrum shows unusual complexity with multiple intense peaks at approximately 70 cm^{-1} (~6 Å⁴/AMU), 105 cm^{-1} (~8 Å⁴/AMU), and a dominant peak at 145 cm^{-1} (~14 Å⁴/AMU). The maximum high-frequency Raman refers to a mode that involves significant polarization modulation, and the relationship between IR/Raman in such a peak is vice versa in all sizes, pure, and doped with Pt and Ti.

c. Single-Doped Gold Clusters $TiAu_n$: Vibrational Characteristics

1. IR/Raman Spectra of $TiAu_3$ Cluster

The incorporation of a titanium atom into pure gold clusters significantly changes the vibrational spectrum and induces IR/Raman activity in **Fig. 15** where $TiAu_3$ exhibits four main infrared active modes at approximately 30 cm^{-1}, 340 cm^{-1}, and 380 cm^{-1} (double peaks, $\varepsilon \approx$ 240 and 160 $m^{-1}cm^{-1}$ respectively, $D(\alpha \rightarrow \sigma) \approx 730$ and 500 cm^{-2}). A remarkable feature is the dramatic blue shift of the main absorption from 165 cm^{-1} in Au_3 to 340-380 cm^{-1} in $TiAu_3$.

The Raman activity spectrum exhibits intense peaks at about 110 cm^{-1} (~7 Å⁴/AMU) and 280 cm^{-1} (weak), with additional peaks at approximately 300 cm^{-1} and 350 cm^{-1} (~1 Å⁴/AMU each). The Raman intensity distribution in the intermediate frequency region confirms the presence of distinct Ti-Au vibrational modes separate from pure Au oscillations. Low frequency region (<150 cm^{-1}) contains Au-Au modes, while the high frequency region (>300 cm^{-1}) contains Ti-Au expansion modes.

2. IR/Raman Spectra of $TiAu_4$ Cluster

$TiAu_4$ represents a rich infrared spectrum with prominent absorptions at about 60 cm^{-1}, 80 cm^{-1}, 200 cm^{-1}, and a capacitor diode at 250-270 cm^{-1} ($\varepsilon \approx 125$ and 195 $m^{-1}cm^{-1}$, $D(\alpha \rightarrow \sigma)$ ≈ 130 and 195 cm^{-2}). The appearance of many well-separated peaks reflects the increasing number of atoms (5 in total) and thus the increased vibrational intensity of the states. The Raman spectrum shows exceptional intensity concentrated at approximately 110 cm^{-1} (~10 Å⁴/AMU) and 145 cm^{-1} (~8 Å⁴/AMU), indicating large changes in the collective polarizability, characteristic of breathing modes in cage-like structures.

3. IR/Raman Spectra of $TiAu_5$ and $TiAu_6$ Clusters

$TiAu_5$ presents a complex IR signature with a low-frequency shoulder near 100 cm^{-1}, mid-frequency features at 200 cm^{-1}, and an exceptionally intense high-frequency absorption at approximately 260 cm^{-1} ($\varepsilon \approx 80$ $M^{-1}cm^{-1}$, $D(\alpha \rightarrow \sigma) \approx 350$ cm^{-2}). The dominance of the 260 cm^{-1} feature suggests a particularly strong collective Ti-Au stretching mode. The Raman activity demonstrates remarkable complexity with multiple intense peaks distributed across 50-180 cm^{-1}, including prominent features at approximately 60 cm^{-1}, 90 cm^{-1}, 120 cm^{-1}, and 160 cm^{-1} (all ~3-7 $Å^4$/AMU).

The $TiAu_6$ cluster exhibits a distinctive IR pattern with features at approximately 90 cm^{-1}, 230 cm^{-1} (intense), and 260 cm^{-1} (dominant, $\varepsilon \approx 45$ $M^{-1}cm^{-1}$, $D(\alpha \rightarrow \sigma) \approx 230$ cm^{-2}). The high-frequency absorptions confirm the prevalence of Ti-Au stretching character. The Raman spectrum displays extraordinary intensity concentrated at approximately 120 cm^{-1} (~16 $Å^4$/AMU), representing one of the most intense Raman features observed for all studied clusters. Additional peaks appeared at 60 cm^{-1} and 180 cm^{-1} (~5 $Å^4$/AMU). The dominant 120 cm^{-1} mode likely corresponds to a totally symmetric breathing vibration wherein the six gold atoms oscillate radially relative to the central titanium atom.

d. Single-Doped Gold Clusters $PtTiAu_n$: Vibrational Properties

1. IR/Raman Spectra of $PtTiAu_3$ Cluster

After 2nd doping, the cluster size of $PtTiAu_3$ as shown in **Fig. 16** exhibits a remarkably complex infrared spectrum extending from 40 to 380 cm^{-1}, with prominent features at approximately 40 and 60 cm^{-1}, 85 and 225 cm^{-1}, and an intense high-frequency peak at 370 cm^{-1} ($\varepsilon \approx 67$ $M^{-1}cm^{-1}$, $d(\alpha \rightarrow \sigma) \approx 240$ cm^{-2}). This wide frequency distribution reflects the presence of three distinct metal species, each contributing to distinct vibrational signatures.

The Raman activity exhibits multiple intense features at approximately 50 cm^{-1}, 80 cm^{-1} (~2 $Å^4$/AMU), 110 cm^{-1} (~14 $Å^4$/AMU, dominant), and 185 cm^{-1} (~8 $Å^4$/AMU). The dominant peak at 110 cm^{-1} indicates a collective breathing mode involving all metal atoms, while the density distribution across multiple frequencies confirms decreased molecular symmetry. The appearance of high frequency modes (>300 cm^{-1}) indicates that Ti-Pt bonds possess strength constants that significantly exceed those of Au-Au interactions. This reflects the potential enhanced d orbital overlap between Titanium and platinum, as both have partially filled d shells, which helps form a strong covalent bond.

2. IR/Raman Spectra of $PtTiAu_4$ Cluster

$PtTiAu_4$ shows an infrared absorption at approximately 150 cm^{-1} and dominant properties near 245 cm^{-1} and 270 cm^{-1} ($\varepsilon \approx 60$ and 115 $M^{-1}cm^{-1}$ respectively, $D(\alpha \rightarrow \sigma) \approx 105$ and 115 cm^{-2}). The high-frequency region shows regulated absorption, indicating multiple Ti-Au and Pt-Au expansion modes with similar force constants but different low masses.

The Raman spectrum shows a dramatic intensity at approximately 85 cm^{-1} (~13 $Å^4$/AMU), with additional features at 65 cm^{-1}, 105 cm^{-1}, and 125 cm^{-1}. The exceptional Raman scattering cross section of the 85 cm^{-1} mode indicates a highly polarizable collective vibration, likely involving the coordinated movement of gold atoms surrounding the Pt-Ti nucleus.

e. Implications for SERS Surface-Enhanced Raman Scattering, Surface-Enhanced Raman Spectroscopy)Applications

The Raman activity spectra of the Au_n, $PtTiAu_n$, and $TiAu_n$ groups show clear peaks in the low frequency region (50-150 cm^{-1}), which are associated with vibration patterns that are efficiently coupled to plasmonic fields. Alloy groups (e.g., Pt, Ti) exhibit broader and denser Raman features, indicating increased polarizability and charge transfer, both of which enhance plasmonic coupling.

Furthermore, the infrared spectra reveal active dipole modes that do not directly contribute to SERS but provide a complementary view of vibrational symmetry and charge distribution. Spectral shifts and density adjustments observed after alloying ("doping") indicate variable electronic environments, which can adjust the LSPR frequency and field localization. This adjustability is critical for optimizing SERS substrates because the resonance state between the excitation laser and plasmonic mode determines the optimization efficiency. The enhanced Raman activity in the mixed groups reflects stronger plasmonic fields and improved SERS potential, making these nanostructures promising candidates for sensing and spectroscopic applications.

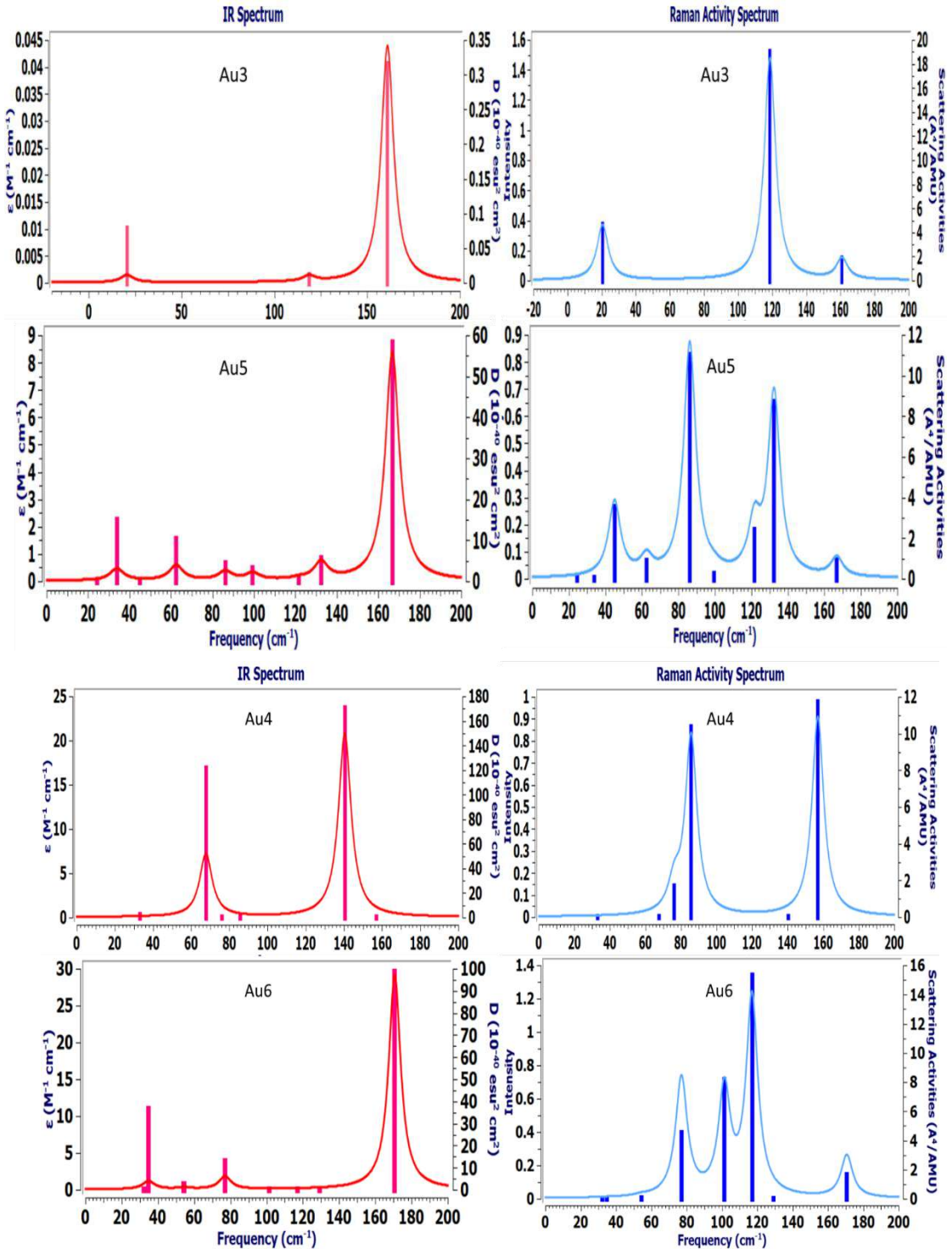

Figure 14. IR/Raman spectra of pure gold Cluster Au_{n+2} (Au_{n+2} =3-5/4-6) in different excited states.

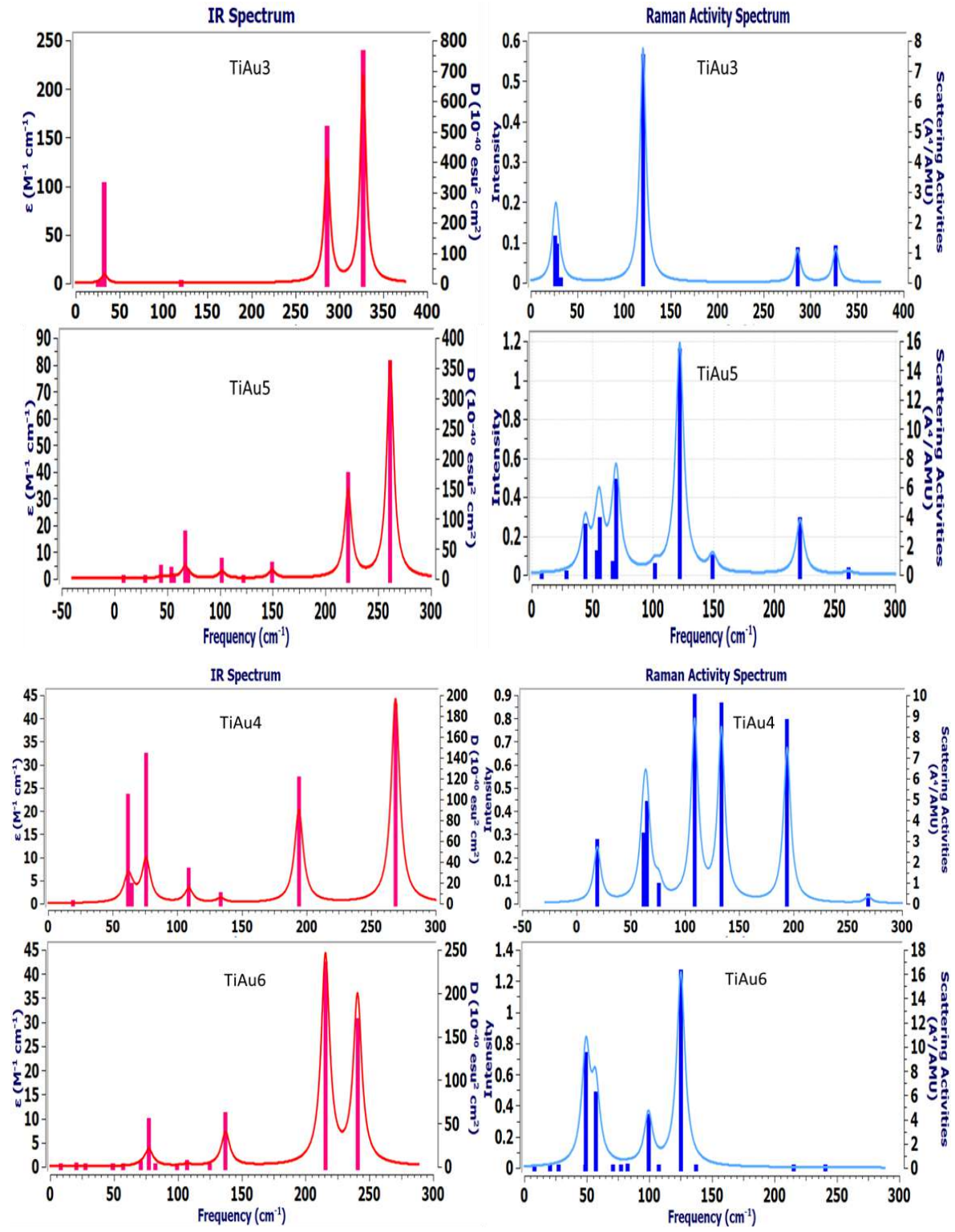

Figure 15. IR/Raman spectra of 1st doped Clusters Au_{n+1} ($TiAu_{n=3\text{-}5/4\text{-}6}$) in different excited states.

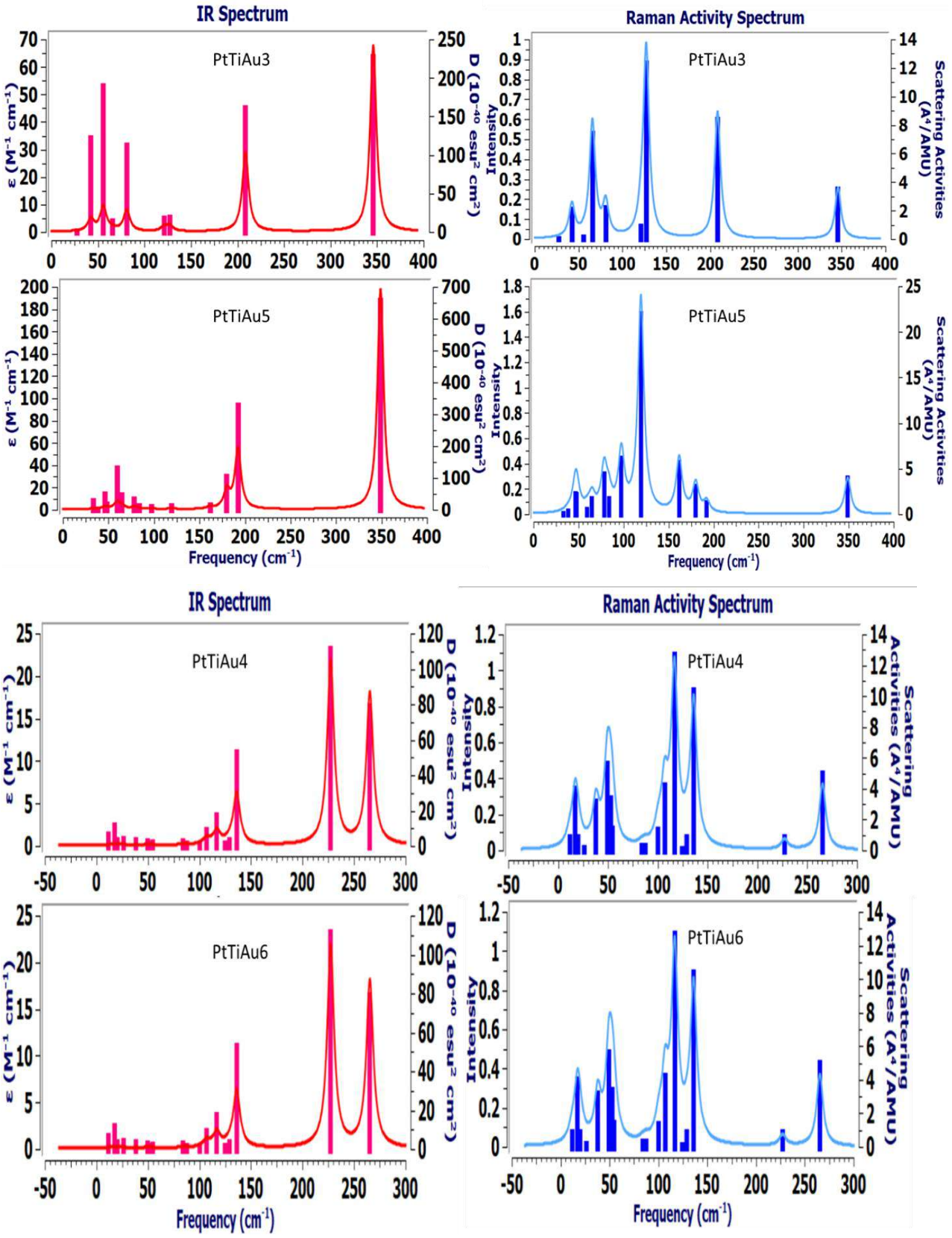

Figure 16. IR/Raman spectra of 2nd doped Clusters Aun (PtTiAun =3-5/4-6) in different excited states.

4.3. Biomedical Applications and Implications

4.3.1 Cancer Detection Potential

These findings elucidate the impact of transition metals on the properties of gold clusters and provide insights into their behavior. The findings of this study enhance our comprehension of the impact of transition metal doping on gold nanoclusters, highlighting their potential in biomedical applications, particularly in cancer diagnostics. This research establishes a foundational framework for designing nano-composites that aim to reduce fabrication costs and expedite diagnostic processes for the detection of malignant diseases.

4.3. 2 Material Characteristics for Medical Applications

These materials are characterized by their non-toxic and biocompatible nature, as well as their exceptional catalytic and biosensing capabilities, rendering them ideal for early diagnosis through biosensors. Their applications extend to various illnesses, including cancer and renal diseases. Future investigations will focus on examining the optical absorption, fluorescence, and polarization properties of diseased cells to refine diagnostic accuracy.

4.3.3 Advantages Over Conventional Diagnostics

The results advocate for the replacement of conventional diagnostic tools, such as MRI, with safer and less physically demanding alternatives, potentially leading to more rapid and patient-friendly diagnostics. Furthermore, the high surface-area-to-volume ratio of nanoparticles enhances their efficacy in biomedical applications. Overall, these findings represent a significant advancement in the development of medical imaging and biosensing technologies.

4.4. Limitations and Perspectives

Several limitations warrant discussion:

4.4.1. Theoretical Approximations

TDDFT, while powerful, has known limitations for charge-transfer excitations and Rydberg states. The use of range-separated functionals (CAM-B3LYP) partially addresses these issues, but quantitative accuracy for absolute absorption energies may be limited. Future work could employ higher-level methods such as coupled-cluster or multi-reference approaches for benchmark calculations on selected systems.

4.4.2.Environmental Effects

The calculations presented assume vacuum conditions, while real biomedical applications occur in aqueous environments with varying pH, ionic strength, and biomolecule

concentrations. Solvation effects could shift optical absorption bands, modify magnetic properties through spin-orbit coupling changes, and alter vibrational frequencies. Implementing implicit or explicit solvation models represents an important future direction.

❖ **Temperature and Dynamics**

The static calculations at 0 K do not capture finite-temperature effects such as thermal fluctuations, isomerization dynamics, or temperature-dependent magnetic behaviors. Molecular dynamics simulations incorporating nuclear motion could reveal how properties vary with temperature and whether predicted structures remain stable under physiological conditions.

❖ **Larger Size Gaps**

The computational cost limitations restricted optical property calculations to $n \leq 6$-7, while structural studies extended to n = 17. Extending optical calculations to larger sizes would reveal where the molecular-to-plasmonic transition fully occurs and whether doping continues to provide significant benefits at larger sizes approaching classical nanoparticle regimes.

❖ **Ligand Effects**

Real clusters will be stabilized by ligands (thiols, phosphines, peptides) that can significantly modify electronic structure, optical properties, and magnetic behaviors. Future studies should incorporate representative ligand shells to assess how biocompatible surface functionalization affects functional properties.

4.4.3. Synergistic Properties

An important insight emerging from this chapter is the synergistic nature of dual doping. Platinum and titanium do not simply provide additive contributions but create cooperative effects:

- Titanium introduces mid-gap states and enhances magnetism
- Platinum stabilizes the electronic structure and enhances catalytic activity
- Together, they create intermediate HOMO-LUMO gaps optimal for visible-light applications
- The combination enables magnetic targeting with preserved optical functionality
- Catalytic activity from platinum complements detection capabilities

This synergy justifies the dual-doping strategy as superior to single-dopant approaches for multifunctional biomedical applications.

4.4.4. Future Research Directions

Based on the findings of this chapter, several promising research directions emerge:

- ✓ **Experimental Validation**: Synthesize selected cluster compositions (particularly $PtTiAu_{5-8}$) and measure UV-Vis absorption, magnetic susceptibility, and Raman spectra for direct comparison with predictions.
- ✓ **Extended Size Range**: Computationally investigate larger clusters (n = 20-50) to identify where bulk-like behavior emerges and whether optimal sizes exist for specific applications.
- ✓ **Alternative Dopants**: Explore other transition metal combinations (Pd, Ag, Cu) or main group elements (Ge, Si) to broaden the palette of achievable properties.
- ✓ **Ligand Engineering**: Systematically study how different ligand types and coverages modify magnetic and optical properties, optimizing biocompatibility while preserving functionality.
- ✓ **Cellular Interactions**: Perform molecular dynamics simulations of cluster-cell membrane interactions to predict cellular uptake mechanisms, biodistribution, and potential toxicity.
- ✓ **In Vivo Modeling**: Develop pharmacokinetic models incorporating predicted properties to estimate circulation times, tumor accumulation, and clearance pathways.
- ✓ **Machine Learning Integration**: Train machine learning models on the comprehensive dataset generated to accelerate the discovery of new compositions with optimized property combinations.

4.5.Conclusion

This chapter has elucidated the optical behavior successfully demonstrated by gold nanoclusters under strategic doping. With properties spanning UV to NIR wavelengths, Titanium incorporation induces pronounced red-shifts, extending absorption from the ultraviolet range of pure gold into the near-infrared (~1200 nm for $TiAu_6$). Platinum co-doping introduces intermediate tunability, enabling fine control across the UV–NIR spectrum. Complementary vibrational analyses reveal enhanced Raman activities (up to ~16 $Å^4$/AMU in $TiAu_6$), underscoring strong SERS potential. The comprehensive characterization of these properties, combined with the structural and electronic foundations of Chapter 3, establishes a complete framework for rational design of multifunctional biomedical nanomaterials. The dual-doping synergy further integrates magnetic responsiveness with tunable optical and vibrational signatures, establishing $PtTiAu_n$ clusters as multifunctional nanostructures for biomedical applications.

General Conclusions

In conclusion to our thesis, the strategic doping of gold clusters with transition metals presents a powerful pathway for creating tailored structures, a robust first-principles computational framework for designing and characterizing doped noble metal nanoclusters. Utilizing Density Functional Theory (DFT) with the SIESTA and GAUSSIAN codes, the research precisely focused on pure Aun, TiAun, and PtTiAun clusters, quantifying the impact of Ti and Pt transition metals on the structural, electronic, magnetic, and optical stability of Au_n (n=1−17) clusters. We have demonstrated that Ti-double-doping with Pt acts as an effective electronic-structure modifier, significantly widening the HOMO-LUMO gap and tuning the magnetic moments. These findings provide a deep physical understanding of how transition metal incorporation can be leveraged to engineer nanomaterials with predefined properties."This dissertation aims to delve into these critical aspects, exploring the theoretical underpinnings of TDDFT and critically assessing the impact of underlying DFT approximations on the predicted optical properties of gold nanoclusters. TDDFT is a powerful and versatile tool for simulating the UV-Vis spectra of gold clusters and nanoparticles, with strong validation from experimental studies and ongoing methodological advances. Its ability to capture size-dependent optical transitions, ligand and doping effects, and the emergence of plasmonic behavior makes it indispensable for nanophotonics, catalysis, and biosensing applications.

However, challenges remain in accurately modeling large, complex systems, accounting for spin-orbit coupling, and selecting appropriate functionals for quantitative predictions By investigating the interplay between functional choice, relativistic effects, and the unique electronic structure of these nanoscale systems, this work seeks to advance our understanding of their light-matter interactions and contribute to the development of more robust computational strategies for predicting the optical response of complex nano systems.

References:

[1] D. Peer, J. M. Karp, S. Hong, O. C. Farokhzad, R. Margalit, and R. Langer, "Nanocarriers as an emerging platform for cancer therapy," *Nat. Nanotechnol.*, vol. 2, no. 12, pp. 751–760, 2007, doi: 10.1038/nnano.2007.387.

[2] P. Jena, "Clusters and Nanomaterials for Sustainable Energy," *ACS Energy Lett.*, vol. 5, no. 2, pp. 428–429, 2020, doi: 10.1021/acsenergylett.9b02687.

[3] N. Tian, Z.-Y. Zhou, S.-G. Sun, Y. Ding, and Z. L. Wang, "Synthesis of Tetrahexahedral Platinum Nanocrystals with High-Index Facets and High Electro-Oxidation Activity," *Science (1979).*, vol. 316, no. 5825, pp. 732–735, 2007, doi: 10.1126/science.1140484.

[4] E. C. Dreaden, A. M. Alkilany, X. Huang, C. J. Murphy, and M. A. El-Sayed, "The golden age: gold nanoparticles for biomedicine," *Chem. Soc. Rev.*, vol. 41, no. 7, pp. 2740–2779, 2012, doi: 10.1039/c1cs15237h.

[5] K. D. Gilroy, A. Ruditskiy, H.-C. Peng, D. Qin, and Y. Xia, "Bimetallic Nanocrystals: Syntheses, Properties, and Applications," *Chem. Rev.*, vol. 116, no. 18, pp. 10414–10472, 2016, doi: 10.1021/acs.chemrev.6b00211.

[6] A. P. Alivisatos, "Semiconductor Clusters, Nanocrystals, and Quantum Dots," *Science (1979).*, vol. 271, no. 5251, pp. 933–937, 1996, doi: 10.1126/science.271.5251.933.

[7] N. Kaur, R. N. Aditya, A. Singh, and T.-R. Kuo, "Biomedical Applications for Gold Nanoclusters: Recent Developments and Future Perspectives," *Nanoscale Res. Lett.*, vol. 13, no. 1, 2018, doi: 10.1186/s11671-018-2725-9.

[8] P. Pyykkö, "Theoretical Chemistry of Gold," *Angew. Chem. Int. Ed.*, vol. 43, no. 34, pp. 4412–4456, 2004, doi: 10.1002/anie.200300624.

[9] S. Vajda *et al.*, "Subnanometre platinum clusters as highly active and selective catalysts for the oxidative dehydrogenation of propane," *Nat. Mater.*, vol. 8, no. 3, pp. 213–216, 2009, doi: 10.1038/nmat2384.

[10] J. Jiang, Z. Xiong, H. Wang, K. Xiang, P. Wu, and J. Zou, "Anchoring Pt nanoparticles and Ti3C2Tx MXene nanosheets on CdS nanospheres as efficient synergistic photocatalysts for hydrogen evolution," *Sci. China Technol. Sci.*, vol. 65, no. 12, pp. 3020–3028, 2022, doi: 10.1007/s11431-022-2192-6.

[11] T. Phaahla, P. Ngoepe, and H. Chauke, "Exploring Synergistic Effect on the Stability of Ni-, Pd-, Ir-Doped TiN (N = 1–15) Nanoparticles," *Alloys*, vol. 3, no. 1, pp. 15–30, 2024, doi: 10.3390/alloys3010002.

[12] T. M. Phaahla, P. E. Ngoepe, R. A. Catlow, and H. R. Chauke, "The effect of doping with pt impurity on ti clusters: a density functional theory study," *Suid-Afrikaanse Tydskrif vir Natuurwetenskap en Tegnologie*, vol. 40, no. 1, pp. 75–78, 2022, doi: 10.36303/satnt.2021cosaami.15.

[13] Y. Chen *et al.*, "Photoemission Mechanism of Water-Soluble Silver Nanoclusters: Ligand-to-Metal–Metal Charge Transfer vs Strong Coupling between Surface Plasmon and Emitters," *J. Am. Chem. Soc.*, vol. 136, no. 5, pp. 1686–1689, 2014, doi: 10.1021/ja407911b.

[14] H. Häkkinen, "The gold–sulfur interface at the nanoscale," *Nat. Chem.*, vol. 4, no. 6, pp. 443–455, 2012, doi: 10.1038/nchem.1352.

References

[15] N. Zhang, J. Kou, and C. Sun, "Investigation on Gold–Ligand Interaction for Complexes from Gold Leaching: A DFT Study," *Molecules*, vol. 28, no. 3, 2023, doi: 10.3390/molecules28031508.

[16] "Correction to Lancet Oncol 2024; published online Dec 12. https://doi.org/10.1016/S1470-2045(24)00719-8," *Lancet Oncol.*, vol. 26, no. 1, pp. e11–e11, 2025, doi: 10.1016/s1470-2045(24)00725-3.

[17] F. Ren *et al.*, "Shortwave-infrared-light-emitting probes for the in vivo tracking of cancer vaccines and the elicited immune responses," *Nat. Biomed. Eng.*, 2023, doi: 10.1038/s41551-023-01083-5.

[18] M.-J. Lee, J.-H. Shin, S.-H. Jung, and B.-K. Oh, "Recent Advances in Biosensors Using Enzyme-Stabilized Gold Nanoclusters," *Biosensors (Basel).*, vol. 15, no. 1, p. 2, 2024, doi: 10.3390/bios15010002.

[19] Y. Zhang, S. Li, H. Liu, W. Long, and X.-D. Zhang, "Enzyme-Like Properties of Gold Clusters for Biomedical Application," *Front. Chem.*, vol. 8, 2020, doi: 10.3389/fchem.2020.00219.

[20] J. Tai, S. Fan, S. Ding, and L. Ren, "Gold Nanoparticles Based Optical Biosensors for Cancer Biomarker Proteins: A Review of the Current Practices," *Front. Bioeng. Biotechnol.*, vol. 10, 2022, doi: 10.3389/fbioe.2022.877193.

[21] A. Rajput, G. Shevalkar, K. Pardeshi, and P. Pingale, "Computational nanoscience and technology," *OpenNano*, vol. 12, p. 100147, 2023, doi: 10.1016/j.onano.2023.100147.

[22] G. D. Miteu *et al.*, "Nanoscience and technology as a pivot for sustainable agriculture and its One Health approach awareness," *Science in One Health*, vol. 2, p. 100020, 2023, doi: 10.1016/j.soh.2023.100020.

[23] M. Nasrollahzadeh, S. M. Sajadi, M. Sajjadi, and Z. Issaabadi, "An Introduction to Nanotechnology," 2019, *Elsevier*. doi: 10.1016/b978-0-12-813586-0.00001-8.

[24] V. Karanassios, "Brief introduction to nanoscience and nanotechnology," *Nanoscience Journal*, vol. 1, no. 1, pp. 1–6, 2018.

[25] "Nanomaterials and Biomedicine," 2020, *Springer Singapore*. doi: 10.1007/978-981-15-5274-8.

[26] H. Heinz *et al.*, "Nanoparticle decoration with surfactants: Molecular interactions, assembly, and applications," *Surf. Sci. Rep.*, vol. 72, no. 1, pp. 1–58, 2017, doi: 10.1016/j.surfrep.2017.02.001.

[27] S. Y. Tee, C. P. Teng, and E. Ye, "Metal nanostructures for non-enzymatic glucose sensing," *Materials Science and Engineering: C*, vol. 70, pp. 1018–1030, 2017, doi: 10.1016/j.msec.2016.04.009.

[28] E. Ye, M. D. Regulacio, S.-Y. Zhang, X. J. Loh, and M.-Y. Han, "Anisotropically branched metal nanostructures," *Chem. Soc. Rev.*, vol. 44, no. 17, pp. 6001–6017, 2015, doi: 10.1039/c5cs00213c.

[29] C. M. Welch and R. G. Compton, "The use of nanoparticles in electroanalysis: a review," *Anal. Bioanal. Chem.*, vol. 384, no. 3, pp. 601–619, 2006, doi: 10.1007/s00216-005-0230-3.

[30] C. Zhu, G. Yang, H. Li, D. Du, and Y. Lin, "Electrochemical sensors and biosensors based on nanomaterials and nanostructures," *Anal. Chem.*, vol. 87, no. 1, pp. 230–249, 2015.

[31] D. W. Kimmel, G. LeBlanc, M. E. Meschievitz, and D. E. Cliffel, "Electrochemical sensors and biosensors," *Anal. Chem.*, vol. 84, no. 2, pp. 685–707, 2012.

[32] I. Ijaz, E. Gilani, A. Nazir, and A. Bukhari, "Detail review on chemical, physical

and green synthesis, classification, characterizations and applications of nanoparticles," *Green Chem. Lett. Rev.*, vol. 13, no. 3, pp. 223–245, 2020, doi: 10.1080/17518253.2020.1802517.

[33] K. P. Chandrika, A. Singh, M. K. Tumma, and P. Yadav, "Nanotechnology prospects and constraints in agriculture," in *Environmental Nanotechnology: Volume 1*, Springer, 2018, pp. 159–186.

[34] J. K. Patel and Y. V Pathak (Editors), "Emerging Technologies for Nanoparticle Manufacturing",Springer International Publishing (2021), 611 pages, https://doi.org/10.1007/978-3-030-50703-9.

[35] N. Joudeh and D. Linke, "Nanoparticle classification, physicochemical properties, characterization, and applications: a comprehensive review for biologists," *J. Nanobiotechnology*, vol. 20, no. 1, 2022, doi: 10.1186/s12951-022-01477-8.

[36] S. Kumari and L. Sarkar, "A Review on Nanoparticles: Structure, Classification, Synthesis & Applications," *JOURNAL OF SCIENTIFIC RESEARCH*, vol. 65, no. 08, pp. 42–46, 2021, doi: 10.37398/jsr.2021.650809.

[37] Z. Liu, Z. Wu, Q. Yao, Y. Cao, O. J. H. Chai, and J. Xie, "Correlations between the fundamentals and applications of ultrasmall metal nanoclusters: Recent advances in catalysis and biomedical applications," *Nano Today*, vol. 36, p. 101053, 2021, doi: 10.1016/j.nantod.2020.101053.

[38] X.-R. Song, N. Goswami, H.-H. Yang, and J. Xie, "Functionalization of metal nanoclusters for biomedical applications," *Analyst*, vol. 141, no. 11, pp. 3126–3140, 2016, doi: 10.1039/c6an00773b.

[39] Y. Tao, M. Li, J. Ren, and X. Qu, "Metal nanoclusters: novel probes for diagnostic and therapeutic applications," *Chem. Soc. Rev.*, vol. 44, no. 23, pp. 8636–8663, 2015, doi: 10.1039/c5cs00607d.

[40] D. Chen and J. Li, "Ultrasmall Au nanoclusters for bioanalytical and biomedical applications: the undisclosed and neglected roles of ligands in determining the nanoclusters' catalytic activities," *Nanoscale Horiz.*, vol. 5, no. 10, pp. 1355–1367, 2020, doi: 10.1039/d0nh00207k.

[41] M. Chen *et al.*, "Atomically precise cu nanoclusters: recent advances, challenges, and perspectives in synthesis and catalytic applications," *Nanomicro Lett.*, vol. 17, no. 1, p. 83, 2025.

[42] R. Antoine, M. Broyer, and P. Dugourd, "Metal nanoclusters: from fundamental aspects to electronic properties and optical applications," *Sci. Technol. Adv. Mater.*, vol. 24, no. 1, 2023, doi: 10.1080/14686996.2023.2222546.

[43] I. Chakraborty and T. Pradeep, "Atomically Precise Clusters of Noble Metals: Emerging Link between Atoms and Nanoparticles," *Chem. Rev.*, vol. 117, no. 12, pp. 8208–8271, 2017, doi: 10.1021/acs.chemrev.6b00769.

[44] A. Kargar, "A DFT-Based Investigation of the properties of gold nanoclusters up to Au20," pp. 1–19, 2023.

[45] M.-C. Daniel and D. Astruc, "Gold nanoparticles: assembly, supramolecular chemistry, quantum-size-related properties, and applications toward biology, catalysis, and nanotechnology," *Chem. Rev.*, vol. 104, no. 1, pp. 293–346, 2004.

[46] H. Häkkinen, "The gold–sulfur interface at the nanoscale," *Nat. Chem.*, vol. 4, no. 6, pp. 443–455, 2012, doi: 10.1038/nchem.1352.

[47] T. Iqbal *et al.*, "A DFT study of electronic, vibrational and optical properties of gold clusters," *Opt. Quantum Electron.*, vol. 54, no. 2, 2022, doi:

10.1007/s11082-021-03446-1.

[48] Y. Wang, H. Lv, L. Sun, X. Guo, D. Xu, and B. Liu, “Ultrathin and Wavy PdB Alloy Nanowires with Controlled Surface Defects for Enhanced Ethanol Oxidation Electrocatalysis,” *ACS Applied Materials & Interfaces*, vol. 13, no. 15, pp. 17599–17607, 2021, doi: 10.1021/acsami.1c02039.

[49] R. Sun, W. Guo, X. Han, and X. Hong, “Two-dimensional Noble Metal Nanomaterials for Electrocatalysis,” *Chem. Res. Chin. Univ.*, vol. 36, no. 4, pp. 597–610, 2020, doi: 10.1007/s40242-020-0183-2.

[50] S. J. Wang, X. Y. Kuang, C. Lu, Y. F. Li, and Y. R. Zhao, “Geometries, stabilities, and electronic properties of Pt-group-doped gold clusters, their relationship to cluster size, and comparison with pure gold clusters,” *Physical Chemistry Chemical Physics*, vol. 13, no. 21, p. 10119, 2011, doi: 10.1039/c0cp02506b.

[51] M. K. Shukla, M. Dubey, E. Zakar, and J. Leszczynski, “DFT Investigation of the Interaction of Gold Nanoclusters with Nucleic Acid Base Guanine and the Watson−Crick Guanine-Cytosine Base Pair,” *The Journal of Physical Chemistry C*, vol. 113, no. 10, pp. 3960–3966, 2009, doi: 10.1021/jp808622y.

[52] L. He and T. Dong, “Multiple synthesis routes for atomically precise noble metal nanoclusters,” *CrystEngComm*, vol. 26, no. 30, pp. 3998–4016, 2024, doi: 10.1039/d4ce00488d.

[53] C. Kittel, “Introduction To Solid State Physics", 8th Edition, John Wiley & Sons, Inc. (2005), 704 pages.

[54] P. Pyykko, “Relativistic effects in structural chemistry,” *Chem. Rev.*, vol. 88, no. 3, pp. 563–594, 1988, doi: 10.1021/cr00085a006.

[55] H. Häkkinen, “Atomic and electronic structure of gold clusters: understanding flakes, cages and superatoms from simple concepts,” *Chem. Soc. Rev.*, vol. 37, no. 9, p. 1847, 2008, doi: 10.1039/b717686b.

[56] S. Link and M. A. El-Sayed, “Spectral Properties and Relaxation Dynamics of Surface Plasmon Electronic Oscillations in Gold and Silver Nanodots and Nanorods,” *J. Phys. Chem. B*, vol. 103, no. 40, pp. 8410–8426, 1999, doi: 10.1021/jp9917648.

[57] M. J. Yacamán, J. A. Ascencio, H. B. Liu, and J. Gardea-Torresdey, “Structure shape and stability of nanometric sized particles,” *Journal of Vacuum Science & Technology B: Microelectronics and Nanometer Structures Processing, Measurement, and Phenomena*, vol. 19, no. 4, pp. 1091–1103, 2001, doi: 10.1116/1.1387089.

[58] M. Walter *et al.*, “A unified view of ligand-protected gold clusters as superatom complexes,” *Proceedings of the National Academy of Sciences*, vol. 105, no. 27, pp. 9157–9162, 2008, doi: 10.1073/pnas.0801001105.

[59] R. Ferrando, J. Jellinek, and R. L. Johnston, “Nanoalloys: From Theory to Applications of Alloy Clusters and Nanoparticles,” *Chem. Rev.*, vol. 108, no. 3, pp. 845–910, 2008, doi: 10.1021/cr040090g.

[60] Y. Lu and W. Chen, “ChemInform Abstract: Metal Nanoclusters: Size-Controlled Synthesis and Size- Dependent Catalytic Activity,” *ChemInform*, vol. 46, no. 49, 2015, doi: 10.1002/chin.201549210.

[61] M. Üçüncü, “Synthesis, physicochemical characterization, and biosensing applications of gold nanoparticles,” 2018, *Izmir Institute of Technology (Turkey)*.

[62] S. Medici, M. Peana, D. Coradduzza, and M. A. Zoroddu, “Gold nanoparticles and cancer: Detection, diagnosis and therapy,” in *Seminars in cancer biology*, Elsevier, 2021, pp. 27–37.

[63] L. H. Thomas, "The calculation of atomic fields," *Mathematical Proceedings of the Cambridge Philosophical Society*, vol. 23, no. 5, pp. 542–548, 1927, doi: 10.1017/s0305004100011683.

[64] E. Fermi, "Eine statistische Methode zur Bestimmung einiger Eigenschaften des Atoms und ihre Anwendung auf die Theorie des periodischen Systems der Elemente," *Zeitschrift für Physik*, vol. 48, no. 1–2, pp. 73–79, 1928, doi: 10.1007/bf01351576.

[65] E. Schrödinger, "Über das Verhältnis der Heisenberg-Born-Jordanschen Quantenmechanik zu der meinem," *Ann. Phys.*, vol. 384, no. 8, pp. 734–756, 1926, doi: 10.1002/andp.19263840804.

[66] M. Born and R. Oppenheimer, "Zur Quantentheorie der Molekeln," *Ann. Phys.*, vol. 389, no. 20, pp. 457–484, 1927, doi: 10.1002/andp.19273892002.

[67] P. Hohenberg and W. Kohn, "Inhomogeneous Electron Gas," *Physical Review*, vol. 136, no. 3B, pp. B864–B871, 1964, doi: 10.1103/physrev.136.b864.

[68] W. Kohn and L. J. Sham, "Self-Consistent Equations Including Exchange and Correlation Effects," *Physical Review*, vol. 140, no. 4A, pp. A1133–A1138, 1965, doi: 10.1103/physrev.140.a1133.

[69] R. M. Martin, *Electronic Structure*. Cambridge University Press, 2004. doi: 10.1017/cbo9780511805769.

[70] W. Kohn and L. J. Sham, "Self-consistent equations including exchange and correlation effects," *Physical review*, vol. 140, no. 4A, p. A1133, 1965.

[71] R. van Leeuwen, *Kohn-Sham potentials in density functional theory*. Vrije Universiteit Amsterdam, The Netherlands, 1994.

[72] J. P. Perdew and Y. Wang, "Accurate and simple analytic representation of the electron-gas correlation energy," *Phys. Rev. B*, vol. 45, no. 23, pp. 13244–13249, 1992, doi: 10.1103/physrevb.45.13244.

[73] M. C. Payne, M. P. Teter, D. C. Allan, T. A. Arias, and J. D. Joannopoulos, "Iterative minimization techniques for*ab initio*total-energy calculations: molecular dynamics and conjugate gradients," *Rev. Mod. Phys.*, vol. 64, no. 4, pp. 1045–1097, 1992, doi: 10.1103/revmodphys.64.1045.

[74] D. R. Hamann, M. Schlüter, and C. Chiang, "Norm-Conserving Pseudopotentials," *Phys. Rev. Lett.*, vol. 43, no. 20, pp. 1494–1497, 1979, doi: 10.1103/physrevlett.43.1494.

[75] D. Vanderbilt, "Soft self-consistent pseudopotentials in a generalized eigenvalue formalism," *Phys. Rev. B*, vol. 41, no. 11, pp. 7892–7895, 1990, doi: 10.1103/physrevb.41.7892.

[76] S. Goedecker, M. Teter, and J. Hutter, "Separable dual-space Gaussian pseudopotentials," *Phys. Rev. B*, vol. 54, no. 3, pp. 1703–1710, 1996, doi: 10.1103/physrevb.54.1703.

[77] C. Hartwigsen, S. Goedecker, and J. Hutter, "Relativistic separable dual-space Gaussian pseudopotentials from H to Rn," *Phys. Rev. B*, vol. 58, no. 7, pp. 3641–3662, 1998, doi: 10.1103/physrevb.58.3641.

[78] D. R. Hamann, "Generalized norm-conserving pseudopotentials," *Phys. Rev. B*, vol. 40, no. 5, pp. 2980–2987, 1989, doi: 10.1103/physrevb.40.2980.

[79] N. Troullier and J. L. Martins, "Efficient pseudopotentials for plane-wave calculations," *Phys. Rev. B*, vol. 43, no. 3, pp. 1993–2006, 1991, doi: 10.1103/physrevb.43.1993.

[80] N. Richard, S. Bernard, F. Jollet, and M. Torrent, "Plane-wave pseudopotential study of the light actinides," *Phys. Rev. B*, vol. 66, no. 23, p. 235112, Dec. 2002, doi: 10.1103/PhysRevB.66.235112.

[81] J. C. Phillips and L. Kleinman, “New Method for Calculating Wave Functions in Crystals and Molecules,” *Physical Review*, vol. 116, no. 2, pp. 287–294, 1959, doi: 10.1103/physrev.116.287.

[82] J. Grotendorst, "Modern methods and algorithms of quantum chemistry: Winterschool, 21-25 February 2000, Forschungszentrum Jülich, Germany : proceedings", vol. 1. NIC Series, IV 562S, 2000.

[83] D. Vanderbilt, “Optimally smooth norm-conserving pseudopotentials,” *Phys. Rev. B*, vol. 32, no. 12, pp. 8412–8415, 1985, doi: 10.1103/physrevb.32.8412.

[84] K. F. Garrity, J. W. Bennett, K. M. Rabe, and D. Vanderbilt, “Pseudopotentials for high-throughput DFT calculations,” *Comput. Mater. Sci.*, vol. 81, pp. 446–452, 2014, doi: 10.1016/j.commatsci.2013.08.053.

[85] C. J. Cramer, *Essentials of computational chemistry: theories and models*. John Wiley & Sons, 2013.

[86] R. G. Parr, “Density functional theory of atoms and molecules,” in *Horizons of Quantum Chemistry: Proceedings of the Third International Congress of Quantum Chemistry Held at Kyoto, Japan, October 29-November 3, 1979*, Springer, 1989, pp. 5–15.

[87] V. Butera, “Density functional theory methods applied to homogeneous and heterogeneous catalysis: a short review and a practical user guide,” *Physical Chemistry Chemical Physics*, vol. 26, no. 10, pp. 7950–7970, 2024, doi: 10.1039/d4cp00266k.

[88] M. E. Casida, “Time-dependent density functional response theory for molecules,” in *Recent Advances In Density Functional Methods: (Part I)*, World Scientific, 1995, pp. 155–192.

[89] G.-T. Bae and C. M. Aikens, “Time-Dependent Density Functional Theory Studies of Optical Properties of Au Nanoparticles: Octahedra, Truncated Octahedra, and Icosahedra,” *The Journal of Physical Chemistry C*, vol. 119, no. 40, pp. 23127–23137, 2015, doi: 10.1021/acs.jpcc.5b05978.

[90] N. T. Maitra, “Perspective: Fundamental aspects of time-dependent density functional theory,” *J. Chem. Phys.*, vol. 144, no. 22, 2016, doi: 10.1063/1.4953039.

[91] E. Runge and E. K. U. Gross, “Density-Functional Theory for Time-Dependent Systems,” *Phys. Rev. Lett.*, vol. 52, no. 12, pp. 997–1000, 1984, doi: 10.1103/physrevlett.52.997.

[92] M. E. Casida and M. Huix-Rotllant, “Progress in Time-Dependent Density-Functional Theory,” *Annu. Rev. Phys. Chem.*, vol. 63, no. 1, pp. 287–323, 2012, doi: 10.1146/annurev-physchem-032511-143803.

[93] N. T. Maitra, “Charge transfer in time-dependent density functional theory,” *Journal of Physics: Condensed Matter*, vol. 29, no. 42, p. 423001, 2017, doi: 10.1088/1361-648x/aa836e.

[94] X. Zang, U. Schwingenschlögl, and M. T. Lusk, “Identification and Resolution of Unphysical Multielectron Excitations in the Real-Time Time-Dependent Kohn-Sham Formulation,” *Phys. Rev. Lett.*, vol. 124, no. 2, 2020, doi: 10.1103/physrevlett.124.026402.

[95] J. I. Fuks, M. Farzanehpour, I. V Tokatly, H. Appel, S. Kurth, and A. Rubio, “Time-dependent exchange-correlation functional for a Hubbard dimer: Quantifying nonadiabatic effects,” *Phys. Rev. A (Coll. Park).*, vol. 88, no. 6, 2013, doi: 10.1103/physreva.88.062512.

[96] H. O. Wijewardane, *Nonlinear intersubband dynamics in semiconductor nanostructures*. University of Missouri-Columbia, 2007.

[97] G. W. F. Drake, *Springer handbook of atomic, molecular, and optical physics*. Springer Nature, 2023.

[98] F. Furche and R. Ahlrichs, "Adiabatic time-dependent density functional methods for excited state properties," *J. Chem. Phys.*, vol. 117, p. 7433, Oct. 2002, doi: 10.1063/1.1508368.

[99] G. Vignale and W. Kohn, "Current-Dependent Exchange-Correlation Potential for Dynamical Linear Response Theory," *Phys. Rev. Lett.*, vol. 77, no. 10, pp. 2037–2040, 1996, doi: 10.1103/physrevlett.77.2037.

[100] X. Zang, U. Schwingenschlögl, and M. T. Lusk, "Identification and Resolution of Unphysical Multielectron Excitations in the Real-Time Time-Dependent Kohn-Sham Formulation," *Phys. Rev. Lett.*, vol. 124, no. 2, 2020, doi: 10.1103/physrevlett.124.026402.

[101] R. E. Stratmann, G. E. Scuseria, and M. J. Frisch, "An efficient implementation of time-dependent density-functional theory for the calculation of excitation energies of large molecules," *Journal of Chemical Physics*, vol. 109, no. 19, pp. 8218–8224, 1998, doi: 10.1063/1.477483.

[102] J. M. Herbert, "Density Functional Theory for Electronic Excited States", Chapter 3 in Theoretical and Computational Photochemistry, C. García-Iriepa, M. Marazzi (Editors), Elsevier (2023), pp 69-118, https://doi.org/10.1016/B978-0-323-91738-4.00005-1

[103] O. V Gritsenko and E. Jan Baerends, "Double excitation effect in non-adiabatic time-dependent density functional theory with an analytic construction of the exchange–correlation kernel in the common energy denominator approximation," *Physical Chemistry Chemical Physics*, vol. 11, no. 22, p. 4640, 2009, doi: 10.1039/b903123e.

[104] J. I. Fuks, L. Lacombe, S. E. B. Nielsen, and N. T. Maitra, "Exploring non-adiabatic approximations to the exchange–correlation functional of TDDFT," *Physical Chemistry Chemical Physics*, vol. 20, no. 41, pp. 26145–26160, 2018, doi: 10.1039/c8cp03957g.

[105] U. Aeberhard *et al.*, "Towards a Multi-scale Approach to the Simulation of Silicon Hetero-junction Solar Cells," *Journal of Green Engineering*, vol. 5, no. 4, pp. 11–32, 2016, doi: 10.13052/jge1904-4720.5342.

[106] E. Runge and E. K. U. Gross, "Density-Functional Theory for Time-Dependent Systems," *Phys. Rev. Lett.*, vol. 52, no. 12, pp. 997–1000, 1984, doi: 10.1103/physrevlett.52.997.

[107] J. P. Perdew, K. Burke, and M. Ernzerhof, "Generalized Gradient Approximation Made Simple," *Phys. Rev. Lett.*, vol. 77, no. 18, pp. 3865–3868, 1996, doi: 10.1103/physrevlett.77.3865.

[108] M. E. Casida and M. Huix-Rotllant, "Progress in Time-Dependent Density-Functional Theory," *Annu. Rev. Phys. Chem.*, vol. 63, no. 1, pp. 287–323, 2012, doi: 10.1146/annurev-physchem-032511-143803.

[109] N. T. Maitra, "Charge transfer in time-dependent density functional theory," *Journal of Physics: Condensed Matter*, vol. 29, no. 42, p. 423001, 2017, doi: 10.1088/1361-648x/aa836e.

[110] V. Butera, "Density functional theory methods applied to homogeneous and heterogeneous catalysis: a short review and a practical user guide," *Physical Chemistry Chemical Physics*, vol. 26, no. 10, pp. 7950–7970, 2024, doi: 10.1039/d4cp00266k.

[111] A. Ghosal and A. K. Roy, "A real-time TDDFT scheme for strong-field interaction in Cartesian coordinate grid", Chemical Physics Letters,

Volume 796 (2022) 139562,
https://doi.org/10.1016/j.cplett.2022.139562

[112] N. T. Maitra, "Perspective: Fundamental aspects of time-dependent density functional theory," *J. Chem. Phys.*, vol. 144, no. 22, 2016, doi: 10.1063/1.4953039.

[113] E. Artacho, J.M. Cela, J. D. Gale, A. GarcíLa, J. Junquera, R. M. Martin, P. Ordejón, D. Sánchez-Portal, and J. M. Soler, "Siesta 4.0 User's Guide" (2016), http://www.uam.es/siesta.

[114] E. Bosoni and S. Sanvito, "Complex band structure with non-orthogonal basis set: Analytical properties and implementation in the SIESTA code," *Journal of Physics Condensed Matter*, vol. 34, no. 10, 2022, doi: 10.1088/1361-648X/ac413d.

[115] J. M. Soler *et al.*, "The SIESTA method for*ab initio*order-*N*materials simulation," *Journal of Physics: Condensed Matter*, vol. 14, no. 11, pp. 2745–2779, 2002, doi: 10.1088/0953-8984/14/11/302.

[116] L. G. Verga and C. K. Skylaris, "DFT modeling of metallic nanoparticles," in *Frontiers of Nanoscience*, vol. 12, Elsevier Ltd, 2018, pp. 239–293. doi: 10.1016/B978-0-08-102232-0.00008-7.

[117] N. D. M. Hine, J. Dziedzic, P. D. Haynes, and C. K. Skylaris, "Electrostatic Interactions in Finite Systems treated with Periodic Boundary Conditions: Application to Linear-Scaling Density Functional Theory," Sep. 2011, doi: 10.1063/1.3662863.

[118] P. Rivero *et al.*, "Systematic pseudopotentials from reference eigenvalue sets for DFT calculations: Pseudopotential files," *Data Brief*, vol. 3, pp. 21–23, Jun. 2015, doi: 10.1016/j.dib.2014.12.005.

[119] N. Sharma and . S., "Density functional simulation of water molecule with Ab-initio pseudo potential," *International Journal of Advanced Academic Studies*, vol. 6, no. 6S, pp. 102–105, Jun. 2024, doi: 10.33545/27068919.2024.v6.i6b.1217.

[120] A. García *et al.*, "S iesta: Recent developments and applications," May 29, 2020, *American Institute of Physics Inc.* doi: 10.1063/5.0005077.

[121] F. Aguilera-Granja, R. H. Aguilera-del-Toro, and E. Díaz-Cervantes, "Adsorption of Selected Molecules on (TiO2)20 Nano-Clusters: A Density-Functional-Theory Study," *Nanomanufacturing*, vol. 2, no. 3, pp. 124–145, 2022, doi: 10.3390/nanomanufacturing2030010.

[122] R. Ferrando, J. Jellinek, and R. L. Johnston, "Nanoalloys: From Theory to Applications of Alloy Clusters and Nanoparticles," *Chem. Rev.*, vol. 108, no. 3, pp. 845–910, 2008, doi: 10.1021/cr040090g.

[123] C. Kittel and R. W. Hellwarth, "*Introduction to Solid State Physics*," *Phys. Today*, vol. 10, no. 6, pp. 43–44, 1957, doi: 10.1063/1.3060399.

[124] U. A. Mira-Bejaia, "République Algérienne Démocratique et Populaire Ministère de l'Enseignement Supérieur et de la Recherche Scientifique."

[125] J. B. Foresman, "Computational Chemistry: A Practical Guide for Applying Techniques to Real World Problems By David Young (Cytoclonal Pharmaceutics Inc.). Wiley-Interscience: New York. 2001. xxvi + 382 pp. $69.95. ISBN: 0-471-33368-9.," *J. Am. Chem. Soc.*, vol. 123, no. 41, pp. 10142–10143, 2001, doi: 10.1021/ja015246y.

[126] C. Kittel and R. W. Hellwarth, "*Introduction to Solid State Physics*," *Phys. Today*, vol. 10, no. 6, pp. 43–44, 1957, doi: 10.1063/1.3060399.

[127] J. S. Binkley *et al.*, "GAUSSIAN 76: an ab initio molecular orbital program,"

Office of Scientific and Technical Information (OSTI), 1978. doi: 10.2172/6738000.

[128] M. J. S. Dewar and D. M. Storch, "Development and use of quantum molecular models. 75. Comparative tests of theoretical procedures for studying chemical reactions," *J. Am. Chem. Soc.*, vol. 107, no. 13, pp. 3898–3902, 1985, doi: 10.1021/ja00299a023.

[129] K. Mishra, C. Stanghellini, and S. Hemming, "Technology and Materials for Passive Manipulation of the Solar Spectrum in Greenhouses," *Adv. Sustain. Syst.*, vol. 7, p., 2023, doi: 10.1002/adsu.202200503.

[130] R. Ferrando, J. Jellinek, and R. L. Johnston, "Nanoalloys: From Theory to Applications of Alloy Clusters and Nanoparticles," *Chem. Rev.*, vol. 108, no. 3, pp. 845–910, 2008, doi: 10.1021/cr040090g.

[131] B. Nagy and F. Jensen, "Basis Sets in Quantum Chemistry," pp. 93–149, 2017, doi: 10.1002/9781119356059.CH3.

[132] J. G. Hill, "Gaussian basis sets for molecular applications," Jan. 05, 2013. doi: 10.1002/qua.24355.

[133] C. Morassut, E. Coccia, and E. Luppi, "Quantitative performance analysis and comparison of optimal-continuum Gaussian basis sets for high-harmonic generation spectra.," *J. Chem. Phys.*, vol. 159 12, p., 2023, doi: 10.1063/5.0153825.

[134] T. Petersson and B. Hellsing, "A detailed derivation of Gaussian orbital-based matrix elements in electron structure calculations", Eur. J. Phys., volume 31 (2010) 37, https://doi.org/10.1088/0143-0807/31/1/004

[135] T. Stein, H. Eisenberg, L. Kronik, and R. Baer, "Fundamental gaps in finite systems from eigenvalues of a generalized Kohn-Sham method," *Phys. Rev. Lett.*, vol. 105, no. 26, Dec. 2010, doi: 10.1103/PhysRevLett.105.266802.

[136] A. Harindranath, R. Kundu, A. Mukherjee, and R. Ratabole, "Comment on Phys. Rev. Lett. 109, 152005 (2012)," *arXiv: High Energy Physics - Phenomenology*, p., 2012, [Online]. Available: https://consensus.app/papers/comment-on-phys-rev-lett-109-152005-2012-kundu-ratabole/490297993831557fb9aaffad1f73e343"chm5586_excited".

[137] Shinde, R. (2014). Ab initio Calculations of Optical Properties of Clusters. arXiv: Atomic and Molecular Clusters. https://doi.org/10.48550/arXiv.1607.06928

[138] V. Mahamiya, P. Bhattacharyya, and A. Shukla, "Benchmarking Gaussian Basis Sets in Quantum-Chemical Calculations of Photoabsorption Spectra of Light Atomic Clusters," *ACS Omega*, vol. 7, no. 51, pp. 48261–48271, Dec. 2022, doi: 10.1021/acsomega.2c06373.

[139] R. T. Ireland and L. K. McKemmish, "On the Specialisation of Gaussian Basis Sets for Core-Dependent Properties," Sep. 2024, doi: 10.1063/5.0159119.

[140] P. Ferrari and K. Hansen, "Computing gold cluster energies with density functional theory: the importance of correlation," *Physical Chemistry Chemical Physics*, vol. 23, no. 27, pp. 14830–14835, 2021, doi: 10.1039/d1cp02084f.

[141] J. Sui, X. Wang, and P. An, "Geometric evolution, stability trend and electronic properties of rhenium-doped gold clusters," *Comput. Theor. Chem.*, vol. 1028, pp. 98–105, 2014, doi: 10.1016/j.comptc.2013.10.028.

[142] B. R. Goldsmith *et al.*, "Two-to-three dimensional transition in neutral gold clusters: The crucial role of van der Waals interactions and temperature," *Phys. Rev. Mater.*, vol. 3, no. 1, 2019, doi:

10.1103/physrevmaterials.3.016002.

[143] P. Shao, X.-Y. Kuang, Y.-R. Zhao, Y.-F. Li, and S.-J. Wang, “Equilibrium geometries, stabilities, and electronic properties of the cationic Au n Be+ (n = 1-8) clusters: comparison with pure gold clusters,” *J. Mol. Model.*, vol. 18, no. 8, pp. 3553–3562, 2012, doi: 10.1007/s00894-012-1365-8.

[144] B.-C. Zhu, P.-J. Deng, J. Guo, W.-B. Kang, and L. Bao, “Rapid 3D roll-up of gas-phase planar gold clusters and affinity and alienation for Mg and Ge: A theoretical study of MgGeAun (n=1–12) clusters,” *iScience*, vol. 25, no. 10, p. 105215, 2022, doi: 10.1016/j.isci.2022.105215.

[145] S. Mahtout, C. Siouani, and F. Rabilloud, “Growth Behavior and Electronic Structure of Noble Metal-Doped Germanium Clusters,” *J. Phys. Chem. A*, vol. 122, no. 2, pp. 662–677, 2018, doi: 10.1021/acs.jpca.7b09887.

[146] J. Cuny, N. Tarrat, F. Spiegelman, A. Huguenot, and M. Rapacioli, “Density-functional tight-binding approach for metal clusters, nanoparticles, surfaces and bulk: application to silver and gold,” *Journal of Physics: Condensed Matter*, vol. 30, no. 30, p. 303001, 2018, doi: 10.1088/1361-648x/aacd6c.

[147] J. M. Soler *et al.*, “The SIESTA method for*ab initio*order-*N*materials simulation,” *Journal of Physics: Condensed Matter*, vol. 14, no. 11, pp. 2745–2779, 2002, doi: 10.1088/0953-8984/14/11/302.

[148] F. Baletto, “Structural properties of sub-nanometer metallic clusters,” *Journal of Physics: Condensed Matter*, vol. 31, no. 11, p. 113001, 2019, doi: 10.1088/1361-648x/aaf989.

[149] A. H. Hakimioun, B. D. Vandegehuchte, D. Curulla-Ferre, K. Kaźmierczak, P. N. Plessow, and F. Studt, “Metal–Support Interactions in Heterogeneous Catalysis: DFT Calculations on the Interaction of Copper Nanoparticles with Magnesium Oxide,” *ACS Omega*, vol. 8, no. 11, pp. 10591–10599, 2023, doi: 10.1021/acsomega.3c00502.

[150] D. Sibanda, S. T. Oyinbo, and T.-C. Jen, “A review of atomic layer deposition modelling and simulation methodologies: Density functional theory and molecular dynamics,” *Nanotechnol. Rev.*, vol. 11, no. 1, pp. 1332–1363, 2022, doi: 10.1515/ntrev-2022-0084.

[151] Y. Huang, C. Rong, R. Zhang, and S. Liu, “Evaluating frontier orbital energy and HOMO/LUMO gap with descriptors from density functional reactivity theory,” *J. Mol. Model.*, vol. 23, no. 1, p. 3, 2017.

[152] I. Khan, K. Saeed, and I. Khan, “Nanoparticles: Properties, applications and toxicities,” *Arabian Journal of Chemistry*, vol. 12, no. 7, pp. 908–931, 2019, doi: 10.1016/j.arabjc.2017.05.011.

[153] M. Aleixandre and M. C. Horrillo, “Recent Advances in SAW Sensors for Detection of Cancer Biomarkers,” *Biosensors (Basel).*, vol. 15, no. 2, p. 88, 2025, doi: 10.3390/bios15020088.

[154] M. Pourmadadi *et al.*, “Review—Cancer Biosensing Using Plasmonic Metal Doped Graphene-Based Materials,” *ECS Sensors Plus*, vol. 4, no. 1, p. 011602, 2025, doi: 10.1149/2754-2726/ada4bb.

[155] M. A. Tafoughalt and M. Samah, “Structural properties and relative stability of silver-doped gold clusters AgAun−1 (n=3–13): Density functional calculations,” *Comput. Theor. Chem.*, vol. 1033, pp. 23–30, 2014, doi: 10.1016/j.comptc.2014.01.023.

[156] Y. Chen *et al.*, “Two-Dimensional Metal Nanomaterials: Synthesis, Properties, and Applications,” *Chem. Rev.*, vol. 118, no. 13, pp. 6409–6455, 2018, doi: 10.1021/acs.chemrev.7b00727.

References

[157] F. Achi, A. M. Attar, and A. Ait Lahcen, “Electrochemical nanobiosensors for the detection of cancer biomarkers in real samples: Trends and challenges,” *TrAC Trends in Analytical Chemistry*, vol. 170, p. 117423, 2024, doi: 10.1016/j.trac.2023.117423.

[158] G. Carchini *et al.*, “How Theoretical Simulations Can Address the Structure and Activity of Nanoparticles,” *Top. Catal.*, vol. 56, no. 13–14, pp. 1262–1272, 2013, doi: 10.1007/s11244-013-0093-3.

[159] J. P. Perdew, K. Burke, and M. Ernzerhof, “Generalized gradient approximation made simple,” *Phys. Rev. Lett.*, vol. 77, no. 18, p. 3865, 1996.

[160] K. A. Peterson, D. Figgen, M. Dolg, and H. Stoll, “Energy-consistent relativistic pseudopotentials and correlation consistent basis sets for the 4d elements Y–Pd,” *J. Chem. Phys.*, vol. 126, no. 12, 2007, doi: 10.1063/1.2647019.

[161] E. Artacho et al., “SIESTA 4.1-b4 User's Guide” (2018), http://www.uam.es/siesta

[162] A. García *et al.*, “S<scp>iesta</scp>: Recent developments and applications,” *J. Chem. Phys.*, vol. 152, no. 20, 2020, doi: 10.1063/5.0005077.

[163] C. Siouani, S. Mahtout, S. Safer, and F. Rabilloud, “Structure, stability, and electronic and magnetic properties of VGe n (n= 1–19) clusters,” *J. Phys. Chem. A*, vol. 121, no. 18, pp. 3540–3554, 2017.

[164] M. A. Roumili, S. Mahtout, K. Baddari, M. Lasmi, and F. Rabilloud, “Phosphorus, cobalt-phosphorus, and nickel-phosphorus clusters: Growth behavior, electronic, and magnetic properties,” *Int. J. Quantum Chem.*, vol. 123, no. 19, 2023, doi: 10.1002/qua.27189.

[165] N. Troullier and J. L. Martins, “Efficient pseudopotentials for plane-wave calculations,” *Phys. Rev. B*, vol. 43, no. 3, p. 1993, 1991.

[166] J. Grotendorst, *Modern methods and algorithms of quantum chemistry*, vol. 1. NIC, 2000.

[167] D. D. Johnson, “Modified Broyden’s method for accelerating convergence in self-consistent calculations,” *Phys. Rev. B*, vol. 38, no. 18, pp. 12807–12813, 1988, doi: 10.1103/physrevb.38.12807.

[168] D. Toprek and V. Koteski, “Ab initio calculations of the structure, energetics and stability of AunTi (n = 1-32) clusters,” *Comput. Theor. Chem.*, vol. 1081, pp. 9–17, 2016, doi: 10.1016/j.comptc.2016.02.005.

[169] R. L. Camacho-Mendoza, L. A. Zarate-Hernandez, J. M. Vásquez-Pérez, J. Cruz-Borbolla, J. G. Alvarado-Rodriguez, and P. Thangarasu, “On the interaction of anisole and thioanisole derivatives with gold clusters studied by DFT,” *Comput. Theor. Chem.*, vol. 1126, pp. 54–64, 2018.

[170] D. Bhattacharjee, B. K. Mishra, A. K. Chakrabartty, and R. C. Deka, “DFT and QTAIM studies on structure and stability of beryllium doped gold clusters,” *Comput. Theor. Chem.*, vol. 1034, pp. 61–72, 2014, doi: 10.1016/j.comptc.2014.02.007.

[171] M. A. Mohammed, H. A. Abdulhussein, M. A. M. Al-ibadi, R. K. Raju, and R. L. Johnston, “Global minima and structural properties of Au Fe nanoalloys from a Mexican Enhanced Genetic Algorithm-based Density Functional Theory,” *Chem. Phys. Lett.*, vol. 776, no. September 2020, p. 138675, 2021, doi: 10.1016/j.cplett.2021.138675.

[172] P. V. Nhat, N. T. Si, J. Leszczynski, and M. T. Nguyen, “Another look at structure of gold clusters Aun from perspective of phenomenological shell model,” *Chem. Phys.*, vol. 493, pp. 140–148, 2017, doi: 10.1016/j.chemphys.2017.06.009.

[173] M. A. Tafoughalt and M. Samah, "Structural properties and relative stability of silver-doped gold clusters AgAun-1 (n=3-13): Density functional calculations," *Comput. Theor. Chem.*, vol. 1033, pp. 23–30, 2014, doi: 10.1016/j.comptc.2014.01.023.

[174] O. Article, "Investigation of structural and electronic properties of small AunCum (n + m ≤ 5) nano-clusters for oxygen adsorption," vol. 7, no. 3, pp. 208–224, 2016, doi: 10.7508/ijnd.2016.03.004.

[175] M. Doverstål, L. Karlsson, B. Lindgren, and U. Sassenberg, "The 3Δu−X3Δg band system of jet-cooled Ti2," *Chem. Phys. Lett.*, vol. 270, no. 3–4, pp. 273–277, 1997, doi: 10.1016/s0009-2614(97)00364-3.

[176] L. M. Russon, S. A. Heidecke, M. K. Birke, J. Conceicao, M. D. Morse, and P. B. Armentrout, "Photodissociation measurements of bond dissociation energies: Ti+2, V+2, Co+2, and Co+3," *J. Chem. Phys.*, vol. 100, no. 7, pp. 4747–4755, 1994, doi: 10.1063/1.466265.

[177] M. Salazar-Villanueva, P. H. Hernández Tejeda, U. Pal, J. F. Rivas-Silva, J. I. Rodríguez Mora, and J. A. Ascencio, "Stable Ti_n (n = 2−15) Clusters and Their Geometries: DFT Calculations," *J. Phys. Chem. A*, vol. 110, no. 34, pp. 10274–10278, 2006, doi: 10.1021/jp061332e.

[178] H. Sun, W. Zhang, and N. Xu, "Density functional calculation of structural and electronic properties of Tin-xAlx (n =2–8, 13, x=0–n) clusters," *Journal of Physics and Chemistry of Solids*, vol. 118, pp. 126–136, 2018, doi: 10.1016/j.jpcs.2018.01.029.

[179] M. D. Morse, "Clusters of transition-metal atoms," *Chem. Rev.*, vol. 86, no. 6, pp. 1049–1109, 1986, doi: 10.1021/cr00076a005.

[180] H. Sun, Y. Ren, Z. Wu, and N. Xu, "Density functional calculation of the growth, electronic and bonding properties of titanium clusters Tin (n=2-20)," *Comput. Theor. Chem.*, vol. 1062, pp. 74–83, 2015, doi: 10.1016/j.comptc.2015.03.021.

[181] C. W. Bauschlicher, H. Partridge, S. R. Langhoff, and M. Rosi, "A theoretical study of the low-lying states of Ti2 and Zr2," *J. Chem. Phys.*, vol. 95, no. 2, pp. 1057–1063, 1991, doi: 10.1063/1.461133.

[182] R. Haichour and S. Mahtout, "Ab initio DFT simulation of electronic and magnetic properties of Tin+1 and FeTin clusters," *J. Mol. Model.*, vol. 28, no. 3, 2022, doi: 10.1007/s00894-022-05041-x.

[183] G. V Gadiyak, Yu. N. Morokov, A. G. Mukhachev, and S. V Chernov, "Electron density functional method for molecular system calculations," *Journal of Structural Chemistry*, vol. 22, no. 5, pp. 670–674, 1982, doi: 10.1007/bf00746425.

[184] S. Furukawa and Y. Nakaya, "Subnanometric Platinum–Germanium Clusters Break the Activity–Stability Tradeoff in Propane Dehydrogenation," 2023, *Springer Science and Business Media LLC*. doi: 10.21203/rs.3.rs-3395297/v1.

[185] Y. Xu, W. A. Shelton, and W. F. Schneider, "Effect of Particle Size on the Oxidizability of Platinum Clusters," *J. Phys. Chem. A*, vol. 110, no. 17, pp. 5839–5846, 2006, doi: 10.1021/jp0547111.

[186] L. Xiao and L. Wang, "Structures of Platinum Clusters: Planar or Spherical?," *J. Phys. Chem. A*, vol. 108, no. 41, pp. 8605–8614, 2004, doi: 10.1021/jp0485035.

[187] N.B. Singh, and U. Sarkar, "Structure, Vibrational and Optical Properties of Platinum Cluster: A Density Functional Theory Approach", J. Mol. Model., 20 (2014) 2537,https://doi.org/10.1007/s00894-014-2537-5

[188] P. Ferrari and K. Hansen, “Computing gold cluster energies with density functional theory: the importance of correlation,” *Physical Chemistry Chemical Physics*, vol. 23, no. 27, pp. 14830–14835, 2021, doi: 10.1039/d1cp02084f.

[189] J. Yadav and S. Saini, “Atop adsorption of oxygen on small sized gold clusters: Analysis of size and site reactivity from restructuring perspective,” *Comput. Theor. Chem.*, vol. 1191, no. August, p. 113014, 2020, doi: 10.1016/j.comptc.2020.113014.

[190] M.-X. Chen and X.-H. Yan, “Density functional calculations for stability of Titanium-doped Gold clusters AunTi (n=2-16)”, arXiv preprint (2007), https://arxiv.org/abs/physics/0702026

[191] P. Wang, X. Wang, L. Wang, X. Hou, W. Liu, and C. Chen, “Interaction of gold nanoparticles with proteins and cells,” *Sci. Technol. Adv. Mater.*, vol. 16, no. 3, p. 34610, 2015, doi: 10.1088/1468-6996/16/3/034610.

[192] N. T. Si, P. V. Nhat, and M. T. Nguyen, “Binding mechanism and SERS spectra of 5-fluorouracil on gold clusters,” *Front. Chem.*, vol. 10, no. December, pp. 1–13, 2022, doi: 10.3389/fchem.2022.1050423.

[193] C. Lu *et al.*, “Design of a gold clustering site in an engineered apo-ferritin cage,” *Commun. Chem.*, vol. 5, no. 1, pp. 1–11, 2022, doi: 10.1038/s42004-022-00651-1.

[194] X. Huang and M. A. El-Sayed, “Gold nanoparticles: Optical properties and implementations in cancer diagnosis and photothermal therapy,” *J. Adv. Res.*, vol. 1, no. 1, pp. 13–28, 2010, doi: 10.1016/j.jare.2010.02.002.

[195] X. Yuan, X. Dou, K. Zheng, and J. Xie, “Recent Advances in the Synthesis and Applications of Ultrasmall Bimetallic Nanoclusters,” *Particle & Particle Systems Characterization*, vol. 32, no. 6, pp. 613–629, 2015, doi: 10.1002/ppsc.201400212.

[196] D. W. Yuan, Y. Wang, and Z. Zeng, “Geometric, electronic, and bonding properties of AuNM (N=1–7, M=Ni, Pd, Pt) clusters,” *J. Chem. Phys.*, vol. 122, no. 11, 2005, doi: 10.1063/1.1862239.

[197] Y.-R. Zhao, “Structures, Stabilities, and Electronic Properties for Rare-Earth Lanthanum Doped Gold Clusters,” *Zeitschrift für Naturforschung A*, vol. 70, no. 2, pp. 91–99, 2015, doi: 10.1515/zna-2014-0160.

[198] M. Brack, “The physics of simple metal clusters: self-consistent jellium model and semiclassical approaches,” *Rev. Mod. Phys.*, vol. 65, no. 3, pp. 677–732, 1993, doi: 10.1103/revmodphys.65.677.

[199] A. Mahalanabish, S. H. Huang, D. Tulegenov, and G. Shvets, “Infrared Spectroscopy of Live Cells Using High-Aspect-Ratio Metal-on-Dielectric Metasurfaces,” *Nano Lett.*, vol. 24, no. 37, pp. 11607–11614, 2024, doi: 10.1021/acs.nanolett.4c03155.

[200] Rekha, S. P., & Gunasekaran, S. (2018). A novel spectroscopic analysis to detect photochemical reaction of the bronchodilator - Doxofylline and its estimation in pharmaceutical formulation.. Spectrochimica acta. Part A, Molecular and biomolecular spectroscopy, 190, 140-149 . https://doi.org/10.1016/j.saa.2017.09.006

[201] P. Ferrari and E. Janssens, “Relative stability of small silver, platinum, and palladium doped gold cluster cations,” *Applied Sciences (Switzerland)*, vol. 9, no. 8, 2019, doi: 10.3390/app9081666.

[202] E. Janssens, S. Neukermans, H. M. T. Nguyen, M. T. Nguyen, and P. Lievens, “Quenching of the Magnetic Moment of a Transition Metal Dopant in Silver

Clusters," *Phys. Rev. Lett.*, vol. 94, no. 11, 2005, doi: 10.1103/physrevlett.94.113401.

[203] R. G. Parr and R. G. Pearson, "Absolute hardness: companion parameter to absolute electronegativity," *J. Am. Chem. Soc.*, vol. 105, no. 26, pp. 7512–7516, 1983, doi: 10.1021/ja00364a005.

[204] J.-K. Zhao, J. Liu, J. Yang, P.-F. Liu, and F. Qiao, "Study on the structure, electronics, and optics of gold cluster functionalized Mo2C based on strong metal support interaction: A comprehensive DFT study," *Colloids Surf. A Physicochem. Eng. Asp.*, vol. 679, p. 132552, 2023.

[205] P. V. Nhat *et al.*, "Tube-like Gold Clusters $M_2@Au_{17}^q$ (M = W, Mo; q = 0, ±1): Structure, Electronic Property, and Optical Nonlinearity," *ACS Omega*, vol. 9, no. 37, pp. 38467–38476, 2024, doi: 10.1021/acsomega.4c02724.

[206] M. Lasmi, S. Mahtout, and F. Rabilloud, "The effect of palladium and platinum doping on the structure, stability and optical properties of germanium clusters: DFT study of PdGen and PtGen (n = 1–20) clusters," *Comput. Theor. Chem.*, vol. 1181, no. January, pp. 1–7, 2020, doi: 10.1016/j.comptc.2020.112830.

[207] Z. Li, B. Li, and C. Yu, "Dynamic Catalytic Structures of Single-Atom (or Cluster) Catalysts: A Perspective Review," *Small Struct.*, vol. 6, no. 5, p. 2400479, 2025.

[208] B. Omran, "Nanotechnology in the Life Sciences Nanobiotechnology: AAMultidisciplinary Field offScience." [Online]. Available: http://www.springer.com/series/15921

[209] J. Cuny, N. Tarrat, F. Spiegelman, A. Huguenot, and M. Rapacioli, "Density-functional tight-binding approach for metal clusters, nanoparticles, surfaces and bulk: application to silver and gold," *Journal of Physics: Condensed Matter*, vol. 30, no. 30, p. 303001, 2018, doi: 10.1088/1361-648x/aacd6c.

[210] D. Traore, E. Giner, and J. Toulouse, "Basis-set correction based on density-functional theory: Linear-response formalism for excited-state energies.," *J. Chem. Phys.*, vol. 158 23, p., 2023, doi: 10.1063/5.0156317.

[211] J. Kottmann, S. Höfener, and F. Bischoff, "Numerically accurate linear response-properties in the configuration-interaction singles (CIS) approximation.," *Phys. Chem. Chem. Phys.*, vol. 17 47, pp. 31453–31462, 2015, doi: 10.1039/c5cp00345h.

[212] D. Traore, E. Giner, and J. Toulouse, "Basis-set correction based on density-functional theory: Linear-response formalism for excited-state energies," May 2023, doi: 10.1063/5.0156317.

[213] D. Rappoport, "Property-Optimized Gaussian Basis Sets for Lanthanides", J. Chem. Phys. 155 (2021) 124102, https://doi.org/10.1063/5.0065611

[214] V. M. Ramos, B. C. Severino, F. M. Brugnari, L. De Lima Conceição, A. S. Rocha, and A. De Lima Batista, "Assessing and applying DFT approaches for geometries and UV–Vis absorption spectra of tetragonal iron(II) complexes," *Theor. Chem. Acc.*, p., 2024, doi: 10.1007/s00214-024-03150-9.

[215] B.-C. Zhu, P.-J. Deng, J. Guo, W.-B. Kang, and L. Bao, "Rapid 3D roll-up of gas-phase planar gold clusters and affinity and alienation for Mg and Ge: A theoretical study of MgGeAun (n=1–12) clusters," *iScience*, vol. 25, no. 10, p. 105215, 2022, doi: 10.1016/j.isci.2022.105215.